A Numerical Study of the Complex Lorenz System as a Dynamical Model

Mabruka Ali Salem Mohamed

Submitted in Fulfilment of the Requirements for
the Degree of Doctor of Philosophy

Department of Applied Mathematics

June 2015

Supervisor: Dr. Eun-jin Kim

University of Sheffield

To my country (Libya)
Thank you for everything.

"Many of life's failures are people who did not realize how close they were to success when they gave up."

Thomas A. Edison

Acknowledgements

First, my gratitude goes to the Almighty Allah for his inspiration, who enabled me to perform this thesis. I would also like to express my thank to my supervisor Dr. Eun-jin Kim for accepting me to do a PhD in applied Mathematics despite my background being in pure Mathematics. I am thankful to my colleagues in the School of Mathematics and Statistics, there are too many people to name you all personally. I am particularly thankful to Prof. Elizabeth Winstanley and Prof. Caitlin Buck for their sincere advice through the period of my study. I would like to thank my examiners (Prof. Michael Ruderman and Dr. Bogdan Hnat), whose insightful comments improved the work contained within this thesis.

I would like to thank the Ministry of Higher Education in Libya for the financial support.

Finally, my huge thanks to my grandfather and family for their constant encouragement in spite of being far away from me, and also my sons (Omar and Mouath).

Abstract

A nonlinear dynamical system is a mathematical model for a portion of the physical world where continuous components are interacting with each other. Such systems are complex, and it is difficult to predict how they will react towards changing the driving parameters and initial conditions.

This dissertation is concerned with the numerical aspect of controlling the Lorenz system that studies the production of the magnetic field in sunspots. The study aims to do this by applying different approaches to the system. A study on the impact of the oscillatory control parameter $D = C_0 \cos(\omega_1 t)$ was carried out, where C_0 and ω_1 are the driving amplitude and frequency, respectively. Overall, finite-amplitude solutions were obtained for sufficiently small ω_1 and large C_0, even though the mean value of D was zero. In addition to this, a linear relationship between C_0 and ω_1 for the transition between finite-amplitude and damping solutions was found.

The combined effect of constant and oscillatory control parameters on the complex Lorenz system was also investigated. This was done by presuming that the control parameter D consists of a constant D_0 and an oscillatory part $C_0 \cos(\omega_1 t)$. The effect of C_0 and ω_1 on the linear and nonlinear response of the Lorenz system for different values of D_0 was numerically observed. In sharp contrast to this linear response, a non-monotonic behaviour is manifested in the nonlinear case where the amplitude and frequency of dynamical variables become minimum. An interesting relation $C_0 \approx D_0 + 1$ is found for the minimum response in this nonlinear case as the system stays in

a Dead-Zone for the longest time. The effect of the oscillatory control parameter disappears both linearly and nonlinearly for sufficiently large ω_1.

Furthermore, this thesis explores the phenomenon of Stochastic Resonance (SR) as a result of using internal and external parameters simultaneously.

Achievements and Copyright Notice

- The work included in Chapter 2 has been previously published in Physica Scripta and is consequently subject to copyright: Oscillatory control parameters in nonlinear chaotic systems, Mabruka Mohamed and Eun-jin Kim, Phys. Scr. 89 (2014) 015202 (8pp) doi:10.1088/0031-8949/89/01/015202.

- A paper was published in Physics of Plasmas under the title (Confinement improvement by fluctuating input power), 20 2013, 114504–4p, Sarah Douglas, Mabruka Mohamed and Eun-jin Kim.

- The work included in Chapter 3 has been previously submitted and is consequently subject to copyright: (Computational study of a complex Lorenz system), Mabruka Mohamed and Eun-Jin Kim, 2015.

- A paper submitted under the title (Improved confinement by transition of input heating power for tokamak plasmas); Muhammad Asif, Mabruka Mohamed and Eun-jin Kim, 2015.

- **I reviewed two papers** were submitted for consideration to publish in (Physics Letters A) and the International Journal of Biomathematics (IJB).

Contents

Acknowledgements **iv**

Achievements and Copyright Notice **vii**

Preface **xvi**

1 Introduction **1**

1.1 The Sun 1

1.1.1 Rotation of the Sun 3

1.1.2 Sunspots 4

1.1.3 Magnetic Field in Sunspots 5

1.2 Dynamical Systems 7

1.2.1 Stability of Dynamical Systems 10

1.2.2 Linearised Differential Equations 11

1.2.3 Dissipative Systems 12

1.2.4 Fourier Transform 12

1.2.5 Frequency Spectrum 13

1.2.6 Bifurcations 13
1.2.7 Resonance 14
1.3 The Lorenz System 16
1.3.1 Magnetohydrodynamics 17
1.3.2 The Magnetic Reynolds Number 18
1.3.3 Bifurcation Diagram of the Lorenz System 25
1.3.4 Stability 26
1.3.5 The system's features 27

2 Oscillatory Control Parameters 30

2.1 Introduction 31
2.2 Results for Fixed ω_1 34
2.2.1 $\omega_1 = 0.5$ with varying C_0 34
2.2.2 $\omega_1 = 10$ with varying C_0 40
2.3 Results for Fixed C_0 44
2.3.1 $C_0 = 2$ with varying ω_1 45
2.3.2 $C_0 = 20$ with varying ω_1 47
2.4 Discussion and Conclusion 50
2.4.1 The Damping in the Linearise Lorenz system 52

3 Parametric Instability and Nonlinear Feedback 53

3.1 Introduction 54

3.1.1 Model and Motivation 55

3.1.2 Aims and Outline 57

3.2 Linear Results 59

3.3 Non-linear Results for $D_0 = 2$ 61

3.3.1 Results for fixed C_0 62

3.3.2 Results for fixed ω_1 70

3.3.3 Summary of results for $D_0 = 2$ 72

3.4 Nonlinear Results for $D_0 = 4$ 76

3.4.1 Results for fixed $C_0 = 2$ and $C_0 = 20$ 76

3.4.2 Summary of results for $D_0 = 4$ 79

3.5 Discussion and Conclusions 82

4 Internal and External Forcing Effects 86

4.1 Introduction 87

4.2 Numerical Results 88

4.3 Results for Varying C_0 and F_0 for $\omega_1 = \omega = 0$ 88

4.3.1 Case I: (Amplitude of B) 90

4.3.2 Case II: (Amplitude of A) 93

4.4 The Linear Growth Rate for Varying C_0 and $\omega = \omega_1$ for $F_0 = 1$ . . 101

4.5 Nonlinear Results for Varying C_0 and $\omega_1 = \omega$ for $F_0 = 1$ 102

4.6 Results for varying ω_1 and ω, and fixed value of $C_0 = 1$ 104

4.7 Discussion and Conclusion 108

5 Concluding Remarks **110**

6 Future Work **113**

Bibliography **116**

Appendix A: **126**

List of Figures

1.1 The Sun's layers. 2

1.2 Picture illustrating the rotation of the Sun, it was taken from Astronomy TodayChaisson and McMillan (2011). 3

1.3 Sunspots recently from 2012 and from 68 years ago, with the Earth and Jupiter for size comparison Major (2012). 5

1.4 Sunspots historical record Hoyt and Schatten (1998) 7

1.5 A graph illustrating the poloidal (θ) direction, represented by the vertical circle, and the toroidal $(\ \Phi)$ direction, represented by the horizontal circle. 20

1.6 Bifurcation diagram for $0 < D < 4$. 25

2.1 (a) Phase-space of $\mathrm{Re}(A)$, $\mathrm{Re}(B)$ and $\mathrm{Re}(\Psi)$ for $C_0 = 5.11$. (b) Time series of $\mathrm{Re}(A)$ for $C_0 = 5.11$. 35

2.2 (a) Quasi-periodic solution of (2.1) for $C_0 = 5.12$. (b) Time series of $\mathrm{Re}(A)$ for $C_0 = 5.12$. The Poincaré sections for $\omega_1 = 0.5$ are denoted by red circles. 35

2.3 The dominant frequencies of B for $\omega_1 = 0.5$. 37

2.4 The frequency spectrum of the magnetic field against C_0 for $\omega_1 = 0.5$. 38

2.5 The frequency spectrum of the magnetic field for $C_0 = 2, \ 5$ and 10 at $\omega_1 = 0.5$. 39

2.6 The amplitude of $Log(|B|^2)$ against C_0 for $\omega_1 = 0.5$. 40

2.7 Chaotic attractors for $C_0 = 45$. 41

2.8 The frequency spectrum of the magnetic field against C_0 for $\omega_1 = 10$. 42

2.9 $Log(|B|^2)$ as a function of C_0 for $\omega_1 = 10$. 43

2.10 Frequency spectrum of the magnetic field as a function of ω_1 for $C_0 = 2.2$. 46

2.11 $|B|^2$ as a function of ω_1. 46

2.12 (a) 2D trajectory plot of Re(A) against Re(B) for a chaotic solution at $\omega_1 = 1$. (b) Time series of Re(A). 48

2.13 The frequency power spectrum of the magnetic field for $C_0 = 20$. 49

2.14 $Log(|B|^2)$ as a function of ω_1 for $C_0 = 20$. 49

2.15 C_0 against ω_1 for the onset of a finite-amplitude solution. 51

2.16 C_0 against ω_1 for the onset appear in the linearised system. . . . 52

3.1 Linear growth rates for (a) $D_0 = C_0 = 2$; (b) $D_0 = 2$ and $C_0 = 20$; (c) $D_0 = 4$ and $C_0 = 2$; (d) $D_0 = 4$ and $C_0 = 20$. 60

3.2 (a) Quasi-periodic solution of Eq. (3.1) where the Poincaré-sections are shown in red circles; (b) The time history of Re(A) for $\omega_1 = 4$. 63

3.3 $|B|^2$ as a function of ω_1 64

3.4 The dominant output frequencies of B for $D_0 = C_0 = 2$. 64

3.5 The frequency spectrum of B against ω_1 for $D_0 = C_0 = 2$. 66

3.6 $|B|^2$ against ω_1 for $D_0 = 2$ and $C_0 = 20$. 68

3.7 The dominant frequencies of B against ω_1 for $D_0 = 2$ and $C_0 = 20$. 69

3.8 The frequency spectrum of B against ω_1 for $D_0 = 2$ and $C_0 = 20$. 69

3.9 Quasi-periodic solution of the system with the Poincaré sections shown in red circles for $C_0 = 2$. 71

3.10 $|B|^2$ as a function of C_0 for $\omega_1 = 3$ 71

3.11 The frequency power spectrum of B against C_0 for $\omega_1 = 3$ 72

3.12 3D plot of B amplitude 73

3.13 3D plot of the dominant output frequency of B for fixed $D_0 = 2$ against C_0 and ω_1 73

3.14 (a) Coordinates of the valley in Fig. 3.12; (b) The value of $|B|^2$ against C_0 at the valley in Fig. 3.13 (c) Coordinates of the valley in Fig. 3.13; (d) The value of the output frequency against C_0 at the valley in Fig. 3.13. 75

3.15 The amplitude of B as a function of ω_1 for $C_0 = 2$ 77

3.16 The amplitude of B as a function of ω_1 for $C_0 = 20$. 77

3.17 Frequency spectrum of B against ω_1 for $C_0 = 2$ 78

3.18 Frequency spectrum of B against ω_1 for $C_0 = 20$. 79

3.19 $|B|^2$; the colour is assigned to the intensity according to the scale shown in the colour bar on the right. 80

3.20 Dominant output frequency of B against ω_1 and C_0. 80

3.21 (a) Coordinates of the valley in Fig. 3.19; (b) The value of $|B|^2$ against C_0 at the valley in Fig. 3.19); (c) Coordinates of the valley in Fig. 3.20; (d) The value of the output frequency against C_0 at the valley in Fig. 3.20. 82

3.22 $\omega_1/15$ against C_0 where the effect of the oscillatory C_0 disappears for different values of D_0. 84

3.23 The values of C_0 (in red circles) and ω_1 (in blue stars) against D_0 where $|B|^2$ becomes minimum. 84

4.1 3D plot of the amplitude B as a function of C_0 and F_0 90

4.2 3D plot of the dominant angular frequency of B as a function of C_0 and F_0. 90

4.3 The coordinate of F_0 and C_0 when the maximum amplitudes occur is shown in red stars. The damping region is shown in blue. . . . 92

4.4 (a) 3D plot of A amplitude for fixed $D_0 = 2$. 94

4.5 $Log|B|^2$ in blue and $Log|A|^2$ in red as function of F_0 for fixed $C_0 = 3$. 96

4.6 Phase space portrait of the system's components $Re(A)$, $Re(B)$ and $Re(\Psi)$ in X, Y and Z axises, respectively, for $C_0 = 3$ and $F_0 = 1$ 97

4.7 Time-domain of $Re(A)$ in red dashed line and $Re(B)$ in blue continuous line, for $C_0 = 3$ and $F_0 = 1$, when the system is exhibiting finite-amplitude solutions, for $C_0 = 3$ and $F_0 = 1$. 97

4.8 Time-domain of $Re(A)$ in red dashed line and $Re(B)$ for $C_0 = 3$ and $F_0 = 7$, when the system exhibiting finite amplitude solution. 98

4.9 $Log|A|^2$ and $Log|B|^2$ against C_0 for fixed $F_0 = 1$. 99

4.10 Phase trajectories for four different values of C_0 at $F_0 = 1$. (a) $C_0 = 1.5$, the case of limited oscillating solution; (b) and (c) the system's orbits when periodic oscillation solutions observed, for $C_0 = 2.3$ and $C_0 = 3.3$, respectively; and (d) an example of chaotic oscillating. 100

4.11 The linear system's growth rate for varying C_0 and fix $F_0 = 1$ and $\omega = \omega_1 = 0, 1, 2$ and 5 102

4.12 (a) $|B|^2$ as a function of C_0 and ω_1 for $F_0 = 1$;(b) $|B|^2$ as a function of C_0 and ω_1 for $F_0 = 0$. 103

4.13 For $C_0 = 1$, 3D for $|B|^2$ as a function of ω and ω_1 for $F_0 = 2,\ 30$ and 100 in (a), (b) and (c) respectively. 105

4.14 Results of the numerical solution for the system (4.1) when (C_0, F_0, ω_1, ω)=(1, 30, 6, 6). The red circles represent the Poincaré section. (a) The system phase-space; (b) Angular frequency; (c) the time series. 106

4.15 The maximum peaks of $|B|^2$ as a function of F_0 107

Preface

The dynamical system is one of the oldest and most highly developed parts of physics that has been studied by many mathematicians for over a hundred years. Principally, its importance increases as the variety of its applications grow. Such systems are very common in nature. Various examples are found in every discipline of science, from a comparatively simple system involving a pendulum to a much more complex celestial system, and from artificial systems (e.g. swarm robotics) to biological systems (e.g. stem cell behaviour) (Takens and Broer, 2009, Ott, 1993, Orme and Chaplain, 1996, Anderson et al., 2000). By replacing the actual dynamical system with a mathematical model as a set of differential equations that can be analysed, one can obtain appropriate information about the problem under study. This approach becomes a good way of investigating their behaviour in order to determine useful information about the parts of the real world we are studying. The mathematical solutions have to be evaluated and interpreted technically.

Among others, the Lorenz system is a popular nonlinear dynamical model that has been widely used to understand complex nonlinear behaviour such as predicting pattern formation, weather, forest fires, population dynamics and magnetic activities in astronomical and laboratory systems (e.g. Bhattacharyaya and Bhattacharjee (2001), Proctor (2007)).

This thesis is focused on the study of the Lorenz system as a typical example of a nonlinear dynamical system. In particular, we aim to investigate numerically the mechanisms of generating the magnetic field inside sunspots. We address this process using the Lorenz system as a simulation model for different parameters; an internal time-dependent parameter, a mixture of a constant and time-dependent-parameter, and internal and external time-dependent parameters. These three schemes drive the system differently due to the types of parameters involved.

To guide the reader, we will give a brief summary of the contents of each chapter.

- **Chapter 1:** In this chapter, we give background information to support the understanding of the thesis. We also report on related studies that have been produced in the case of using a constant parameter D as the dynamo number.
- **Chapter 2:** We study the effect of the time-dependent parameter $D = C_0 \cos(\omega_1 t)$ on the Lorenz system, where C_0 is the driving amplitude and ω_1 is the driving frequency.
- **Chapter 3:** We extend the study in Chapter 2 by assuming that the control parameter D is a combination of a constant part D_0 and an oscillating part $C_0 \cos(\omega_1 t)$ for different values of D_0. Since D changes between $D_0 - C_0$ and $D_0 + C_0$ as time varies, the system effectively goes through different varieties of attractors, from damping to chaotic solutions, including multiple oscillations.
- **Chapter 4:** In this chapter we identify the Lorenz system's mechanism when an internal and external parameter are used at the same time, aiming

for an improvement to the dynamical system so that it creates the right opportunity for the appearance of some phenomena, such as resonance and undamped solutions.

- **Chapter 5:** We summarise the thesis.
- **Chapter 6:** We draw the plan for future work.

Mabruka Mohamed, June, 2015

Chapter 1

Introduction

§ 1.1 The Sun

The Sun is the nearest star to the Earth, positioned at the heart of our solar system; it is an enormous rotating ball of hot gas and plasma. The Sun's a radius $R_\odot \approx 6.955 \times 10^5 km$ and a total mass of $198.89 \times 10^{28} kg$. This mass converts into energy at the rate of 380×10^{24} watts Dam and Lin (1996). The Sun is an essential source of light and heat for the Earth; the solar energy is generated due to the nuclear reactions that turn hydrogen into helium. The interior of the Sun cannot be perceived directly due to the opaqueness of the Sun's surface.

- The **solar interior** is classified into three layers: the Core, the radiation zone and the convection zone. These regions are shown in Fig. 1.1.
- The **solar exterior** consists of three layers; the photosphere, the transition

region, and the corona.

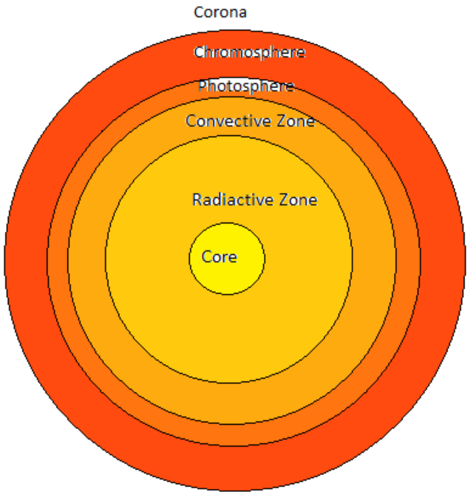

Figure 1.1: The Sun's layers.

In the **Core** region, hydrogen plasma fuses in a reaction, which generates helium nuclei, neutrons and photons. This layer represents a 20 % of the radius of the Sun. The temperature diverges over the core, from about 15 million Kelvin at the kernel to about 5 million Kelvin at the edge of the core Vernazza et al. (1976) Watson (2012). The **radiation zone** is the second layer of the solar interior, when the energy is transported as photons, instead of convection Noyes (1982). This represents the zone extends from the core outward to about $0.7R_{\odot}$ Charbonneau et al. (1999). The **convection zone** is the outermost zone of the Sun's interior. It lies between the radiation zone and the visible surface at a depth of about 200,000 km, which represents about 30% of the radius of the Sun's interior. In-depth studies of the Sun can be found in many sources for instance Watson (2012),Noyes (1982).

1.1.1 Rotation of the Sun

The Sun is not solid, and therefore it does not rotate uniformly; the poles of the Sun rotate slower than the equator. It takes up to 35 days to rotate at the poles whereas it takes just 25 days to rotate at the equator. This is known as differential rotation. Sunspots and many other solar activities are due to this phenomenon.

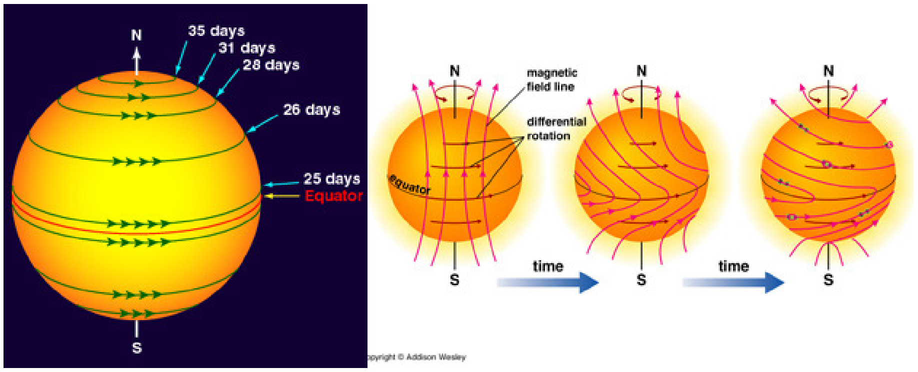

Figure 1.2: Picture illustrating the rotation of the Sun, it was taken from Astronomy TodayChaisson and McMillan (2011).

The physical process of producing the magnetic field in the Sun is known as the solar dynamo. The Sun, as does other celestial objects, generates the magnetic field; the apparent evidence for the evidence for this lies in the existence of sunspots.

1.1.2 Sunspots

Sunspots are dark regions that exist on the exterior of the Sun, generated by the high magnetic field strength. Sunspots appear to be darker because they are cooler than the areas around them Russell (2010). Temperatures in the deep cores of sunspots drop to about 3700 Kelvin (compared to 5700 Kelvin for the photosphere that surrounds it).

Three years after the first telescope was produced in Europe in 1608, Galileo performed scientific observations and concluded that indeed the Sun has spots. Also, he reported a change in the size and pattern of these spots. Sunspots appear at latitudes of approximately ±40° at the beginning of a new cycle Nicolson (1982). As the cycle progresses, spots move towards the equator, and at the end of the cycle reach about ±5° latitude. Sunspots observed for the first time with the naked eye in at least 200BC by Chinese (Eddy et al. (1989), Yau and Stephenson (1988)). Sunspots appear in a butterfly pattern. This name is inspired by the structure which show two butterfly wings that begin far apart at the beginning of the cycle and come together over time. The physical reason for this movement of the sunspot structure as a butterfly can be linked to the progress of the solar magnetic field during its cycle due to the differential rotation as illustrated in Fig.1.2.

After discovering the magnetic fields in sunspots, Hale et al., 1919 Hale et al. (1919) found that there are two large sunspot sets, which have opposite magnetic field polarities and are seen side-by-side. In other words, they spotted that sunspots normally appear as two sets of spots. One set has a north (positive) magnetic field, and the other set has a south (negative) magnetic field. The magnetic field is strongest in the darker parts of the spots which are called the umbra.

The 11-year sunspot cycle is associated with a 22-year cycle for the reversal of the solar magnetic field Hathaway (2014).

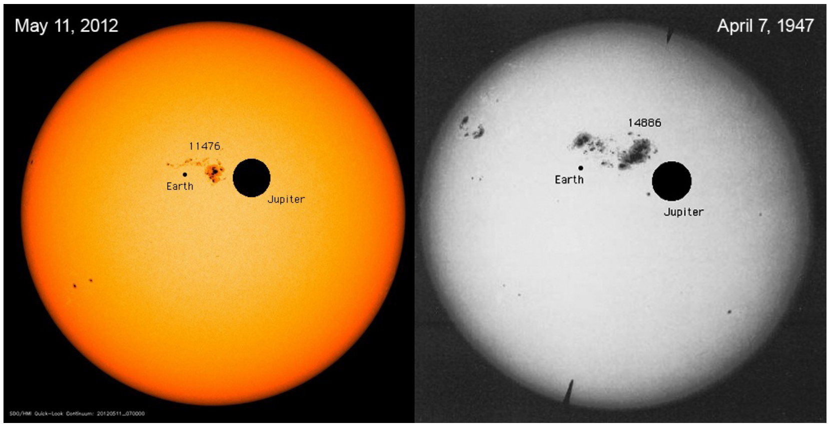

Figure 1.3: Sunspots recently from 2012 and from 68 years ago, with the Earth and Jupiter for size comparison Major (2012).

The pictures in Fig. 1.3 were taken by the NASA Solar Dynamics Observatory Major (2012). They illustrate sunspot areas in comparison with the sizes of Earth and Jupiter, which demonstrates the scale of the sunspot phenomenon.

1.1.3 Magnetic Field in Sunspots

Magnetic fields exist everywhere in the Cosmos. They seem to be found wherever large amounts of fluid with enough electrical field motion are present along with mixed with convection and rotation Gailitis et al. (2002).

The magnetic field arises from under the surface of the Sun and moves up through the atmosphere, generating multiple structures on various length scales Solanki et al. (2006) Babcock (1961) Ostlie and Carroll (1996).

Two mechanisms for producing the magnetic field in the Sun have been introduced. One States that the Sun is a magnetic oscillator with settled poloidal and toroidal fields that vibrate with a 22-year period. The other believes that there exists a dynamo; where a poloidal field is created due to the persistent helicity of convective eddies in a rotating system Weiss (1990).

The first measurement of the magnetic fields in sunspots was at the beginning of the 20*th* century. A detailed study of the existence of magnetic fields in sunspots was completed by George Hale in a paper with the title "On the Probable Existence of a Magnetic Field in Sun-Spots" (Hale, 1908) Hale (1908). The magnetic strength in the interior of the sunspot is much higher in comparison to the magnetic strength exterior. Outside the sunspots the magnetic field ranges between 10 and 50 Gauss, whereas it ranges between an astounding 1000-3000 Gauss in the interior, which is about 10^4 stronger than the magnetic field of the Earth at the surface (0.5 Gauss).

A recent paper showed that the magnetic field probably plays a significant role in the Earth's weather Haigh (2003). Consequently, studying the magnetic field in sunspots is important, as a study of this nature can help in understanding the climate patterns of Earth.

In this work, we concentrate on numerical simulations of the mechanism for generating the magnetic field in sunspots. Further detail about observational studies related to the Sun, sunspots, and the magnetic field in sunspots can be found in the thesis presented by Watson, University of Glasgow (2012) Watson (2012), Stix (2000).

Past records of sunspot observations as illustrated in Fig. 1.4 clearly show that the solar cycle is aperiodic.

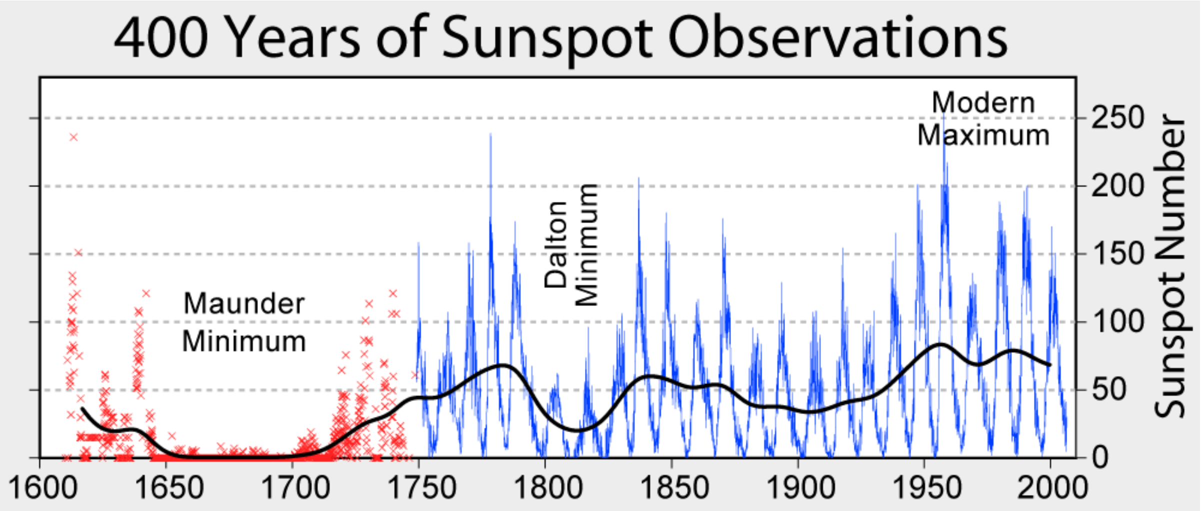

Figure 1.4: Sunspots historical record Hoyt and Schatten (1998)

It is notable that during the second half of the 17th century there was a Maunder Minimum period, where much fewer sunspots were observed Shindell et al. (2001), Wuebbles et al. (1998). In the Maunder minimum period, solar activity was lower than the early 2000s (Sokoloff (2004)). The number of sunspots suggests that the solar dynamo is oscillating nonlinearly Jones et al. (1985). The solar cycle's features are described in much more detail in Noyes (1982). Since the generation of magnetic fields in sunspots is a dynamical process, we will be exposed to the study of dynamical systems and some of their properties in the following section.

§ 1.2 Dynamical Systems

A dynamical system is a system of quantities that changes in time. It can be any mechanism that evolves deterministically Apety (2011).

A large number of situations in nature can be simulated as dynamical systems, modelling them as a set of ordinary differential equations (ODEs). It is a good approach to investigate their behaviour in order to determine useful information about the parts of the real life world we are studying. This analysis can help us to understand what happens to a system's behaviour as time changes. Among others, the Lorenz system is a popular nonlinear dynamical model that has been widely used to understand complex nonlinear behaviour, such as predicting pattern formation, weather, forest fires, population dynamics and magnetic activities in astrophysical and laboratory systems (e.g. Bhattacharyaya and Bhattacharjee (2001), Proctor (2007)).

For instance, the population sizes of different species of plants and animals in an ecological system, and the positions and speeds of celestial bodies are examples of natural phenomena that can be described by dynamical systems. In conjunction with the development of computers, applied mathematics has made a significant contribution as a tool to model and understand dynamical systems in different fields.

We aim to investigate nonlinear dynamical systems and their related bifurcations and also to perform linear stability analysis. This linearisation of systems, equilibrium points, and stability properties not only helps in understanding the system's behaviour, but also gives us an idea of the acceptable range of the numerical solutions Ott (1993).

There are two kinds of dynamical systems: continuous and discrete. To explain the concept of these types of dynamical systems in the real world we are presenting the following two simple examples:

- Consider a pendulum consisting of a solid stick with a ball bonded at its end, and that the pendulum is free to swing around the pivot point. This kind of pendulum oscillates without any friction, and so, it will remain oscillating permanently. Such a mechanism gives an example of a continuous dynamical system.

- On the other hand, assume we measure changes in a bacterial population over time. The growth of a bacterial population is an example of a discrete-time dynamical system.

In this thesis, we focus on a continuous dynamical system.

Consider f_i (i=1, 2, ...n) continuous functions in time t, the system of n ordinary differential equations with the initial conditions takes the following form:

$$\begin{aligned} \dot{x_1}(t) &= f_1(x_1, x_2, \ldots, x_n, \mu_1) \\ \dot{x_2}(t) &= f_2(x_1, x_2, \ldots, x_n, \mu_2) \\ \vdots &= \vdots \\ \dot{x_n}(t) &= f_n(x_1, x_2, \ldots, x_n, \mu_n) \end{aligned} \tag{1.1}$$

$X(0) = (x_1(0),\ x_2(0),\ \ldots,\ x_n(0)) \equiv X_0$ where $(x_1,\ x_2,\ \ldots, x_n)$ are variables, $(f_1,\ f_2,\ \ldots,\ f_n)$ are functions telling us how these variables change with time, and μ are parameters Spiegelman (1997).

For any initial state of the system $X(0)$, we can determine a solution of the equations (1.1) either analytically or numerically to obtain the system state $X(t)$ at any time $t > 0$. The set of equations (1.1) (for linear homogeneous systems) can also be written in the following format:

$$\dot{X} = AX. \tag{1.2}$$

where A is a coefficient matrix.

To determine the eigenvalue λ we solve the following characteristic polynomial equation:

$$\det|A - \lambda I| = 0. \tag{1.3}$$

Next we calculate the eigenvectors as $(A - \lambda_i)v_i = 0$, where each eigenvalue λ_i has a corresponding eigenvector v_i.

The eigenvalue can be written in complex form as $\lambda_i = \gamma_i + i\omega_i$, where γ_i represents the system growth rate for Eq. (1.2) and ω_i is the frequency. The linear solution to system (1.1) is given by:

$$X(t) = \sum v_i \beta_i e^{\lambda_i}, \tag{1.4}$$

where X is a vector of state variables, v_i are the eigenvectors, λ_i are the eigenvalues and β_i are constants.

Nonlinear dynamical systems possess many properties that have not been totally explored yet, such as, the sensitivity to changing initial conditions. In some situations, it is still not possible to find accurate solutions. However, it is possible to find equilibrium solutions in some cases e.g. systems with small perturbations.

1.2.1 Stability of Dynamical Systems

The stability of a particular solution of a dynamical system depends upon the system's equilibrium points.

Let us first define an equilibrium point.

Assume $X^* \in \mathbb{C}$, ($\mathbb{C}$ represents the complex numbers), if $f(X^*) = 0$, X^* called an equilibrium point.

As a result the left-hand side of the system (1.1) equals to zero, $\dot{X} = 0$ so the changing rate in X is equal to zero when $f(X) = 0$. Consequently, there is no change in the system's solutions if we are driving it from the equilibrium point.

The equilibrium point of the dynamical system X^* is asymptoticly stable if we drive the system from any point $X(t) \in \mathbf{H}$, $(\mathbf{H} \subset \mathbb{C})$, then X converges to the equilibrium point X^*, and X^* is globally stable if $\mathbf{H} = \mathbb{C}$.

1.2.2 Linearised Differential Equations

Given a dynamical system (1.1), **the Jacobian matrix** of $f = (f_1, f_2, \ldots, f_n)$ at a point $X^* \in \mathbb{C}$ is defined by:

$$J = \begin{pmatrix} \frac{\partial f_1}{\partial x_1} & \frac{\partial f_1}{\partial x_2} & \cdots & \frac{\partial f_1}{\partial x_n} \\ \frac{\partial f_2}{\partial x_1} & \frac{\partial f_2}{\partial x_2} & \cdots & \frac{\partial f_2}{\partial x_n} \\ \vdots & \vdots & \ddots & \vdots \\ \frac{\partial f_n}{\partial x_1} & \frac{\partial f_n}{\partial x_2} & \cdots & \frac{\partial f_n}{\partial x_n} \end{pmatrix}$$

The linear stability of the equilibrium point X^* that belongs to the differential equations (1.1) is determined by the eigenvalues of the Jacobian matrix.

The equilibrium point is asymptotically stable in the case where all eigenvalues λ_i of the Jacobian matrix have negative real parts. In such a case the system is exponentially stable near equilibrium.

The equilibrium point is unstable if even one of the eigenvalues has a positive real part.

Purely imaginary eigenvalues can not be calculated by the linearisation method at the equilibrium point Apety (2011).

1.2.3 Dissipative Systems

The concept of **a dissipative** dynamical system has a remarkable interest in some fields such as engineering and physics. Dissipation theory, which specifies dissipative systems from general dynamical systems, results in a substantial restriction on their dynamical behaviour. Electrical networks are typical examples of dissipative dynamical systems. In these systems, electrical energy is converted into thermal energy in the form of dissipation as heat Willems (1972).

Suppose we have the set of equations as defined in the system (1.1) where divergence is defined as

$$(\nabla.f) \equiv \frac{\partial f_1}{\partial x_1} + \ldots + \frac{\partial f_n}{\partial x_n}.$$

If the divergence has a negative value $\nabla.f < 0$, the system (1.1) is called a dissipative system. This is true if the variable perturbations are small.

1.2.4 Fourier Transform

The Fast Fourier transform (FFT) is extremely useful in applied mathematics. By definition, Fourier analysis involves the transformation from the time domain to the frequency domain Dym and Mckean (1972),

$$\begin{aligned} F\{\upsilon(t)\} &= \int_{-\infty}^{\infty} \upsilon(t) e^{-i\omega t} dt \\ &= \tilde{\upsilon}(\omega). \end{aligned}$$

A similar process is used to calculate the inverse Fourier transform,

$$\begin{aligned} F^{-1}\{\tilde{\upsilon}(\omega)\} &= \frac{1}{2\pi}\int_{-\infty}^{\infty} d\omega\tilde{\upsilon}(\omega)e^{i\omega t} \\ &= \upsilon(t). \end{aligned}$$

1.2.5 Frequency Spectrum

The signal in the frequency spectrum domain is represented by the frequency spectrum. A frequency spectrum is generated by the Fourier transform and the respective inverse Fourier transform completely reproduces the original function. For better reproduction, the amplitude and phase of each frequency component must be preserved. The fast Fourier transform (FFT) is applied to generate frequency spectra. The FFT produce complex numbers which represent a length and direction (amplitude and phase) of the output signal.

Both linear and nonlinear operations are easier to analyse in the frequency domain as compared to the time domain.

It takes a long time to determine the signal in the time domain while we can find the signal behaviour easily using the frequency power spectrum. For instance, a periodic signal appears as a unit pulse in the frequency domain.

1.2.6 Bifurcations

Bifurcation means the separation of a system (locally / globally) into two sets of behaviour. Bifurcation of a dynamical system is a phenomenon where varying parameters produce a qualitative change in a system's dynamics.

In real life, we can demonstrate the flow in a circular cylinder linked by a smooth sphere from the middle as an example. Let us suppose viscous fluid is flowing smoothly through the cylinder past the sphere. There are two cases:

- If the fluid is running slowly, then the fluid changes its behaviour suddenly and becomes periodic.

- If the running increases, the flow becomes more and more complicated, leading to turbulent flow.

In this model, the only element changed in the dynamical system is the grid size that may be considered as a parameter which causes the bifurcation.

Let $f(x)$ be a solution to a dynamical system, and assume the solution depends on the parameter μ. The bifurcation, in this case, is a phenomenon which occurs for a specific value of μ which is called the bifurcation parameter.

Hopf bifurcation is a local bifurcation in a fixed point of a dynamical system which becomes unstable as a pair of complex conjugate eigenvalues of the linearisation around the fixed point crossing the imaginary axis of the complex plane.

1.2.7 Resonance

Resonance is a phenomenon that happens in a dynamical system when the driving frequency of oscillation is equal to the natural frequency, giving rise to high amplitudes. The concept of resonance is normally used in physics for states where a dynamical system produces periodic oscillations at some output frequency equal to the driving frequency Benzit et al. (1981).

Many pieces of research investigate the occurrence of resonance in nonlinear dynamical systems in the presence of driving forces. In the case of controlling dynamical systems using time-dependent parameters, the Lorenz system has an efficient response motion. In particular, the stochastic resonance appears as a consequence of the cooperation between the system's internal mechanisms and the external periodic forcing. This phenomenon appears in many systems, which are likely to have exciting applications of interest in different fields.

Scheiner and Galileo first observed sunspots after the significant scientific breakthrough in Europe which began with the invention of the telescope. It was an unusual occurrence that took place in the second half of the $17th$ century when sunspots became a rarity. Some researchers believe that the remarkably cold weather during those years was linked to their disappearance. The magnetic field in sunspots was studied for the first time by George Hale Hale (1908). Recently, many applications of the relationship between climate change and sunspots have taken place. The evidence for such an effect is increasing Bond et al. (2001), Haigh (1999). Most researchers have attributed the creation of magnetic fields in the Sunspots to the effect of an α - turbulent dynamo, due to the α- dynamo theory which was produced by Parker (1955).

As a consequence of Parker's theory, Weiss et al. Weiss et al. (1984) modelled the solar cycle behaviour as a $6th$-order Lorenz system with nonlinear terms, where D represents α effect of the Sun rotation defined as;

$$D = \alpha^{*}\Omega^{*}L^{4}/\eta^{2}$$

The dynamo number D is the control parameter of the system. It plays a role in producing the poloidal field from the toroidal field.

Previous studies have assumed D to be a constant Weiss et al. (1984), Jones et al. (1985). However, D might be time-dependent because the α effect might change over time. This thesis is focused on the numerical study of the Lorenz system, which represents the magnetic field components (poloidal and toroidal) and differential rotation. Several modified techniques are applied to control the nonlinear complex- valued Lorenz system.

§ 1.3 The Lorenz System

In 1963, the meteorologist Edward Lorenz introduced one of the classic representations of modern nonlinear dynamics in a 3D autonomous model. He originally designed his model to describe the Earth's atmospheric conditions. Since then, the Lorenz model has applications in many fields, due to its ability to produce different types of behaviour, including some unusual features, such as the famous butterfly pattern Lorenz (1963).

The Lorenz system has been widely used as a simplified model to understand some natural phenomena Yassen (2005). As a result, a large number of novel systems have been produced based on the first Lorenz system Wang and Wang (2008), Moghtadaei and Golpayegani (2012) Cuomo et al. (1993). In particular, the Lorenz system has many applications in various science disciplines, such as the weather and biological systems Jones et al. (2009), studying the sunspot period Hathaway et al. (1994), and laser studies Wu et al. (2010).

Lorenz's original paper Lorenz (1963) received much attention in many fields of science Bunimovich (2014). This is especially true in the field of astronomy, and it has been widely studied for various constant parameters Yan (2005).

In fact, Lorenz had only to look at his system's solution without plotting any figures of his results because his computer in 1963 was quite primitive. Since the

1980s, the Lorenz system has been used as a dynamic model for the solar magnetic cycle which has a dominant regular time interval of 22 years, modulated by irregular behaviour Suzuki (1998), Parker (1975).

In the last two decades, the study of the solar cycle has evolved from the traditional trend of understanding into a new intention of studying. A great amount of research is carried out on the study of the sunspots cycle.

The most interesting nonlinear system is the one that describes magnetic fields in sunspots. The Lorenz system has been used to simulate the dynamic interactions between the magnetic field components and the differential speed of rotation in the sunspots. In a Cartesian system, the production of large-scale magnetic fields can be simulated by equations that produce plane waves Parker (1979). This linear Cartesian system of differential equations can be extended by adding some nonlinear terms in order to obtain a model dynamo that is able to generate nonlinear finite-amplitude waves.

It is interesting to know the process of finding the Lorenz equations, which are used to simulate the generating of the magnetic field in sunspots. For this reason we address the Lorenz's system provenance in the following subsection.

1.3.1 Magnetohydrodynamics

A plasma is a collection of ions and electrons. It is treated as a continuum fluid in magnetohydrodynamics (MHD). In a plasma, the interaction between the magnetic field $\mathbf{B}$ and the velocity field $\mathbf{u}$ is governed by the following MHD equations:

$$\frac{\partial \mathbf{B}}{\partial t} = \nabla \times (\mathbf{u} \times \mathbf{B}) + \eta \nabla^2 \mathbf{B} \tag{1.5}$$

and the Navier-Stokes equation

$$\rho\left[\frac{\partial \mathbf{u}}{\partial t} + (\mathbf{u}.\nabla)\mathbf{u}\right] = -\nabla p + \rho g + \rho\nu\nabla^2\mathbf{u} + J \times \mathbf{B}. \tag{1.6}$$

Here,

$\mathbf{B} \in \mathbb{C}$: Magnetic field

$\mathbf{u} \in \mathbb{C}$: Velocity

$\rho \in \mathbb{R}$: Density

$\nu \in \mathbb{R}$: Kinematic viscosity

$J \times \mathbf{B} \in \mathbb{C}$: The Lorentz force term

$\rho g \in \mathbb{R}$: Gravitational force

$\eta = \frac{1}{\mu_0\sigma}$, $\in \mathbb{R}$: The magnetic diffusivity where σ is the conductivity and μ_0 is permeability.

1.3.2 The Magnetic Reynolds Number

The magnetic Reynolds number R_m is a dimensionless number, which is the ratio of the first term on the right-hand side of the induction Eq. 1.5 to the second term. The Reynolds number gives the ratio of advection of magnetic field to diffusion.

$$R_m = \frac{|\nabla \times (\mathbf{u} \times \mathbf{B})|}{\eta|\nabla^2\mathbf{B}|}$$

- In the case $R_m \ll 1$ the induction equation becomes

$$\frac{\partial \mathbf{B}}{\partial t} = \eta\nabla^2\mathbf{B}.$$

In this case, the diffusive effects are controlling the system and the magnetic field moves smoothly through the fluid, so there is no effect on the magnetic field from the fluid.

- If $R_m \gg 1$ the magnetic field is frozen into the fluid, it moves with the plasma.
  In this case, the induction equation reduces to

$$\frac{\partial \mathbf{B}}{\partial t} = \nabla \times (\mathbf{u} \times \mathbf{B}). \tag{1.7}$$

The essential principles of the dynamo process are the generation of toroidal flux from a poloidal flux through the differential rotation of the Sun at different latitudes by stretching out the poloidal field lines into the flow direction and producing the poloidal component from the toroidal in a cyclic processes.
The dynamo equation:

$$\frac{\partial \mathbf{B}}{\partial t} = \nabla \times (\mathbf{u} \times \mathbf{B}) - \eta \nabla^2 \mathbf{B} + \alpha \nabla \times \mathbf{B} \tag{1.8}$$

The magnetic field has three componants. In spherical coordenate (r, θ, φ) we can write

$$\mathbf{B} = \mathbf{B}_p + \mathbf{B}_t$$

where

$$\mathbf{B}_p = \nabla \times (0,\ 0,\ \mathbf{A}(r, \theta, t)),$$

$$\mathbf{B}_t = (0,\ 0,\ \mathbf{B}(r, \theta, t)).$$

$$\mathbf{u} = (0,\ 0,\ \Omega r \sin(\theta))$$

As

$$\mathbf{B}_p = \nabla \times \mathbf{A} = (B_r,\ B_\theta,\ 0)$$

Then

$$\mathbf{B}_p = \left(\frac{1}{r\sin(\theta)} (\frac{\partial}{\partial\theta} (A_\varphi \sin(\theta) - \frac{\partial A_\varphi}{\partial\varphi})\hat{r},\ \frac{1}{r}(\frac{1}{\sin(\theta)}\frac{\partial A_r}{\partial\varphi} - \frac{\partial r A_\varphi}{\partial r})\hat{\theta},\ \frac{1}{r}(\frac{\partial}{\partial r}(rA_\theta) - \frac{\partial A_r}{\partial\theta})\hat{\varphi} \right)$$

Hence

$$\mathbf{B}_p = \frac{1}{r\sin(\theta} \left(\frac{\partial r\sin(\theta)}{r\partial\theta} A_\varphi,\ \frac{-\partial r\sin(\theta)}{r\partial r} A_\varphi,\ 0 \right)$$

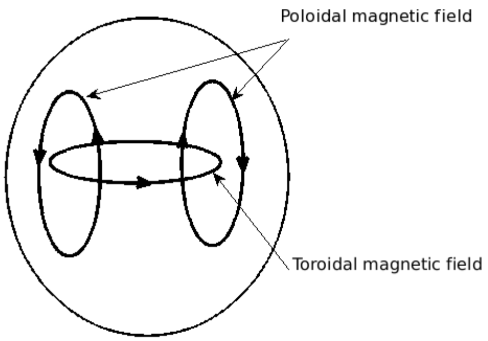

Figure 1.5: A graph illustrating the poloidal (θ) direction, represented by the vertical circle, and the toroidal (Φ) direction, represented by the horizontal circle.

- From (1.8)

$$\frac{\partial \mathbf{B}}{\partial t} = \nabla \times (\mathbf{u} \times \mathbf{B}).$$

By using standard vector identities we can write

$$\frac{\partial(\mathbf{B}_p + \mathbf{B}_t)}{\partial t} = \nabla \times (\mathbf{u} \times \mathbf{B}) = [(\nabla.\mathbf{B}) + \mathbf{B}.\nabla]\mathbf{u} - [(\nabla.\mathbf{u}) + \mathbf{u}.\nabla]\mathbf{B}$$

As there is no magnetic monopole, the divergence of the magnetic field is equal to zero, i.e. $\nabla.\mathbf{B} = 0$. Also $\nabla.\mathbf{u} = 0$.

Hence

$$\frac{\partial B}{\partial t} = r\sin(\theta)(\nabla \times \mathbf{A}).\nabla\Omega \tag{1.9}$$

- In Eq. (1.8) by letting

$$\frac{\partial \mathbf{B}}{\partial t} = -\eta\nabla^2\mathbf{B}$$

Therfore

$$\frac{\partial(\mathbf{B}_t\{\varphi\} + \mathbf{B}_p\{(r,\ \theta)\}}{\partial t} = \alpha\nabla \times \mathbf{B}_t\ \{(r,\ \theta)\} + \alpha\nabla \times \mathbf{B}_p\ \{\varphi\} \tag{1.10}$$

This leads to

$$\frac{\partial \mathbf{B}_t}{\partial t} = \alpha\nabla \times \nabla \times \mathbf{A} = \alpha\nabla(\nabla.\mathbf{A}) - \alpha\nabla^2\mathbf{A}$$

As $\nabla.\mathbf{A} = 0$

$$\frac{\partial(0,\ 0,\ B)}{\partial t} = -\alpha(\nabla^2 - \frac{1}{r^2\sin^2(\theta)})A\hat{\varphi} \tag{1.11}$$

From equation 1.10

$$\frac{\partial \mathbf{B}_p}{\partial t} = \frac{\partial(\nabla \times A)}{\partial t} = \alpha\nabla \times \mathbf{B}_t$$

We can rearrange this as

$$\nabla \times \frac{\partial(0,\ 0,\ A)}{\partial t} = \nabla \times (\alpha(0,\ 0,\ \mathbf{B}))$$

Therfore

$$\frac{\partial A}{\partial t} = \alpha B \tag{1.12}$$

From equations(1.9), (1.11) and (1.12)

$$\dot{A} = \alpha B + \eta\big(\nabla^2 - \frac{1}{r^2 sin^2(\theta)}\big)A \tag{1.13}$$

$$\dot{B} = r sin(\theta) B_p.\nabla\Omega + \eta\big(\nabla^2 - \frac{1}{r^2 sin^2(\theta)}\big)B \tag{1.14}$$

The equations (1.13) and (1.14) represent an $\alpha\Omega$ dynamo, where α represents the effects of helicity [1] and η represent the enhanced turbulent diffusivity, which is constant.

In the case $\alpha = 0$, the poloidal field **A** would decay exponentially, meaning **B** would decay to zero as well Ott (1993).

In this case the magnetic field is bounded by the Lorentz force's effect on the motion. This can cause changes in the azimuthal velocity υ, which evolves according to Eq. (1.6) as

$$\frac{\partial \upsilon}{\partial t} = F(r) + j \times B.\hat{\Phi} + \nu\big(\nabla^2 - \frac{1}{r^2 sin^2(\theta)}\big)\upsilon. \tag{1.15}$$

If we write $\upsilon = V(r) + \Psi(r,t)$ the time-independent component, V satisfies the following equation

---

[1] The helicity H of the magnetic field **B** define by the formula:

$$H \equiv \int A.BdV$$

where **A** is the vector-potential of **B** ($\mathbf{B} = \nabla \times \mathbf{A}$).

$$F + \nu\big(\Delta - \frac{1}{r^2 sin^2(\theta)}\big)V = 0.$$

Thus, Eq. (1.15) can be rewritten for Ψ as

$$\frac{\partial \Psi}{\partial t} = \frac{1}{\mu_0 \rho}\big[\nabla \times (B\hat{\Phi})\big] \times B_p.\hat{\Phi} + \nu\big(\Delta - \frac{1}{r^2 sin^2(\theta)}\big)\Psi. \tag{1.16}$$

From the equations (1.13), (1.14) and (1.16) and by choosing the magnetic field components B and Ψ as,

$$\vec{B} = (0, B(t)e^{ikx}, ikA(t)e^{ikx}).$$

We may assume that the α effect decreases as the magnetic field grows, hence

$$\Psi(t) = \Psi_0(t) + \Psi(t)e^{2ikx}.$$

Equations (1.13), (1.14) and (1.16) can be put in the following 7th-order system

$$\begin{aligned}
\dot{A}(t) &= 2DB(t) - A(t) \\
\dot{B}(t) &= i(1+\Psi_0)A(t) - 0.5iA^*\Psi(t) - B(t) \\
\dot{\Psi}(t) &= -A(t)B(t) - \nu\Psi(t) \\
\dot{\Psi}_0(t) &= 0.5(A^*(t)B(t) - A(t)B^*(t)) - \nu_0\Psi_0(t).
\end{aligned} \tag{1.17}$$

In the above equations, Ψ_0 is a real variable, while A, B and Ψ are complex, and ν and ν_0 are constants.

The system (1.17) is $7th$-order and has an exact periodic solution Sood and Kim (2013). This system can be reduced into a $5th$-order system by letting $\nu \to \infty$ then $\Psi \to 0$.

Also, the system (1.17) can be written as a $6th$-order system, in case $\nu_0 \to \infty$, this leads to $\Psi_0 \to 0$. In this study, we focus on the second case.

The dynamical system consisting of the $6th$-order differential equations is given as:

$$\begin{aligned} \dot{A}(t) &= 2DB(t) - A(t), \\ \dot{B}(t) &= iA(t) - 0.5iA^*\Psi(t) - B(t), \\ \dot{\Psi}(t) &= -iA(t)B(t) - \nu\Psi(t). \end{aligned} \tag{1.18}$$

Here, A, B and Ψ are complex variables, representing the poloidal and toroidal magnetic fields, and the differential speed of rotation, respectively. Ψ has double the frequency of magnetic fields A and B. A^* is the complex conjugate of A. ν is a real constant which represents the viscosity of the flow. D is the control parameter. Different techniques have been applied to the Lorenz system that give different types of behaviour, such as damping, periodic, and chaotic oscillation. Jones et. al. 1984 Weiss et al. (1984), studied the $6th$-order nonlinear Lorenz model for a constant D. They found that the Lorenz system in plane geometry has a Hopf bifurcation when $D = 1$, which results in to a periodic solution for $D > 1$, followed by a second bifurcation at $D = 2.07$. Further increasing the parameter D leads the system's solution to an unstable state and gives chaotic behaviour for $D \geq 3.84$.

Our study will use the $6th$-order Lorenz model that is presented in Weiss et al. (1984). For more details can be found in Weiss et al. (1984), **?**.

1.3.3 Bifurcation Diagram of the Lorenz System

The bifurcation diagram of a system is a summary of the sequence of behaviours as the control parameter increases.

Fig 1.6 illustrates the bifurcation diagram of the Lorenz system as a function of D. At each value of the parameter D on the Y-axis, the diagram provides different values that are obtained after several hundred thousand iterations.

As can be seen, a small difference in the parameter D changes a steady solution to a chaotic solution.

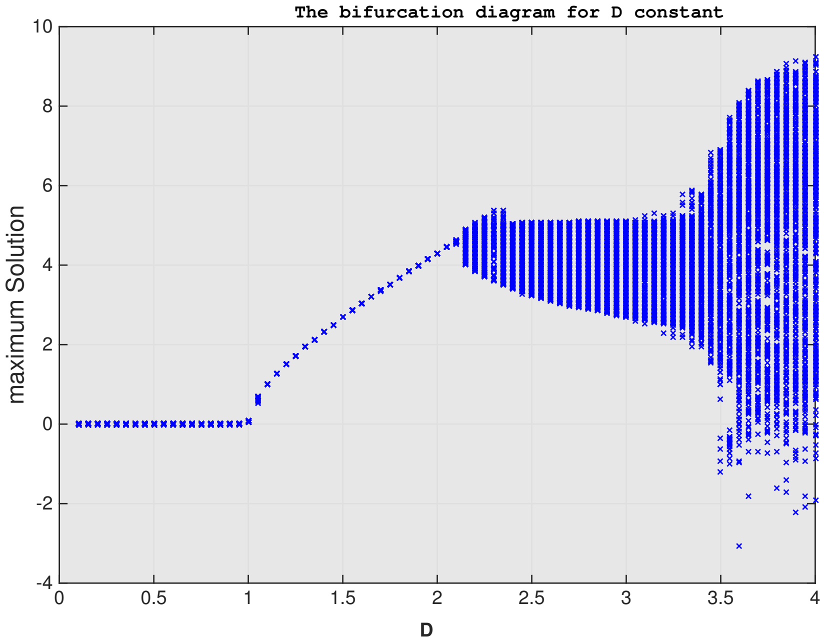

Figure 1.6: Bifurcation diagram for $0 < D < 4$.

We see that for $D < 1$, all the points are located at zero, which is the only attractor point for $D < 1$. For $1 < D < 2.07$, we can also see only one fixed point attractor. However, the attracted value increases as D increases.

1.3.4 Stability

Now to explain the system behaviour we need to study the stability of its solution. By linearize the system (1.18) around the equilibrium point (0, 0, 0) can be rewritten in the matrix form:

$$\frac{d}{dt}\begin{pmatrix} A \\ B \\ \Psi \end{pmatrix} = \begin{pmatrix} -1 & 2D & 0 \\ i & -1 & 0 \\ 0 & 0 & -\nu \end{pmatrix}\begin{pmatrix} A \\ B \\ \Psi \end{pmatrix}$$

Thus, the characteristic polynomial is given by

$$\begin{vmatrix} -1-\lambda & 2D & 0 \\ i & -1-\lambda & 0 \\ 0 & 0 & -\nu-\lambda \end{vmatrix} = 0,$$

which gives eigenvalues

$$\lambda = -\nu, -1 \pm \sqrt{D}(i+1).$$

It is obvious that when $\lambda = -\nu$ the system is stable while the positive square root causes instability. Clearly the solution is stable for $D \leq 1$ and unstable for $D > 1$ (as for $D > 1$ $\lambda > 0$). The global stability can be studied by considering a suitable Lyapunov function:

$$L \equiv \sigma^{-1}|A|^2 + 2|B|^2 + |\Psi|^2.$$

Thus,

$$\frac{dL}{dt} = -|2B - \{D + i\}A|^2 - 2\nu|\Psi|^2 + \frac{4D^2}{3}|A|^2.$$

Hence the $6th$-order system (1.18) always decays provided $D < 1$, this clearly seen in Fig. 1.6.

1.3.5 The system's features

The system has some important fundamental features as outlined below:

- The system (1.18) is dimensionless.
- It is autonomous, meaning that time does not explicitly appear on the right-hand side of the equations.
- The system has a dissipative structure, satisfying the following inequality:

  $$\frac{\partial \dot{A}}{\partial A} + \frac{\partial \dot{B}}{\partial B} + \frac{\partial \dot{\Psi}}{\partial \Psi} = -(\nu + 2) < 0.$$

  Since ν is a positive constant, the system's solutions are bounded.
- The system is symmetric under the transformation
  $(A,\ B,\ \Psi,\ D,\ F) \to A^*,\ \ -B^*,\ \Psi^*,\ \ -D,\ \ -F)$
- After linearisation of the equations around zero, the eigenvalues are

  $$\lambda = -\nu, -1 \pm \sqrt{D}(i + 1). \tag{1.19}$$

This implies that, as time increases, instability happens only from the positive real eigenvalue in the positive square root. Hence, the trivial solution for $|D| < 1$ is stable.

Due to the changes we made to the system (1.18), it can produce different kinds of behaviour including chaos within different ranges of parameter values.

For constant $D > 1$, the system has a nonlinear periodic solution which becomes unstable as D is increased for $\nu < 1$ Weiss et al. (1984). Besides, the system generates chaotic behaviour for the most common value of $\nu < 1$. The solutions to this system are nonlinear dynamo waves, a trivial solution $A = B = \Psi = 0$ also exists for constant D at $D < 1$ Weiss et al. (1984). Also, Jones et al. Jones et al. (1985) found the existence of a sequence of bifurcations as the parameter D is increased from zero; conditioned on $\nu < 1$.

The set of equations (1.18) have no analytic solutions for $D > 2.07$ Jones et al. (1985) due to nonlinearity, which plays an essential role in the solution's stability. Analytic solution for $D < 2.07$ is shown in Jones et al. (1985).

As a consequence, it becomes complicated to determine the system's solution using manual techniques. As a result, numerical solution is the only way to solve such a system.

In this work, we have solved the set of equations (1.18) on MATLAB and IDL, by using the Runge-Kutta (RK45) method with small time steps (0.001). A typical value of the parameter $\nu = 0.5$ is chosen, as was used in many previous studies, such as Jones et al. (1985) Mohamed and Kim (2014), to ensure chaotic behaviour.

Here, we used $(A(0),\ B(0),\ \Psi(0)) = (0, 1, 0)$ as an initial condition. Although the initial condition is fixed throughout this numerical simulation, varying these values does not change the solution for a sufficiently long intervals of time.

In particular, we modify the Lorenz system is presented by Jones et al. (1984) Weiss et al. (1984) as follows:

- First, by changing the constant D to be a time-dependent parameter as $D = D_0 \cos(\omega_1 t)$ in Chapter 2.

- Second, we have extend the study by choosing the parameter to be a combination of a constant and a time-dependent parameter as $D = D_0 + C_0 \cos(\omega_1 t)$ in Chapter 3.

- Furthermore, we have combined internal and external time-dependent parameters, by using $D = C_0 \cos(\omega_1 t)$ and adding $F = F_0 \cos(\omega t)$ into the first Equation in the Lorenz system 1.1 , we investigate the system response to such parameters in Chapter 4.

In Chapters 2/3 A and B have identity solutions, however, in Chapter 4 our extension of the system, as well as changing it's mechanisms, turns the system from identity solutions for A and B into different behavioural structures/trends for some range of for some ranges of the parameters value.

Chapter 2

Oscillatory Control Parameters

Abstract

For a better understanding of the role of control parameters in nonlinear dynamical systems, we numerically examine the effect of the oscillatory control parameter $D = C_0 \cos(\omega_1 t)$ on the Lorenz model for a dynamo, where C_0 and ω_1 are the driving amplitude and frequency, respectively. Although the mean value of D is zero, finite-amplitude solutions are found for sufficiently large C_0 and small ω_1. Overall, smaller C_0 and higher ω_1 are less efficient in generating finite-amplitude solutions. Also, the bifurcation in the system's solutions occurs at a larger value of C_0 and a smaller value of ω_1. Furthermore, we found a linear relationship between C_0 and ω_1 for the transition between finite-amplitude and damping solutions.

§ 2.1 Introduction

The Lorenz system was used as a dynamo model for the solar magnetic cycle which shows a dominant 22-year regular period modulated by irregular behaviour Hathaway et al. (2009),Suzuki (1998). Specifically, this model describes the evolution of two components of a magnetic field, A and B, and the differential angular speed of rotation Ψ, which are governed by the following non-linear ordinary differential equations:

$$\begin{aligned} \dot{A}(t) &= 2DB(t) - A(t), \\ \dot{B}(t) &= iA(t) - 0.5iA^{*}\Psi(t) - B(t), \\ \dot{\Psi}(t) &= -iA(t)B(t) - \nu\Psi(t). \end{aligned} \tag{2.1}$$

$A(t)$ and $B(t)$ represent the poloidal and toroidal magnetic fields, respectively; $\Psi(t)$ is the differential angular speed of rotation. All these variables are complex. A^{*} denotes the complex conjugate of A Jones et al. (1985). In this set of equations (2.1) the magnetic field generation depends on the parameter D, which is known as the dynamo number. In this research D is taken to be the main control parameter.

The set of equations (2.1) have the following two properties:

(1) They are symmetric under the transformation $(A, B, \Psi, D) \rightarrow (A^{*}, -B^{*}, \Psi^{*}, -D)$.

(2) Due to this symmetric property, the dynamics governed by a negative D has a corresponding positive value, so it is sufficient to consider the behaviour for positive D (i. e. $D \geq 0$).

The solution of the given set of equations (2.1) has a finite-amplitude solution with non-linear oscillations Jones et al. (1985), Thomas and Weiss (2004).

After ignoring the quadratic terms of the set of equations (2.1), a linear analysis for constant D is given by:

$$\frac{d}{dt}\begin{pmatrix} A \\ B \\ \Psi \end{pmatrix} = \begin{pmatrix} -1 & 2D & 0 \\ i & -1 & 0 \\ 0 & 0 & -\nu \end{pmatrix}\begin{pmatrix} A \\ B \\ \Psi \end{pmatrix}$$

which gives the following eigenvalues:

$$\lambda \in \{-\nu, -1 \pm \sqrt{D}(i+1)\}. \tag{2.2}$$

This implies that for $D < 1$, the solutions damp in time, approaching the stable solution $A(t) = B(t) = \Psi(t) = 0$ as $t \to \infty$, when $D = 1$, the solution is marginally stable.

In the presence of non-linear terms it gives rise to the first bifurcation along with linear frequency value $\omega_0 = 1$ [1] at $D = 1$, while the second bifurcation occurs at $D = 2.07$ where the famous pattern of a butterfly wing appears. If the parameter D goes on increasing further, the attractor structure becomes more and more complex. Ultimately it leads towards chaos at $D \approx 3.84$, see e.g. Jones et al. (1985), Weiss et al. (1984).

While the case of constant D has been extensively studied, the situation has not been studied well for what happens when D varies in time, with a zero mean value.

---

[1] ω_0 represents the system's frequency for D constant ($\omega_0 = \sqrt{D}$

It is important to note that the parameter D captures the overall effect of small-scale dynamics and is called the transport coefficient or the dynamo number Boccaletti et al. (2000), Proctor (2007), Bhattacharyaya and Bhattacharjee (2001), Newton and Kim (2012). The parameter D can vary in time as the transport coefficient is not guaranteed to be constant (e.g. see, Douglas et al. (2013), Becker and Kremer (1996), Graham (1982)). It is the main focus of this chapter to look into this matter and to examine whether the time-dependent control parameter D can alone be lead to the finite-amplitude solutions, and if so, then how these solutions can be related to the amplitude as well as the frequency of the parameter D. For this reason, in this chapter, we consider oscillatory D parameters of the form $D = C_0 \cos(\omega_1 t)$ for fixed as $\nu = 0.5$. As the multiplicative control parameter D is present, analytical solutions of the non-linear system are not possible and hence we perform numerical simulations. As the parameter D is dependent upon the amplitude C_0 and frequency ω_1, in section 2.2, for a fixed ω_1 the amplitude C_0 is varied, while in section 2.3 for a fixed C_0, the frequency ω_1 is varied.

In both cases, system (2.1) is solved with the help of the Runge-Kutta-Fehlberg (RKF45) method with a suitably small time step i.e. 0.001 for sufficient numeric accuracy, and the amplitude and frequency power spectra are computed from the time history of A, B, and Ψ. Moreover, the relation between C_0 and ω_1 is established for bifurcation, which are also found in simpler systems Newton and Kim (2012), Douglas et al. (2013). It can be seen that the reported relation brings up the transitions between finite-amplitude and damping solutions which are shown as being distinct from the amplitude death for damping of oscillation Guo-Lin and Wen-Ping (2007).

§ 2.2 Results for Fixed ω_1

As discussed above, when D is constant, linear instability appears for $D > 1$ along with finite-amplitude solutions. Equations (2.1) indicate that the frequency for this solution is $\omega_0 = 1$. Here, we studied the response of the system by considering two different cases for ω_1. The first case is when the driving frequency ω_1 is smaller than $\omega_0 = 1$, while in the other case ω_1 is larger than $\omega_0 = 1$. Specifically, by varying C_0, equations (2.1) are solved numerically for $\omega_1 = 0.5$ in section 2.2.1 and $\omega_1 = 10$ in section 2.2.2.

2.2.1 $\omega_1 = 0.5$ WITH VARYING C_0

In this case, the driving frequency ω_1 is lower than $\omega_0 = 1$. The behaviour of the system becomes complicated increasing values of C_0 from zero. In the interval $C_0 < 1.78$, the solutions of the system (2.1) rapidly evolve to the trivial equilibrium point $(0, 0, 0)$. This is the expected damped solution for the oscillatory control parameter having mean value zero. With further increases in C_0, the system bifurcates into finite-amplitude solutions and at $C_0 \approx 1.78$, there exists the first bifurcation where the observed periodic oscillation has frequency 0.5. This obtained output frequency i.e. 0.5 equals to the driving frequency $\omega_1 = 0.5$. In Fig. 2.1, the Poincaré section is clearly shown as red circles[2]. It is very interesting to note that these circles are positioned on top of each other and in such a way they indicate that the output frequency and the driving frequency are the same.

---

[2] A Poincaré section is used in this part to detect some structure in the system's attractors.

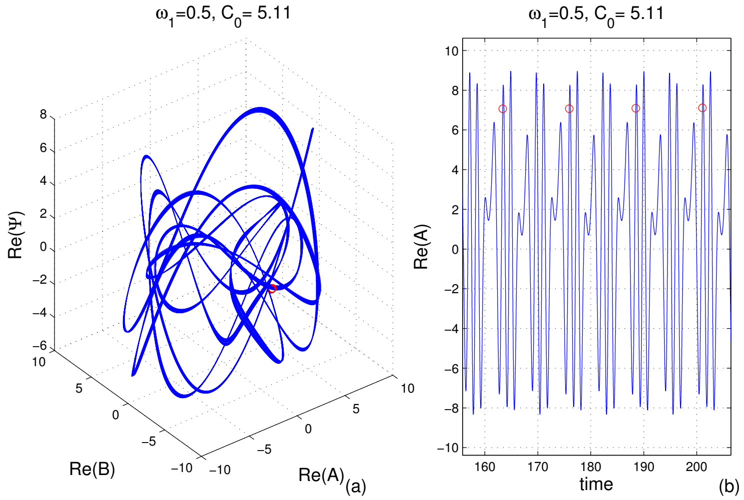

Figure 2.1: (a) Phase-space of Re(A), Re(B) and Re(Ψ) for $C_0 = 5.11$. (b) Time series of Re(A) for $C_0 = 5.11$.

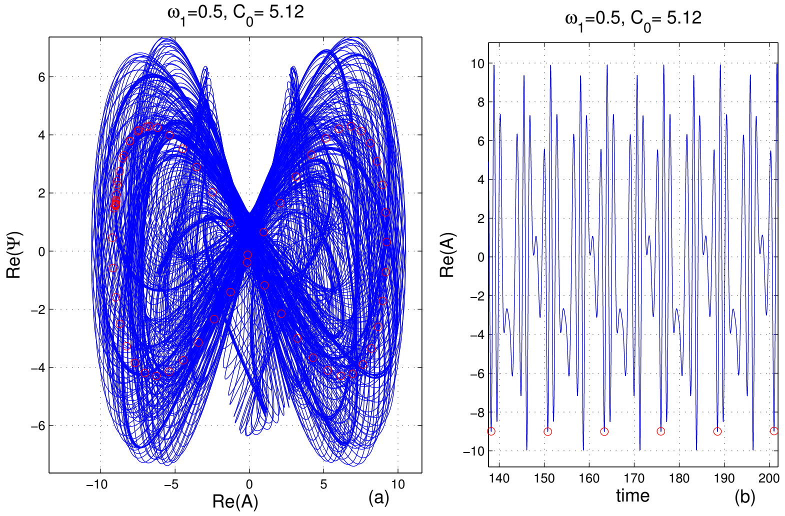

Figure 2.2: (a) Quasi-periodic solution of (2.1) for $C_0 = 5.12$. (b) Time series of Re(A) for $C_0 = 5.12$. The Poincaré sections for $\omega_1 = 0.5$ are denoted by red circles.

Further increasing the value of C_0 gives rise to phase trajectories that are more complex, indicating that the toroidal and poloidal magnetic fields have chaotic behaviour. At the particular value $C_0 \approx 2.68$, the system experiences a second bifurcation and ultimately becomes chaotic. As Fig. 2.1 shows, further increased value, i.e. at $C_0 = 5.11$, the solution is again periodic with different values of the frequency and amplitudes. When C_0 exceeds slightly above $C_0 = 5.11 - 5.12$, the periodic oscillations become quasi-periodic while in Fig. 2.2 the red circles represents the Poincaré section having an oval twist due to the output frequency. This demonstration tells us that the solution is sensitive to a slight change in the values of the parameter C_0. Moreover, further increasing the value of C_0 leads to complex behaviour by making the attractor of the system more complex. At $C_0 \approx 6.56$, a changeover to a chaotic state takes place. As the system experiences bifurcations of a different kind by increasing C_0, all bifurcations can not be determined easily. This is because with a small change in C_0 there occurs a rapid change in their behaviour.

If we compute a frequency spectrum of B for a fixed C_0 value and find the frequency where there is the maximum amplitude spectrum, then we can understand the overall behaviour of the system. The frequency spectrum can be computed with the help of a fast Fourier transform (FFT) of the time series of variable B. The plot of this dominant frequency, for maximum intensity of B as a function of C_0 is shown in Fig. 2.3.

As an interesting fact, the dominant frequency appears almost constant before exceeding a value of 0.5 with increasing C_0. The constant frequency between succeeding jumps is due to mode-locking (e.g. Rajasekar and Lakshmanan (1988)). Therefore, the system is controlled by the driving frequency $\omega_1 = 0.5$ by keeping the dominant frequency as an integer multiple of the driving frequency in a small region by mode-locking. In a non-linear periodically forced oscillator, such jumps were also observed (i.e. Van-del Pol oscillator Rajasekar and Lakshmanan (1988), Parlitz and Lauterborn (1987)).

In Fig. 2.3, the dominant frequency shows a rough representation of the systems behaviour over time, as for any fixed value of C_0, the frequency can have a wide spectrum with multi-peaks. Therefore, for different values of C_0, the intensity of the frequency spectrum is shown in Fig. 2.4 with colour, where a high intensity is represented by yellow. For the dynamical variable B, firstly we obtained a time series for each value of C_0 to attain that frequency where the intensity for B is maximum.

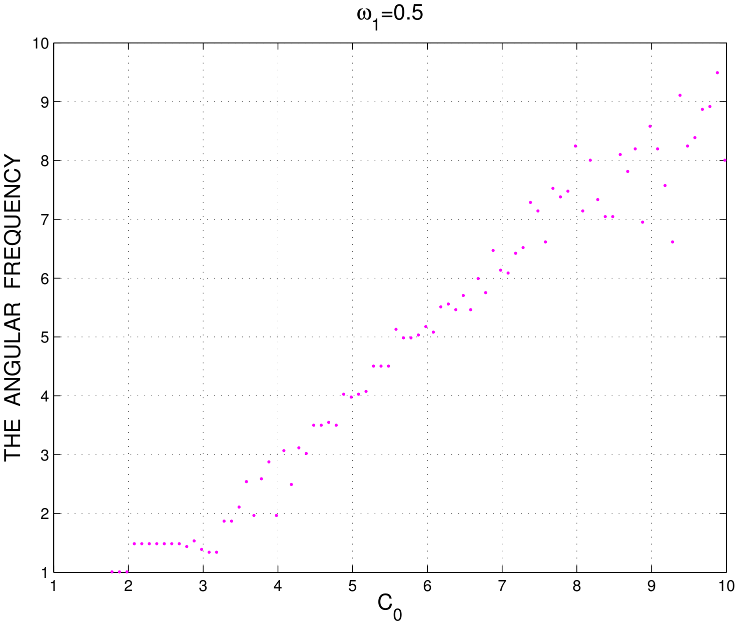

Figure 2.3: The dominant frequencies of B for $\omega_1 = 0.5$.

To obtain the frequency of the maximum intensity for B, first we obtain a time series of the dynamical variable B for each C_0 . Using (FFT) we find a Fourier series of B to compute the power spectrum of the frequency for each C_0. Once a power spectrum is obtained for each C_0, colours are assigned according to the colour coding as shown in the bar next to the figure, where the frequency of the maximum intensity to low intensity is represented by yellow to dark colours. When zoomed in, multiple maxima separated by integer multiples of the driving frequency $\omega_1 = 0.5$ are observed for small $C_0 < 2.5$. A region of the brightest yellow in Fig. 2.4 shows that the frequency of high intensity increases almost linearly with C_0, similar to the behaviour demonstrated in Fig 2.3.

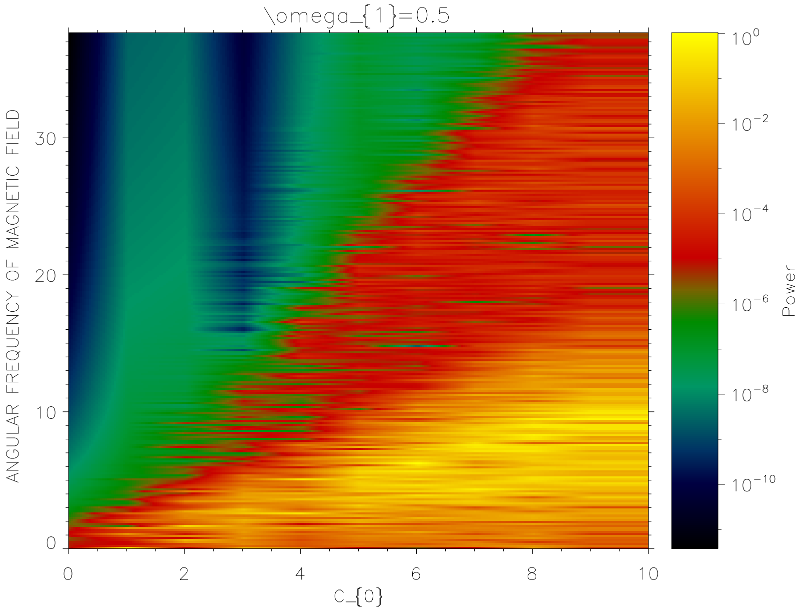

Figure 2.4: The frequency spectrum of the magnetic field against C_0 for $\omega_1 = 0.5$.

Fig. 2.4 clearly shows that the region of the frequency of high intensity gradually becomes wider as C_0 increases. Furthermore, it also shows that the entire frequency spectrum significantly broadens to higher frequencies around $4 < C_0 < 5$. This broadening is interestingly associated with a rapid increase in $|B|^2$ with C_0 as shown in Fig. 2.6.

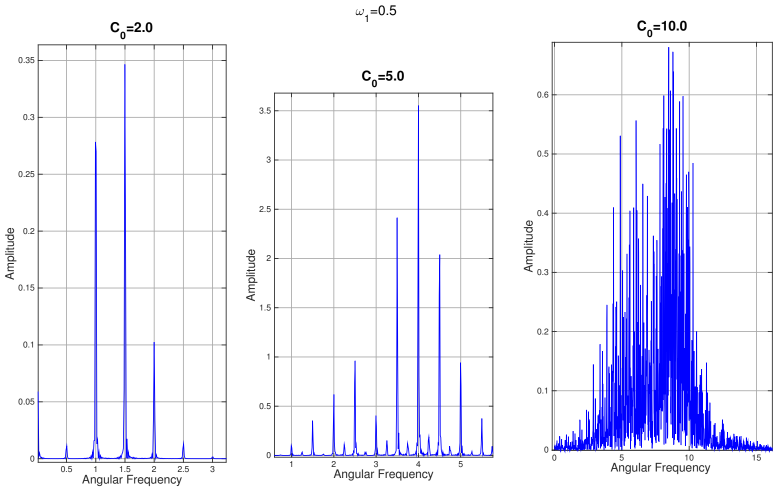

Figure 2.5: The frequency spectrum of the magnetic field for $C_0 = 2,\ \ 5$ and 10 at $\omega_1 = 0.5$.

Now we study the change in the amplitude of B with C_0. This can be computed by taking the time average of $|B|^2$ for a considerably long time and then plotting it as a function of C_0. Here an interesting behaviour appears in Fig. 2.6 that, with C_0, the overall increasing amplitude intermixed with jumps, as was observed in Fig. 2.3 for the frequency spectrum.

Overall, starting from zero amplitude for the damping case, the amplitude increases roughly linearly with C_0 for $C_0 \in (1.78, 4.3)$. It then starts increasing more quickly for $C_0 > 4.3$ where we observed the frequency spectrum to become broader suddenly as mentioned above. For further increased value of C_0 there is a gradually slower increase in amplitude.

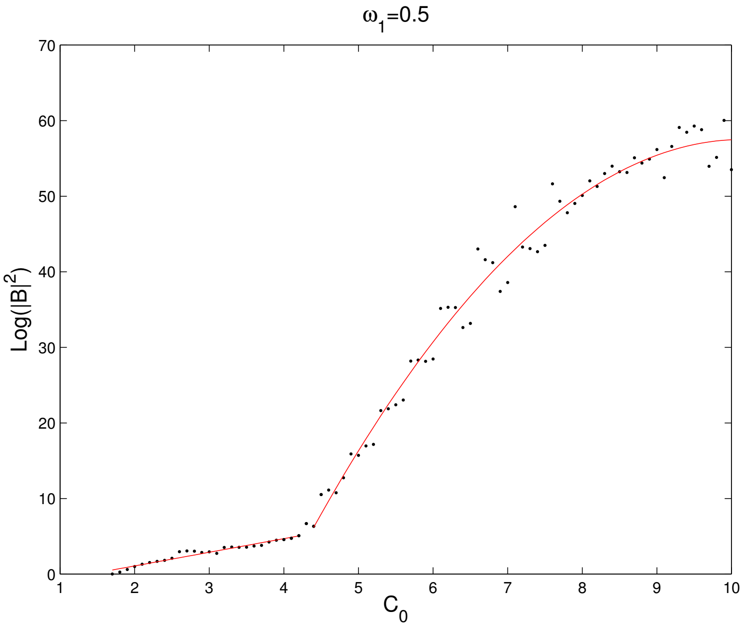

Figure 2.6: The amplitude of $Log(|B|^2)$ against C_0 for $\omega_1 = 0.5$.

2.2.2 $\omega_1 = 10$ WITH VARYING C_0

We consider $\omega_1 = 10$, a driving frequency of much higher value than $\omega_0 = 1$ and examine how the response of the system is different. We consider different values of C_0 to examine the detailed behaviour of the system.

The domain $0 < C_0 < 7.2$ gives the stable decaying solution for the system and it is the same behaviour of the system as was observed previously in section 2.1, in the interval $0 < C_0 < 1.78$ for $\omega_0 = 0.5$. At $C_0 \approx 7.2$, the first bifurcation happens along with a finite-amplitude periodic solution.

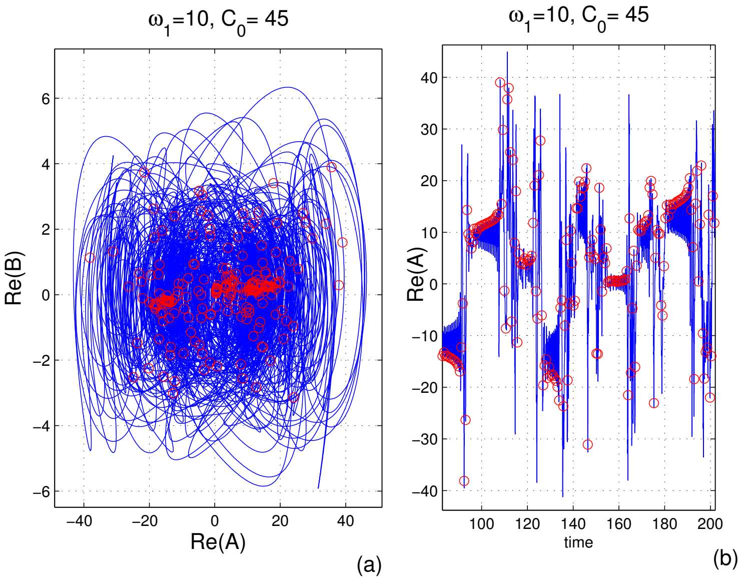

Figure 2.7: Chaotic attractors for $C_0 = 45$.

We observe from the study of the Poincaré section that the oscillation frequency is identical to the driving frequency. It is important to notice that this bifurcation at driving frequency $\omega_1 = 10$ occurs at higher value of C_0 than that for $\omega_1 = 0.5$ in section 2.2.1. This critical value of C_0 is also higher than $D = 1$ for constant D Weiss and Thompson (2009). We obtained a quasi-periodic solution at $C_0 \approx 19.4$ when the second bifurcation occurs. A more complex behaviour is observed in the interval $35 < C_0 < 45$ which involves oscillations of various types along with various values. A change to the chaotic behaviour is established for $C_0 > 43$. An example of this chaotic behaviour is shown in Fig. 2.7, that is the phase-space plot for $Re(A)$ and $Re(B)$ with the related time series for $C_0 = 45$.

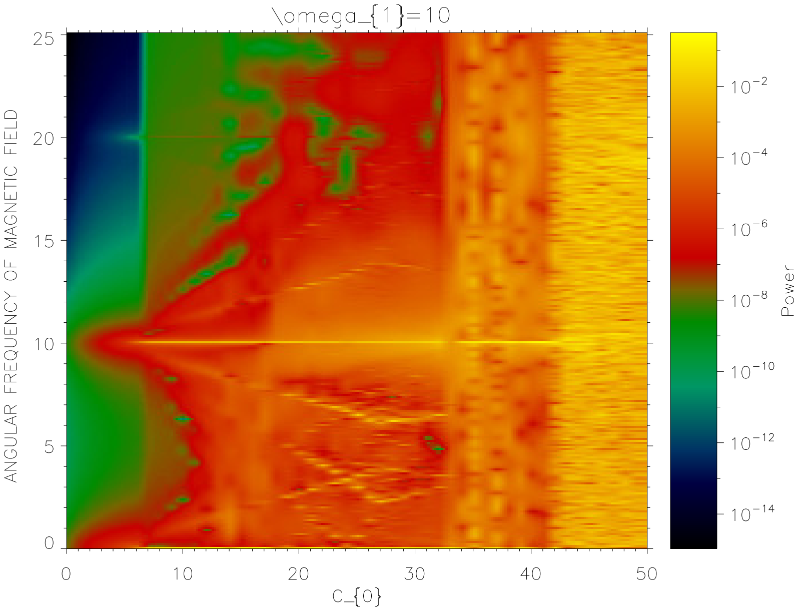

Figure 2.8: The frequency spectrum of the magnetic field against C_0 for $\omega_1 = 10$.

For the general understanding of the behaviour of the system at $\omega_1 = 10$, the frequency power spectrum is shown in Fig. 2.8, for different values of C_0. It is of great interest to notice that a bright line for high-intensity appears along a horizontal line of frequency 10, which corresponds exactly to the driving frequency. The peak at $\omega_1 = 10$ gradually becomes wider from the lower frequency side for $7.2 < C_0 < 17$ which causes the sudden broadening of the entire spectrum, firstly when $C_0 \approx 35$ and then about $C_0 \approx 43$. Reflection of these changes can also be seen in the behaviour of $Log(|B|^2)$ shown in Fig. 2.9 where at about $C_0 \approx 35$ and $C_0 \approx 43$, there occur sudden jumps in $Log(|B|^2)$.

To obtain the frequency of the maximum intensity for B, first of all, a time series of the dynamical variable B for each C_0 is obtained. Using (FFT), a Fourier series of B is found to compute the power spectrum of the frequency for each C_0. Once a power spectrum is obtained for each C_0, colours are assigned according to the colour coding as shown in the bar next to the figure, where the frequency of the maximum intensity to low intensity is represented by yellow to dark colours. When zoomed in, multiple maxima separated by integer multiples of the driving frequency $\omega_1 = 0.5$ are observed for small $C_0 < 2.5$. A region of the brightest yellow in Fig. 2.4 shows that the frequency of high intensity increases almost linearly with C_0, similar to the behaviour demonstrated in Fig.

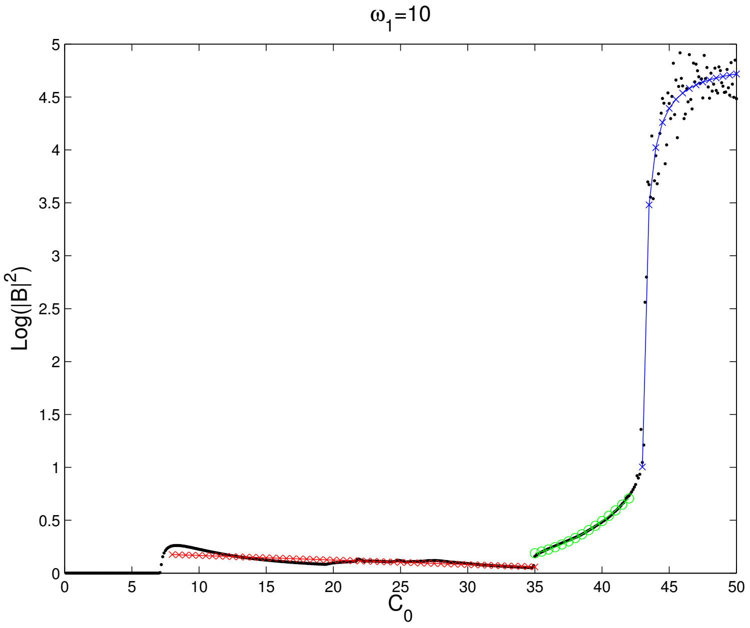

Figure 2.9: $Log(|B|^2)$ as a function of C_0 for $\omega_1 = 10$.

We now examine the amplitude of B as a function of C_0. In comparison with the lower driving frequency case $\omega_1 = 0.5$, the system in this case tends to have the smaller amplitude. Mainly, a rapidly decreasing amplitude is seen in the interval $8 < C_0 < 35$ as shown in Fig. 2.9. A Linear fit by red crosses is overplotted in this region in Fig. 2.9. This decrease is replaced a roughly quadratic increase, in the interval $35 < C_0 < 42$. After that $|B|^2$ becomes saturated by attaining a constant value about ≈ 4.5 at larger C_0, i. e. around $C_0 \approx 43$.

In this case the obtained asymptotic value is much smaller than that of the lower driving frequency case.

It is clear from these results that the smaller amplitude C_0 as well as higher frequency ω_1 are not much capable of generating finite-amplitude solutions of the Lorenz system, while the bifurcation occurring at a larger value of C_0 and smaller values of $|B|^2$. The difference in the trends between Fig. 2.6 and Fig. 2.9 reveals that the amplitude has very different behaviour with changing values of C_0. Fig. 2.9 shows the amplitude for lower frequency increases monotonically with C_0.

Moreover, in Figs. 2.8 and 2.9, the results for the frequency spectrum and amplitude imply the fundamental change in response of the system around $C_0 \approx 35$ which depends on the larger values of the frequency. Section 2.3 presents a comprehensive discussion of the dependence of the response of the system on the driving frequency.

§ 2.3 Results for Fixed C_0

As discussed earlier, higher frequency of D is generally not very efficient in generating finite-amplitude solutions for the Lorenz system. The response of the system depends on the value of the driving frequency compared with the natural frequency of the system. This section elaborates on these by studying the dependence on the frequency systematically when ω_1 is varied for two different values of C_0. Specifically, these two values are considered in such a way that for constant $D = C_0$ (i.e. $\omega_1 = 0$) they have periodic as well as chaotic attractors, and the changes that also occur in damping solution for suitably larger ω_1. It can be noted that the values of $C_0 = 2$ and $C_0 = 20$ are selected as examples of cases when a constant control parameter yields periodic and chaotic solution correspondingly.

2.3.1 $C_0 = 2$ WITH VARYING ω_1

When ω_1 increases for $\omega_1 \in (0, 2)$ the attractors are periodic but the frequencies change with ω_1. During this stage, the driving frequency is sufficiently small and can be considered as constant (in time). Around $\omega_1 \approx 2.2$, the limit cycle disappears, and the system damps quickly to the trivial equilibrium state. The frequency power spectrum in Fig. 2.10 reveals this behaviour where there appears regions in yellow multiple maximal in the interval $0 < \omega_1 < 2.2$, with the output frequencies as $n\omega_1$ $(n \in \mathbb{Z})$ i.e. an integer multiple of the driving frequency. Significantly, distinct peaks occur at the same frequencies as the driving frequency (i.e. the bottom line). For $\omega_1 > 2.2$ damping makes the spectrum really weak.

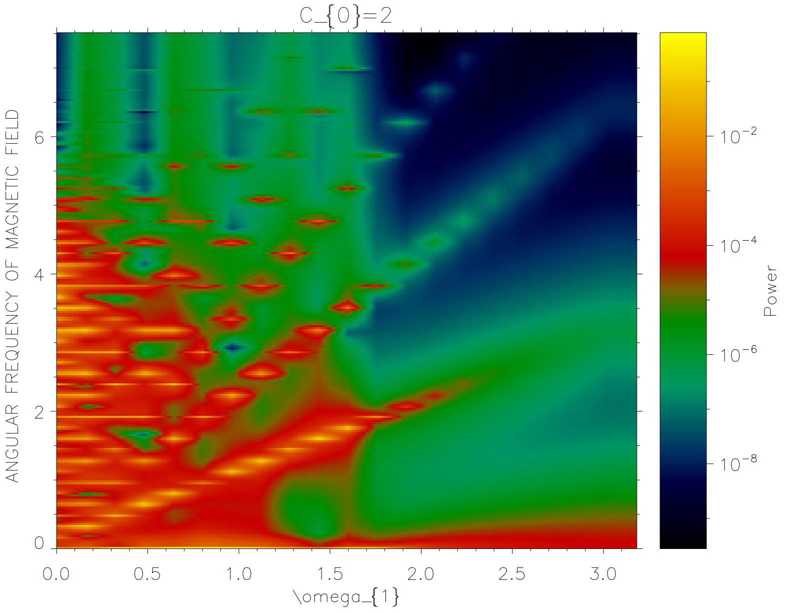

Figure 2.10: Frequency spectrum of the magnetic field as a function of ω_1 for $C_0 = 2.2$.

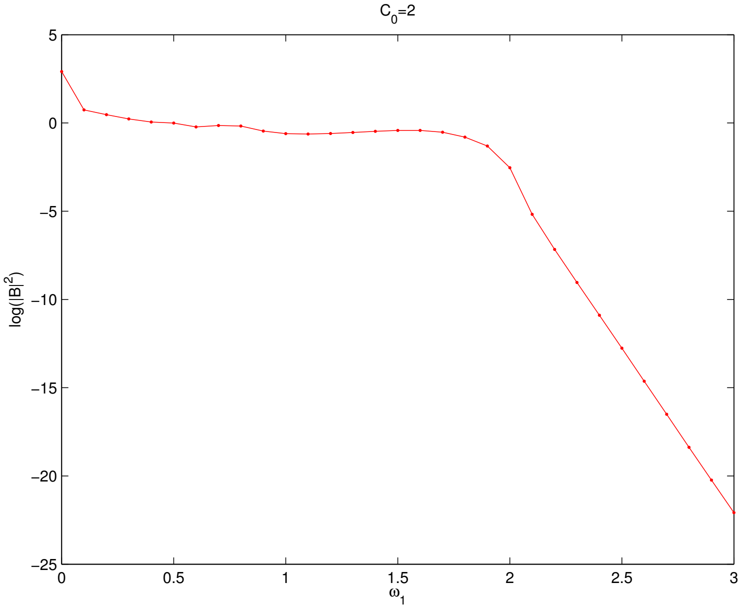

Figure 2.11: $|B|^2$ as a function of ω_1.

The drop in the solution's amplitude can be seen in Fig. 2.11 where $|B|^2$ is plotted using log scale as a function of ω_1. Around $\omega_1 \approx 2.2$, the sudden drop of $|B|^2$ is visible.

What is the reason behind the sudden change in amplitude and frequency of B at about $\omega_1 \approx 2.2$? It appears it is linked to the change of state from when the system responds coherently to the driving frequency to the state when it cannot because of the large value of the driving frequency. This is also related to our previous comment that the sufficiently small frequency $\omega_1 < 1$ in comparison with linear onset frequency is taken to be approximately constant.

2.3.2 $C_0 = 20$ WITH VARYING ω_1

Now we will study the response of the system for different driving frequencies ω_1 while the driving amplitude is fixed at a large value $C_0 = 20$. Due to a significantly larger perturbation amplitude C_0, the behaviour of the system in this case is different from the cases in section 2.3.1. The solution begins at $\omega_1 = 0$ with a chaotic orbit which is expected if D was a constant with value $D = 20$, and then around $\omega_1 \approx 13$ it bifurcates to a periodic orbit after losing the chaotic attractor. At about $\omega_1 \approx 28.29$, there occurs a transition to the damped solution. For $\omega_1 = 1$, Fig. 2.12 illustrates chaos by showing the Poincaré section red circles.

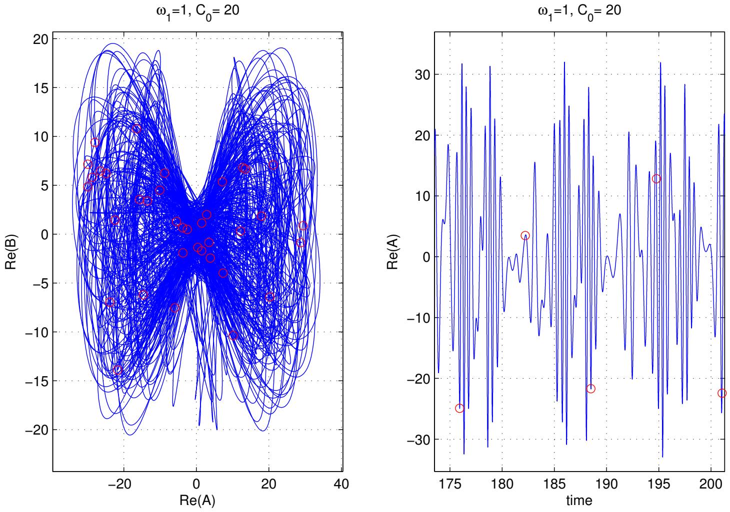

Figure 2.12: (a) 2D trajectory plot of $\mathrm{Re}(A)$ against $\mathrm{Re}(B)$ for a chaotic solution at $\omega_1 = 1$. (b) Time series of $\mathrm{Re}(A)$.

In Figs. 2.13 and 2.14, the overall behaviour of the system is summarised, in the order of the frequency spectrum and amplitude, respectively. In Fig. 2.13 the bright yellow in a broadband which is the vertical direction for small $\omega_1 < 7$ is a demonstration of chaos, which gradually weakens with increasing ω_1. This chaos is lost by the system between $7 < C_0 < 13$, and at $\omega_1 = 13$ it bifurcates to a periodic orbit. This periodic orbit lasts up to $\omega_1 = 28.29$. For $\omega_1 > 28.29$, the damped solution is represented, in Fig. 2.13, in dark colour.

How are the above changes in the frequency spectrum related to the amplitudes behaviour? In particular, for $\omega_1 < 7$, the amplitude first oscillates and then increases very slowly as ω_1 approaches 28.29. At this point, a transition to damping along with a sudden drop in amplitude occur. Here, $e^{0.1083\omega_1}$ and $e^{-3.735\omega_1}$ are two exponential functions that are fitted to the amplitude in intervals $7 < \omega_1 < 28$ and $\omega_1 > 29$, respectively. These two fitted curves, in Fig. 2.14, are plotted in blue lines.

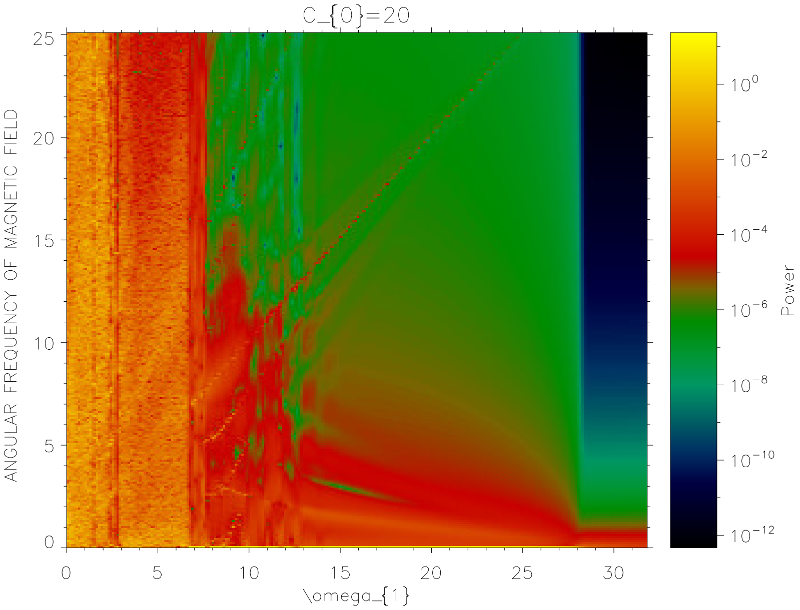

Figure 2.13: The frequency power spectrum of the magnetic field for $C_0 = 20$.

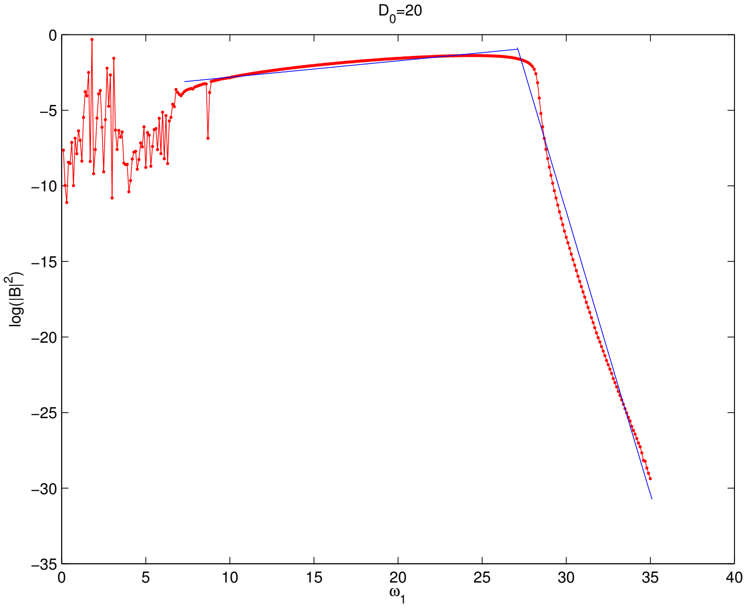

Figure 2.14: $Log(|B|^2)$ as a function of ω_1 for $C_0 = 20$.

In the interval $7 < \omega_1 < 28.29$, it seems that the change in the frequency as well as amplitude is linked to the change of state from when the system responds coherently to the driving frequency, to the state when it cannot because of the large value of driving frequency as was observed in section 2.3.1. This transition involves the bifurcation having a quasi-periodic/periodic attractor.

§ 2.4 Discussion and Conclusion

We have studied the effects of $D = C_0 \cos(\omega_1 t)$ (i.e. time-dependent) dynamo number on the solar dynamo model represented by the Lorenz system. In particular, we vary C_0 in sections 2.2 and 2.3. The parameter D depends on the amplitude (C_0) and frequency ω_1, respectively. Although D does not have a mean value in average time, for sufficiently large C_0 and smaller ω_1 the system has finite-amplitude solutions. When ω_1 is fixed and C_0 increases, we witness how the system exhibits bifurcation towards chaos. On the other hand, when C_0 is fixed and ω_1 increases the finite-amplitude solution leads to a damped solution. While generating finite-amplitude solutions, the control parameter with a smaller amplitude C_0 and a higher frequency ω_1 is found to be less efficient and a bifurcation takes place at large value of C_0 and smaller ω_1. Here an interesting question arises, as to whether these are a systematic way of compensating the effect of C_0 by ω_1 and vice versa. In order to answer this, we consider the more different values of C_0 and ω_1, and determine the point of bifurcation between a finite-amplitude solution and a damped solution.

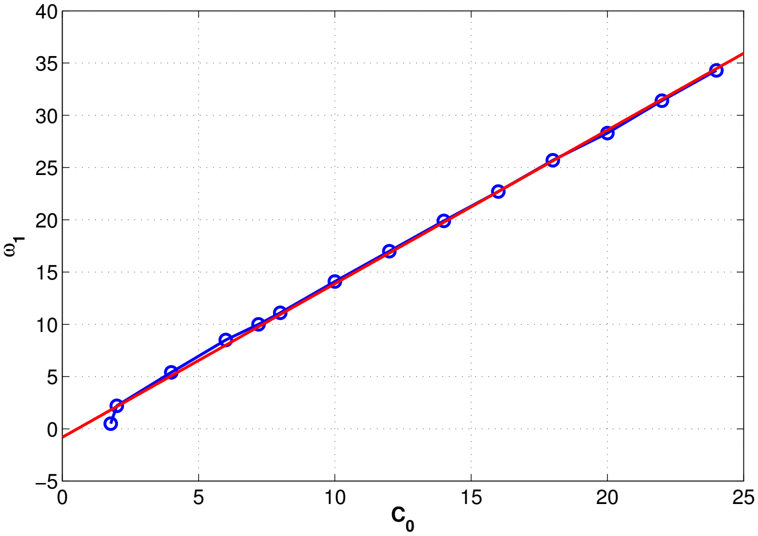

Figure 2.15: C_0 against ω_1 for the onset of a finite-amplitude solution.

Our results are shown in Fig. 2.15, where circles show the values of C_0 and ω_1 the bifurcation points. This leads us to find a linear relation $\omega_1 = 1.4465C_0 - 0.4212$ for the bifurcation points and plot it as a solid red line in Fig. 2.15. ω_1 can be altered linearly with C_0 to compensate for the effect of the change in C_0. Such a type of linear relationship was reported in a simpler nonlinear dynamo model Newton and Kim (2012) and also in a nonlinear dynamo model as well as in a non-linear dynamical model i.e. for transport barriers in laboratory plasmas Douglas et al. (2013) where an oscillatory control parameter is additive. Hence, this linear relation could be a basic aspect of periodically oscillatory perturbation in nonlinear dynamical systems that will be examined in other non-linear systems (e.g. Rössler Wang and Chen (2011), Gaspard (2005) and Chen LÜ et al. (2002)) in future work. The effect of time-dependent control parameter involving a mean part as well as an oscillatory part will also be presented in Chapter 3, where an interesting question of the effect of resonance will be examined. It is important to consider a more general case of viscosity having constant and fluctuating parts. More detail can be found in Appendix A.

2.4.1 The Damping in the Linearise Lorenz system

What is interesting in the result from the linearise Lorenz system is that the relation between C_0 and ω_1 when damping behaviour occurs almost equal that in the nonlinear which appears in Fig. 2.16.

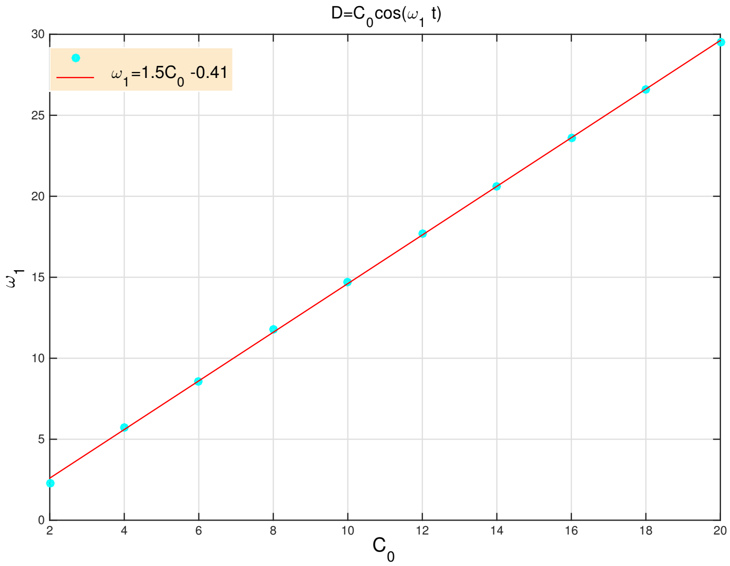

Figure 2.16: C_0 against ω_1 for the onset appear in the linearised system.

Chapter 3

Parametric Instability and Nonlinear Feedback

Abstract

We investigate the combined effect of constant and oscillatory control parameters on the complex Lorenz system. By assuming that the control parameter D consists of a constant D_0 and oscillatory part $C_0 \cos(\omega_1 t)$, we numerically study the effect of C_0 and ω_1 on the linear and nonlinear response of the complex Lorenz system for different values of D_0. Since D takes values between $D_0 - C_0$ and $D_0 + C_0$ as time changes, the system effectively can go through different attractors from damping to chaotic solutions in time, covering multiple attractors. The maximum linear growth rate is found at $\omega_1 = 4\omega_0$, where ω_0 is the natural frequency (e.g. when $C_0 = 0$) provided that C_0 is not much larger than D_0. In sharp contrast to this linear response, a non-monotonic behaviour is manifested in the nonlinear case where the amplitude and frequency of dynamical variables become minimum. An interesting relation $C_0 \approx D_0 + 1$ is found for the minimum

response in this nonlinear case as the system stays in a Dead-Zone for the longest time. The effect of the oscillatory control parameter disappears both linearly and nonlinearly for sufficiently large ω_1.

§ 3.1 Introduction

Nonlinear dynamical systems' key properties are governed by a few important control parameters Boccaletti et al. (2000), Hu et al. (2007), whose change leads to a sequence of bifurcations. For fixed control parameters, the addition of small perturbations to the system can give rise to unexpectedly interesting behaviours, some of which are even counter-intuitive Chen and Han (2003). For instance, the complexity (e.g. chaos) of the system can be increased or decreased due to a perturbation as detailed below. Depending on the situation, a perturbation to the system can be either internal or external in the form of multiplicative or additive noises, respectively. We assume that in the case of internal/multiplicative noise, the perturbation that appears in the control parameter is multiplied by a system variable.

The evidence for the physical relevance of noise, as well as its importance, has been accumulated from many different fields Simakov and Perez-Mercader (2013), Gang et al. (1993). One noteworthy reaction of noise is stochastic resonance (SR), which occurs when a nonlinear system is simultaneously driven by an external periodic force and stochastic noise Benzit et al. (1981), Neiman et al. (1997), Revelli et al. (2008). A large response of the system is obtained at certain values of the noise amplitude. This is due to a subtle synchronisation between the time scale associated with periodic forces and another important characteristic timescale, typically associated with the transition between two attractors (e.g. exit time) in the presence of the stochastic noise Anishchenko et al. (1993), Pikovsky and Kurths (1997). Even in the absence of external noise (e.g. in deterministic nonlinear systems), SR can also result from the stochasticity/chaos that arises internally in a nonlinear system Crisanti et al. (1997), Sinha (1999), Chapeau-Blondeau and Godivier (1997). Another interesting effect that has received great attention is the parametric instability in the case of a periodic multiplicative noise Priede et al. (2010), Li et al. (2004), Reimann (2004). The aim of this chapter is to extend previously reported work (e.g. Crisanti et al. (1997), Priede et al. (2010)) to a nonlinear system of complex variables and explore a wide range of parameter values, where a periodic perturbation can induce transitions among multiple attractors.

3.1.1 Model and Motivation

Our model is the complex Lorenz system, that is presented in Chapters 1 and 2 and which is given as a model for the activity of magnetic fields. This model describes how magnetic fields are produced in a conducting fluid (the so-called dynamo). These Lorenz equations have been used as a model for solar magnetic fields which exhibit a 22-year regular period modulated by irregular behaviour Letellier et al. (2006), Suzuki (1998). Specifically, it is governed by a system of six coupled ordinary differential equations (ODEs), which describe the evolution of the two components of the magnetic field, A and B, and the angular speed of differential rotation Ψ. In dimensionless form, these are given as;

$$\begin{aligned} \dot{A}(t) &= 2DB(t) - A(t), \\ \dot{B}(t) &= iA(t) - 0.5iA(t)^*\Psi(t) - B(t), \qquad (3.1) \\ \dot{\Psi}(t) &= -iA(t)B(t) - \nu\Psi(t). \end{aligned}$$

Here, $A(t)$, $B(t)$ and $\Psi(t)$ represent the poloidal and toroidal magnetic fields, and the angular speed of differential rotation, respectively. All the variables are complex. The viscosity of the differential rotation is represented by a constant parameter ν Parker (1979). The parameter D in the set of equations 3.1 is the dynamo number which is to be considered as a single (real) control parameter in our study. Previous studies Jones et al. (1985) reported that when D is constant, the first bifurcation to a non-zero finite-amplitude solution of A, B, and Ψ occurs at $D = 1$. Then the second bifurcation occurs at $D = 2.07$, followed by the appearance of periodic limit cycle solutions. As D increases further, the system's behaviour becomes more complicated towards chaos around $D = 3.84$ (e.g. Jones et al. (1985)).

In this chapter, we assume that D consists of a constant D_0 and an oscillatory part $C_0 \cos(\omega_1 t)$ as;

$$D = D_0 + C_0 \cos(\omega_1 t).$$

Here ω_1 and C_0 in D represent the driving frequency and amplitude, respectively. Our main interest is in the effect of C_0 and ω_1 on the response of the system for different values of D_0 at different bifurcation points Mohamed and Kim (2015). In contrast to previous work on (SR) in Lorenz system Crisanti et al. (1997) where periodic forcing was included in one of the control parameters (different from our control parameter D), our work is not limited to the analysis of a 'small' perturbation effect near the bifurcation point to chaos, but instead examines the effect of all possible values of ω_1 and C_0 for the two fixed values of D_0.

In the trivial case of $D_0 = 0$, D changes periodically in time, with zero time average. While no finite-amplitude solution may be expected based on the mean value, our previous study in Chapter 2/ Mohamed and Kim (2014) has shown that a purely oscillating parameter $D = C_0 \cos(\omega_1 t)$ can give rise to a finite-amplitude solution for sufficiently large C_0 and small ω_1. In particular, we have found that the effect of changing C_0 can be offset by altering ω_1 linearly with respect to C_0, higher amplitude C_0 and the smaller frequency ω_1 being more efficient in generating finite-amplitude solutions.

We have found an interesting linear relationship between ω_1 and C_0 given as $\omega_1 = 1.4465C_0 - 0.4212$ for the transition between damping and finite-amplitude solutions, similar to the linear relation obtained by Newton and Kim Newton and Kim (2012) for a simpler nonlinear dynamo model. Moreover, this linear relationship governs the point where the effect of the oscillatory parameter effectively disappears completely (i.e. $D = 0$).

We used similar parameter as $q_0 + A\sin(\omega t)$ Douglas et al. (2013).

3.1.2 AIMS AND OUTLINE

We investigate the system's response to the periodic forcing $D_0 + C_0 \cos(\omega_1 t)$ in the presence of a non-zero constant D_0. For an arbitrary value of C_0, D takes the value between $D_0 - C_0$ and $D_0 + C_0$ as time changes. Specifically, as D varies between $D_0 - C_0 < D < D_0 + C_0$ in time, effectively, the system goes through different attractors from damping to chaotic solutions in time for a sufficiently large C_0. There thus exists a time interval in $2\pi/\omega_1$ over which D is smaller than the critical value for the onset of a finite-amplitude solution, i.e. $|D| < 1$. Recall that, our system is invariant under the change of the sign of D. During this time, $|D|$ is too small to excite a finite-amplitude solution, effectively making B decay; this will be named a Dead-Zone (DZ). For a given D_0 our system begins to enter this DZ when $C_0 > D_0 - 1$ since the minimum value of $D < 1$. As C_0 increases further from $D_0 - 1$, the time span for DZ increases until $D_0 - C_0 = -1$ ($C_0 = D_0 + 1$). For $C_0 > D_0 + 1$ ($D_0 - C_0 < -1$), the system starts exploring the region of the negative value of $D < -1$ where a finite-amplitude solution exists as $|D| > 1$. This suggests that our system stays in the DZ for the longest time span when $C_0 = D_0 + 1$. This has an important consequence a nonlinear response as discussed in detail in Sections 3.3 and 3.4.

The main issues to be addressed are: (i) how linear instability depends on C_0 and ω_1 in the absence of nonlinearity in our system; (ii) how the nonlinear response depends on C_0 and ω_1; (iii) whether the response of the system becomes maximum or minimum for certain values of C_0 and ω_1; (iv) whether there is a relation between C_0 and ω_1 for a given constant D_0 which governs the transition point where the effect of the oscillatory D disappears (like the linear relation found for $D_0 = 0$ in Mohamed and Kim (2014).) To be able to answer these questions, we solve our main equations (3.1) numerically using the RK45 method for a sufficiently small time step (e.g. $dt = 0.001$) to ensure numerical accuracy for a fixed value of $\nu = 0.5$, as done in previous work Jones et al. (1985), Mohamed and Kim (2014).

Section 3.2 contains a linear analysis of our system. Section 3.3 and Section 3.4 provide the results for fixed $D_0 = 2$ and $D_0 = 4$, respectively, by varying the values of C_0 and ω_1. A value of $D_0 = 2$ in Section 3.3 is chosen as a constant parameter which is very close to the second bifurcation at 2.07. In comparison the value of $D_0 = 4$ in Section 3.4 ensures chaos when $C_0 = 0$. Discussion and conclusions are in Section 3.5.

§ 3.2 Linear Results

For a linear analysis, we drop the nonlinear terms proportional to $A^*\Psi$ and AB in Eqs. 3.1. In this case, Ψ is decoupled from A and B and damps at the rate ν. The coupled equations for A and B can be reduced to one equation in terms of $\tilde{B} = Be^{-t}$ as follows:

$$\frac{d^2\tilde{B}}{dt^2} - 2i(D_0 + C_0\cos(\omega_1 t))\tilde{B} = 0. \tag{3.2}$$

For $C_0 = 0$, the linear growth rate γ and natural frequency ω_0 of B can easily be found from Eq. (3.2) as:

$$\gamma = \sqrt{D_0} - 1\,, \omega_0 = \pm\sqrt{D_0}. \tag{3.3}$$

For $C_0 \neq 0$, Eq. (3.2) represents the Mathieu equation with imaginary parameters, which has been studied much less than the case with real parameters (e.g. see Ziener et al. (2012)). Instead of looking for solutions in terms of series, we compute (the largest) linear growth rate numerically for the parameter values of

$D_0 = 2, 4$ and for $C_0 = 2, 20$ as we vary ω_1. The resulting linear growth rates are shown in Fig. 3.1.

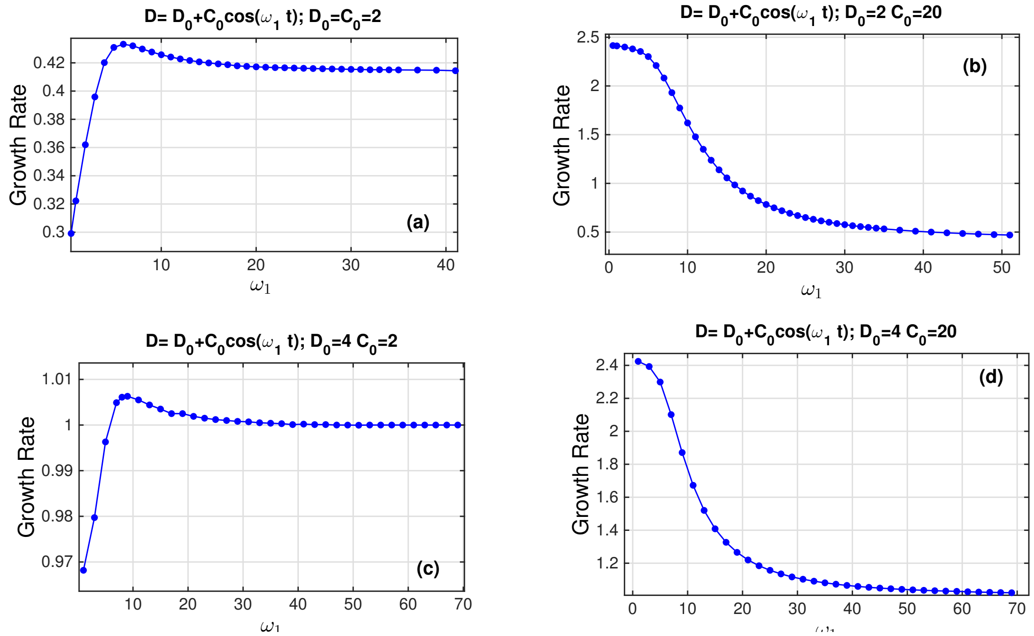

Figure 3.1: Linear growth rates for (a) $D_0 = C_0 = 2$; (b) $D_0 = 2$ and $C_0 = 20$; (c) $D_0 = 4$ and $C_0 = 2$; (d) $D_0 = 4$ and $C_0 = 20$.

Fig. 3.1a shows that for $C_0 = D_0 = 2$, the linear growth increases with ω_1 and takes its maximum value 0.438 at $\omega_1 \approx 6$. It is important to note that $\omega_1 \approx 6$ where the maximum growth rate occurs is about 4 times larger than the natural frequency $\omega_0 = \sqrt{D_0} = \sqrt{2}$ [see Eq. (3.3)]. This should be compared with the parametric resonance in a system of real variables that arise when the frequency of the periodic perturbation is twice the natural frequency [e.g. see Priede et al. (2010) and references therein] and is due to the fact that our variables are complex instead of real. As ω_1 is further increased from $\omega_1 \approx 6$, the linear growth rate slowly decreases and approaches an asymptotic value of $\gamma = \sqrt{2} - 1$, equal to the linear growth rate for $D_0 = 2$ and $C_0 = 0$, see Eq. (3.3). That is, the effect of the periodic perturbation disappears for a sufficiently large $\omega_1 > 23$.

Similar dependence of the linear growth rate on ω_1 is observed for $D_0 = 4$ and $C_0 = 2$ in Fig. 3.1c which shows the maximum growth rate at $\omega_1 \approx 8$. The value of the maximum growth rate in this case is again about four times larger than $\omega_0 = \sqrt{D_0} = \sqrt{4}$. The disappearance of the effect of the periodic control parameter is also observed for a sufficiently large ω_1, the growth rate approaching its asymptotic value of $\gamma = \sqrt{4} - 1 = 1$ [see Eq. (3.1)]. However, when the periodic control parameter is significantly larger than the value of D_0, the growth rate is found to monotonically decrease with increasing ω_1, approaching the value given in Eq. (3.3). This is shown in the cases of $D_0 = 2$ and $C_0 = 20$ in Fig. 3.1b and $D_0 = 4$ and $C_0 = 20$ in Fig. 3.1d.

In Section 3.3 and Section 3.4, we show that the effect of C_0 on the growth rate for finite ω_1 (i.e. the existence of maximum growth rate, or monotonic decrease in growth rate) is different from the nonlinear response while the disappearance of the effect of C_0 for sufficiently large ω_1 is similar in the nonlinear case.

§ 3.3 Non-linear Results for $D_0 = 2$

In section 3.2 exponentially growing solutions are obtained. However, in this section, including the nonlinear terms in the system leads to finite-amplitude solutions after passing through the stage of the initial transient growth. In order to quantify the nonlinear response systematically, we carry out the following tasks:

(I) Solve Eqs. 3.1 for the chosen values of C_0 and ω_1;

(II) Compute the mean value of variables (e.g. $|B|^2$) by taking a time-average after removing the initial transient;
(III) Compute the Fourier series of B by taking the Fourier Transform of the time-series of B, compute the frequency spectrum and determine the dominant (output) frequency of B where the frequency spectrum takes its maximum value;
(IV) Repeat (I)–(III) by varying the values of C_0 and $\omega_1 \in (0, 35)$.
In this section, we consider a fixed value $D_0 = 2$ which has a periodic solution in the absence of the oscillatory control parameter ($C_0 = 0$); Secs. 3.3.1 and 3.3.2 present results for a fixed value of C_0 for different values of ω_1 and for a fixed value of ω_1 and for different values of C_0, respectively.

3.3.1 RESULTS FOR FIXED C_0

To understand the nonlinear response of the system when the oscillatory forcing results in multiple attractors in time, we present the detailed nonlinear results for $C_0 = 2$ and $C_0 = 20$. In the first case, $C_0 = 2$ damping solutions occurring only during the time span when $0 < D < 1$. The second $C_0 = 20$ is the case when our system spends a very short fraction of the time in a DZ where $|D| < 1$.

3.3.1.1 $C_0 = 2$

The case of $\omega_1 = 0$ recovers the result for constant dynamo number $D = 4$ where finite-amplitude solutions are chaotic Jones et al. (1985). For non-zero ω_1, the value of D changes between 0 and 4 in time, spanning from a damping solution for $D < 1$ (i.e. in the DZ) to a chaotic solution for $D > 3.84$. We note that a previous analysis based on the synchronisation and the exit time from a bistable attractor Jones et al. (1985) cannot thus be carried over to our system. Starting from a chaotic attractor that occurs at $D = 4$ with $\omega_1 = 0$, our system changes its stability as the value of ω_1 changes. One example of such a transition is shown for $\omega_1 = 1.4$ in Fig. 3.2 where the attractor loses its chaos and becomes quasi-periodic. In order to study separate oscillations due to the driving frequency ω_1, we superimpose the Poincaré sections as red circles in Fig. 3.2. The Poincaré sections are obtained by taking the data at discrete times that are multiples of $\omega_1/2\pi$. As ω_1 further increases, these quasi-periodic solutions eventually become oscillatory.

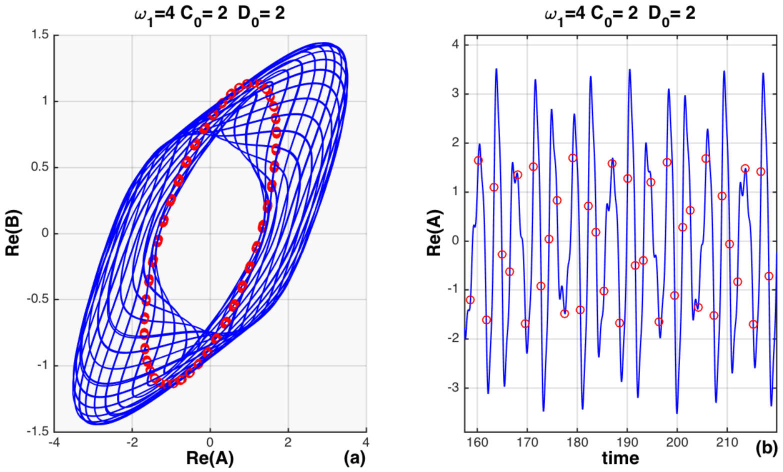

Figure 3.2: (a) Quasi-periodic solution of Eq. (3.1) where the Poincaré-sections are shown in red circles; (b) The time history of Re(A) for $\omega_1 = 4$.

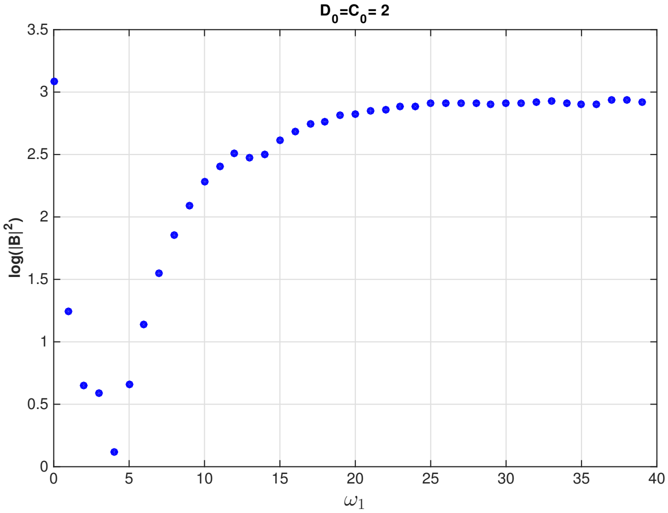

Figure 3.3: $|B|^2$ as a function of ω_1

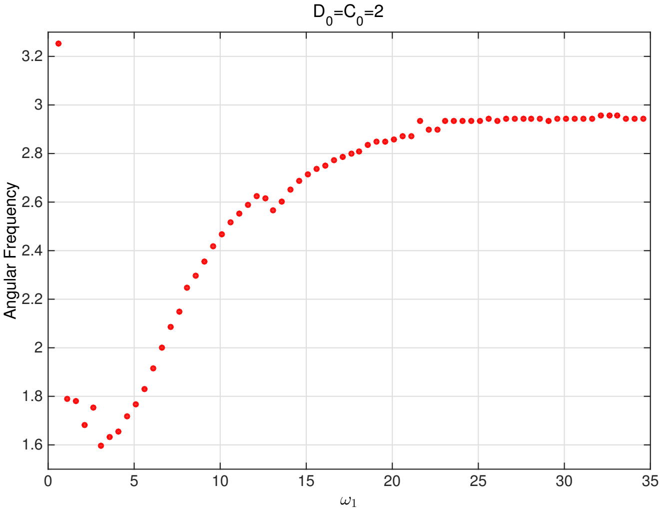

Figure 3.4: The dominant output frequencies of B for $D_0 = C_0 = 2$.

As we are more interested in the overall effect of ω_1 rather than detailed bifurcations, we utilise the mean amplitude and frequency power spectrum of B against ω_1 as quantitative measures and show them in Figs. 3.3, 3.4 and 3.5, respectively. Fig. 3.3 shows that $|B|$ decreases as ω_1 increases from zero, takes its minimum value around $\omega_1 \approx 4$, and then increases with further increase in ω_1

for $\omega_1 > 4$. This dependence of $|B|^2$ on ω_1 is in sharp contrast to the behaviour of the linear growth rate γ with respect to ω_1, where the linear growth rate in Fig. 3.9a takes its maximum value around $\omega_1 \approx 6$. This result illustrates that the nonlinear response is fundamentally different from the linear response. For sufficiently large $\omega_1 > 23$, the amplitude becomes almost constant with the value of 3 as the oscillatory parameter no longer has any effect on the system due to large ω_1, which is similar to the behaviour in the linear version noted in Section 3.2.

Fig. 3.4 illustrates how the dominant frequency of B changes with ω_1 where the dominant frequency denotes the output frequency of B at which the frequency spectrum is a maximum. The frequency spectrum can however have multiple peaks or a broad spectrum (in the case of chaos), so the dominant frequency given in Fig. 3.4 is a crude representation of the temporal behaviour of the system. We thus show the entire frequency spectrum in colour for different values of ω_1 in Fig. 3.5, where colour represents the intensity of the frequency. Specifically, colours are assigned according to the colour coding as shown in the bar next to the figure where frequency of the maximum intensity to low intensity is represented by yellow to dark colours, respectively. Note that the chaotic solution at $\omega_1 = 0$ with a broad frequency spectrum leads to the scattered bright points along y-axis in Fig. 3.5. In Figs. 3.4 and 3.5, the transition from chaos to an oscillatory solution can be seen for $\omega_1 > 23$ where the only dominant frequency takes its constant value ≈ 3. Interestingly, this value of the angular frequency is very close to the natural output frequency $\omega = \omega_0$ of the system (3.1) for $D_0 = 2$ in the nonlinear case. This suggests that the effect of oscillatory D disappears for $\omega_1 > 23$ in the case of $C_0 = 2$.

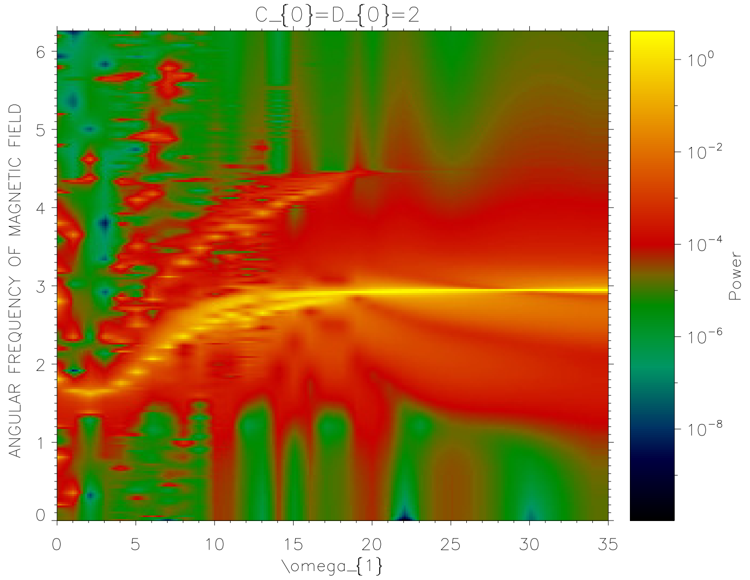

Figure 3.5: The frequency spectrum of B against ω_1 for $D_0 = C_0 = 2$.

It is interesting to observe that Figs. 3.3(a), 3.4, and 3.5 exhibit a very similar trend in that the impact of the periodic control parameter on the system gradually fades away as ω_1 increases until it completely disappears for $\omega_1 \approx 23$. Beyond this point, the solution recovers the result for the case of a constant control parameter $D = 2$, the dominant frequency and amplitude taking the asymptotic values of 2.945 and 3, respectively. This result is reminiscent of what was found in the linear case in Section 3.2 as well as in our previous work in the case of a purely oscillatory control parameter $D = C_0 \cos(\omega_1 t)$, where the effect of an oscillatory control parameter disappears for a sufficiently large ω_1. Furthermore, Figs. 3.3 -3.5 show that the system's response is minimum around $\omega_1 \approx 3.8$, as manifested by the minimum value of output frequency and $|B|^2$. This value of $\omega_1 \approx 3.8$ differ from the natural frequency of 2.945 in the nonlinear case of the constant $D = D_0 = 2$. This behaviour is probably due to the complexity associated with the finite-amplitude perturbation C_0, such as different attractors that our system explore as time changes.

3.3.1.2 $C_0 = 20$

The previous subsection 3.3.1 considered the case where constant and the oscillatory control parameters are comparable as $C_0 = 2 = D_0$. What will happen in the case of a large driving amplitude C_0 when the effect of the oscillatory control parameter dominates over that of constant control parameter? To answer this question, we now consider a much larger value of the $C_0 = 20$. As D varies in $-18 < D < 22$, the system's solutions change between damping and chaotic solutions twice for one period of $2\pi/\omega_1$, spending a little time in DZ, as noted previously.

Following the same steps as in Section 3.1.1, we plot the amplitude and frequency spectrum in Figs. 3.6- 3.8 for $C_0 = 20$. We observe that at $\omega_1 = 0$, finite-amplitude solution is chaotic as expected for $D = 20$. As ω_1 increases from zero, the attractor becomes quasi-periodic; for sufficiently large ω_1, it changes to a periodic oscillation, recovering the result for a constant $D = D_0 = 2$. Specifically, compared with the case of $C_0 = 2$, the minimum in Figs. 3.6 and 3.7 occurs at $\omega_1 = 7.8$ for $C_0 = 20$, further from the natural frequency $\omega_0 = 2.958$ for constant $D = D_0 = 2$ as a result of a significantly larger oscillatory perturbation. Interestingly, this minimum response at $\omega_1 = 7.8$ again differs from the linear response where the linear growth rate monotonically decreases with ω_1 (see Fig. 3.1c and the corresponding discussion in Section 3.2). The wide yellow band is shown for $\omega_1 < 20$ in Fig. 3.8, and again represents a continuous frequency spectrum associated with the chaotic solutions. In this figure, a few distinct, discrete peaks in bright yellow are observed for $20 < \omega_1 < 140$ in the background of an almost continuous spectrum shown in red. Upon a further increase in ω_1, only one frequency (shown in bright yellow) survives and remains almost constant, approaching the asymptotic frequency ≈ 3. The latter corresponds to the frequency for the periodic attractor for constant $D = D_0 = 2$, reflecting the disappearance of the effect of oscillatory parameter for large ω_1. Similar behaviour is also seen for the amplitude squared $|B|^2$ shown in Fig. 3.6, where $|B|^2$ becomes almost constant for $\omega_1 > 140$. The disappearance of the effect of the oscillatory control parameter for large ω_1 is again similar to the linear behaviour.

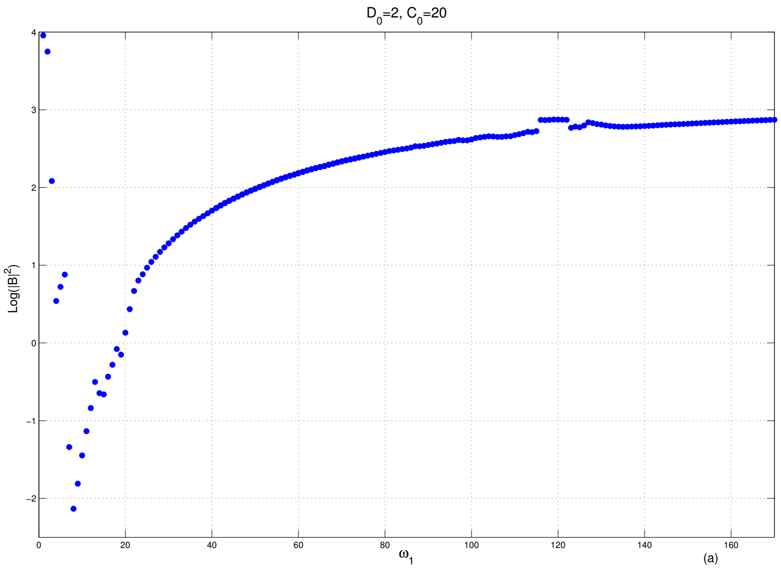

Figure 3.6: $|B|^2$ against ω_1 for $D_0 = 2$ and $C_0 = 20$.

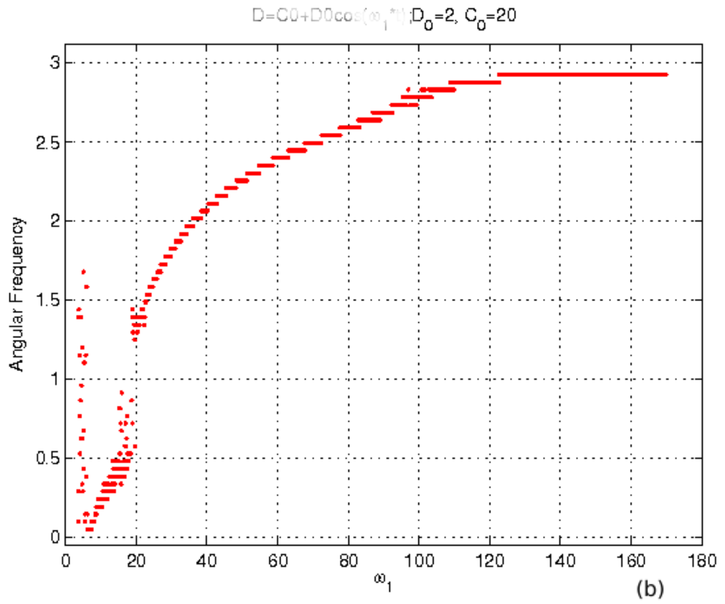

Figure 3.7: The dominant frequencies of B against ω_1 for $D_0 = 2$ and $C_0 = 20$.

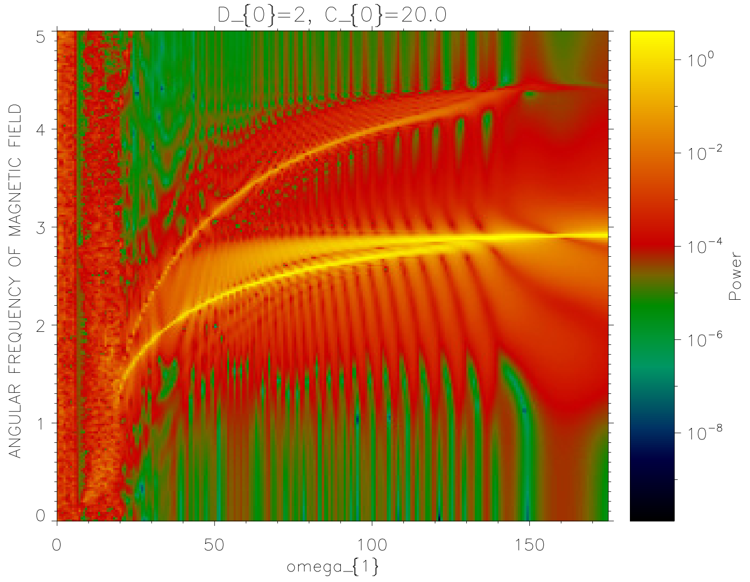

Figure 3.8: The frequency spectrum of B against ω_1 for $D_0 = 2$ and $C_0 = 20$.

In summary, in Section 3.3.1 we analysed the system's response to varying ω_1 when C_0 was fixed and showed that the system exhibits non-monotonic behaviour with the minimum response around $\omega_1 \approx 3.8$ for $C_0 = 2$ and $\omega_1 \approx 7.8$ for $C_0 = 20$

where the minimum values of the amplitude and frequency of B occur. $\omega_1 \approx 3.8$ in the case of $C_0 = 2$ is quite close to the natural frequency $\omega_0 = 2.958$ for constant $D_0 = 2$ while $\omega \approx 7.8$ in the case of $C_0 = 20$ is further from the natural frequency ω_0 due to the large perturbation. The questions that arise are; how the system changes its response for different amplitudes C_0 when the driving frequency was fixed; also how the minimum response is manifested as C_0 is varied when ω_1 is fixed. These issues will be addressed in the following Section 3.3.2.

3.3.2 RESULTS FOR FIXED ω_1

We now investigate the system's response to varying C_0 by choosing a fixed value of $\omega_1 = 3.0$. This particular value of the driving frequency $\omega_1 = 3.0$ is chosen since it is close to the natural frequency of $\omega_0 = 2.958$ when $D_0 = 2$. For fixed $\omega_1 = 3.0$, we observe different types of solutions as C_0 is varied. Specifically, with C_0 increasing from zero, the solution starts with a quasi-periodic oscillation. One example is shown in Fig. 3.9 for $C_0 = 2$ where the Poincaré sections are shown as red circles. Further increases in the parameter C_0 lead to a more complicated attractor towards chaos for $C_0 > 3.4$. Fig. 3.10 shows the dependence of the amplitude of B on C_0 systematically. As can be seen, $|B|^2$ decreases with C_0 for $0 < C_0 < 2$, increases slowly for $2 < C_0 < 16$, and then increases very rapidly for $C_0 > 16$. The minimum $|B|$ is observed around $2.5 < C_0 < 3.5$. The corresponding frequency spectrum of B is shown in Fig. 3.11. We recall that the bright broadband spectrum shown in the vertical direction in this figure indicates a chaotic state. The width of the band decreases initially up to $C_0 \approx 2.3$ and then gradually becomes wider with the further increase in C_0. This broadening band is interestingly associated with a rapid increase in $|B|^2$ with C_0 shown in

Fig. 3.10.

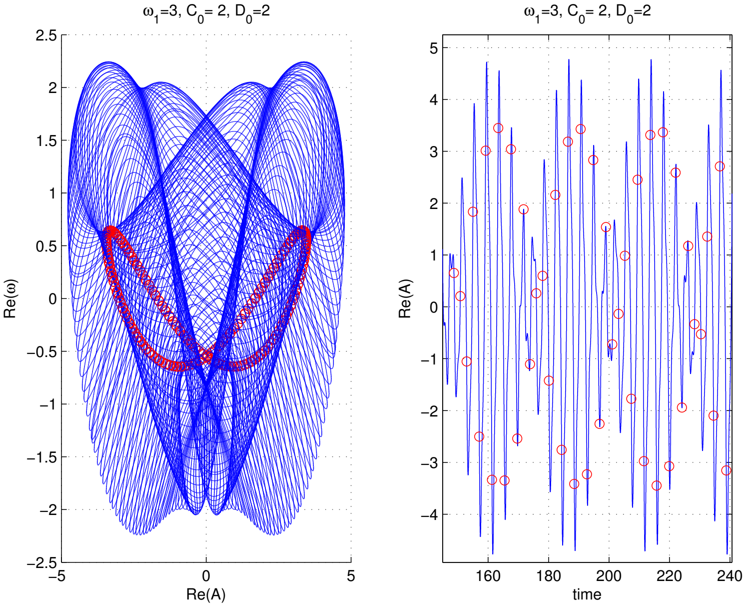

Figure 3.9: Quasi-periodic solution of the system with the Poincaré sections shown in red circles for $C_0 = 2$.

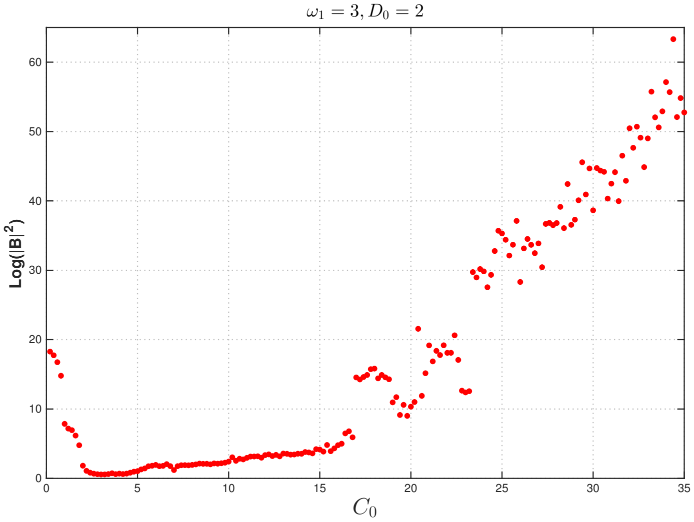

Figure 3.10: $|B|^2$ as a function of C_0 for $\omega_1 = 3$

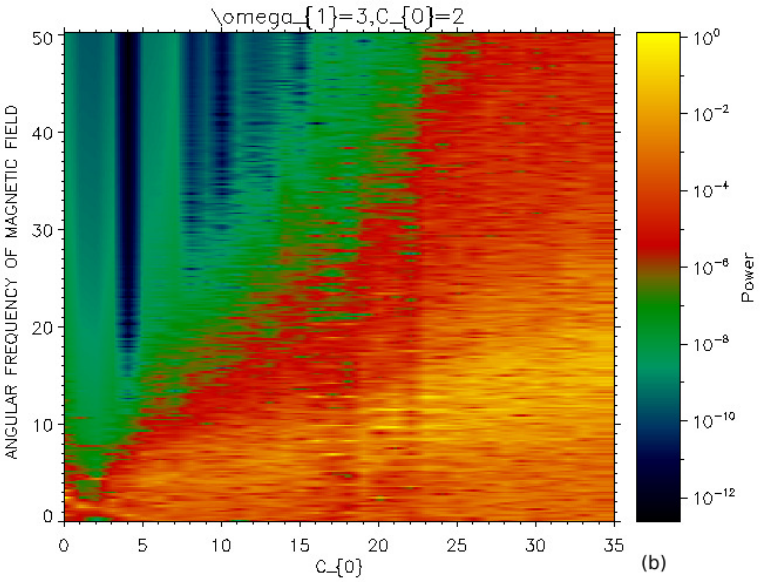

Figure 3.11: The frequency power spectrum of B against C_0 for $\omega_1 = 3$

3.3.3 Summary of results for $D_0 = 2$

The results in Sections 3.1 and 3.2 show how the system responds to different values of ω_1 for fixed C_0 and vice versa. For a comprehensive understanding of the system, it is worthwhile presenting results for different values of C_0 and ω_1 at the same time. To this end, after performing steps (I)-(III) described in Section 3.2, we carry out the following steps (IV')-(VI'):

(IV') Plot results from (II) as a function of C_0 and ω_1 on a 3D plot in Fig. 3.12;

(V') Plot results from (III) as a function of C_0 and ω_1 on a 3D plot in Fig. 3.13;

(VI') Repeat (I)–(III) and (IV')-(V') by varying the values of C_0 and $\omega_1 \in (0, 35)$.

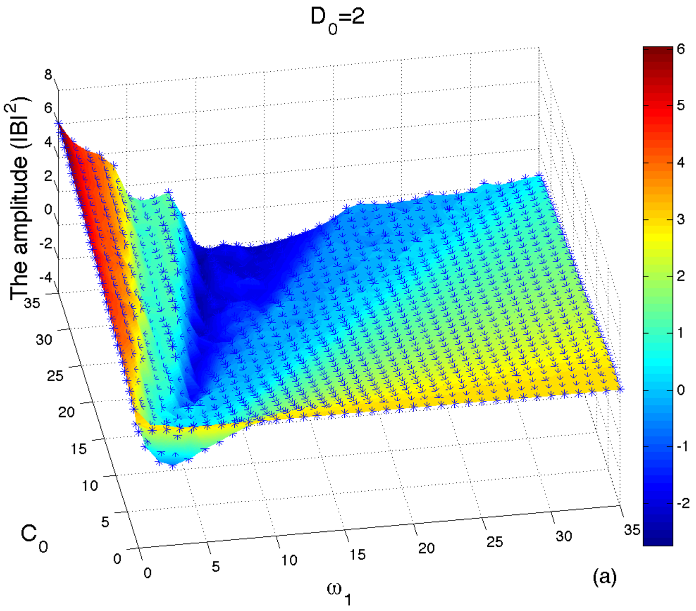

Figure 3.12: 3D plot of B amplitude

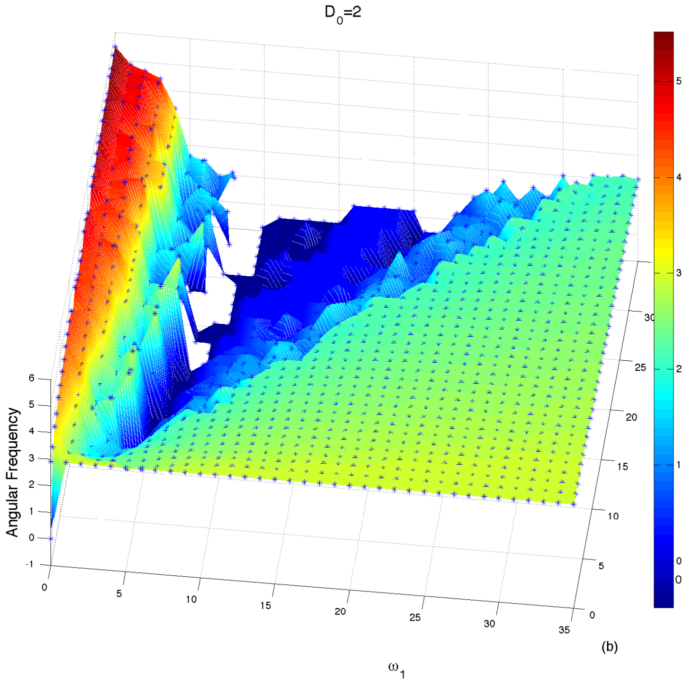

Figure 3.13: 3D plot of the dominant output frequency of B for fixed $D_0 = 2$ against C_0 and ω_1

Fig. 3.12 shows $|B|^2$ (in colour) as a function of ω_1 and C_0 where red (blue) indicate high (low) amplitude. Similarly, Fig. 3.13 shows the dominant output frequency for different values of ω_1 and C_0 where the intensity of the dominant frequency is portrayed in colour. Hot and cool colours indicate strong and weak intensity. Note that, in both Figs. 3.12 and 3.13, the Z-axis is plotted in *Log* scale. Non-monotonic behaviour of the system that was discussed in Sections 3.1-3.2 is clearly seen as valleys in dark colours for certain values of ω_1 and C_0 in both Figs. 3.12 and 3.13 where the amplitude and dominant output frequency of B take their local minimum values, respectively. Alternatively, for any fixed value of C_0, there is a particular value of ω_1 which gives a minimum amplitude (frequency) and vice versa. These valleys represent the minimum response of our nonlinear system for a certain combination of C_0 and ω_1. It is important to highlight that in contrast to the linear results for the largest growth rate at certain parameter values, the non-monotonic response of our nonlinear system, implied by these valleys, represents the 'smallest' response due to nonlinear effects.

The coordinates of the valley in Fig. 3.12 are shown in Fig. 3.14a, while the valley coordinates in Fig. 3.13 are shown in Fig. 3.14c. Fig. 3.14b plots the value of $|B|^2$ against C_0 at the valleys in Fig. 3.14a.

Similarly, Fig. 3.14d plots the value of the output frequency of B against C_0 at the valleys in Fig. 3.14c. Consequently, Fig. 3.14a establishes the relationship between C_0 and ω_1 for the minimum response. It can be seen that ω_1 decreases with increasing C_0 for $C_0 \leq 3.4$, and then starts to increase in direct proportion to C_0 except for a short interval $7 \leq C_0 \leq 8$. Fig. 3.14b shows that $|B|^2$ tends to decrease as C_0 increases although there is a slight increase in $|B|^2$ for $C_0 \in (4, 7)$. Moreover $|B|^2$ remains almost constant for $C_0 \geq 10$. Fig. 3.14d illustrates that for small C_0, the output frequency at the valley is inversely proportional to C_0

while it becomes almost constant for sufficiently large C_0. Interestingly, similar trends in C_0 and ω_1 can be seen in Fig. 3.14a and 3.14c while multiple values of ω_1 leading to minimum output frequency can be observed certain C_0 in Fig. 3.14b.

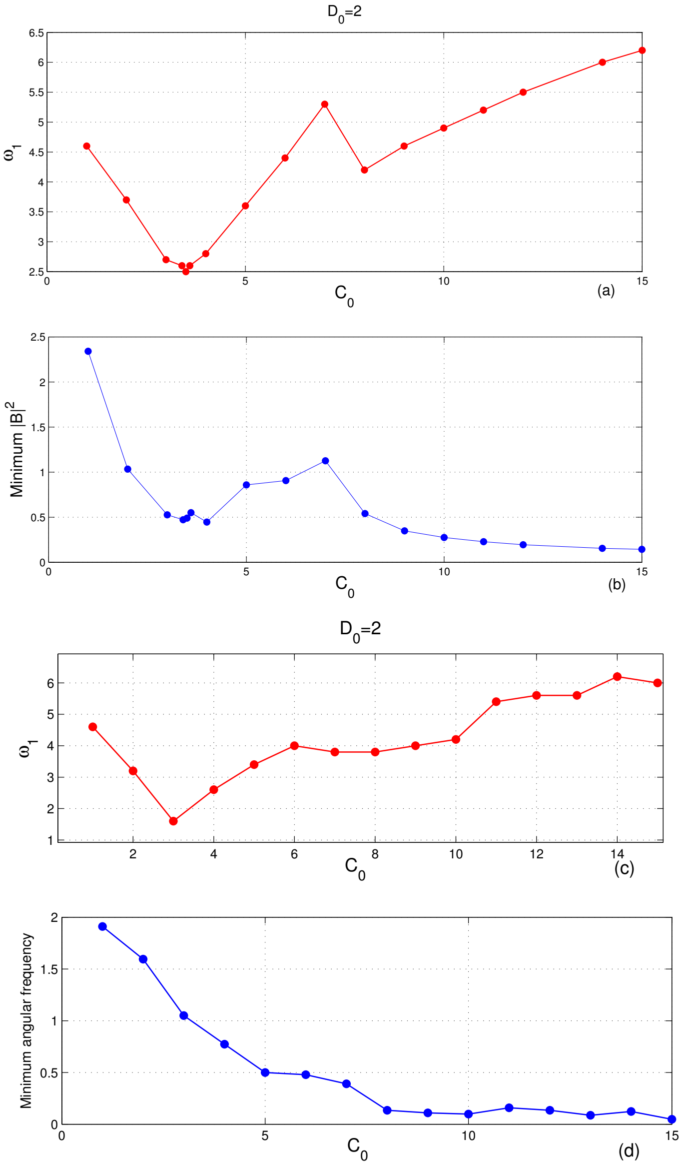

Figure 3.14: (a) Coordinates of the valley in Fig. 3.12; (b) The value of $|B|^2$ against C_0 at the valley in Fig. 3.13 (c) Coordinates of the valley in Fig. 3.13; (d) The value of the output frequency against C_0 at the valley in Fig. 3.13.

The existence of the minimum response for certain values of C_0 and ω_1 in Fig. 3.14a and Figs. 3.14c-d suggests that there are two distinct regimes depending on the value of C_0. The transition between these two regimes occurs around $C_0 \approx 3.4$. To understand this, we recall that as D varies between $D_0 - C_0 < D < D_0 + C_0$ in time, there exists a time interval in $2\pi/\omega_1$ over which D is below the critical value for the onset of a finite-amplitude solution, i.e. $|D| < 1$ (i.e. the DZ). As noted in Section 3.1, our system stays in the DZ for the longest time span for $C_0 = D_0 + 1$, effectively leading to the minimum value of $|B|^2$. Specifically, for $D_0 = 2$, the minimum response is thus expected for $C_0 \approx 3$, therefore explaining $C_0 \approx 3.4$ observed in Fig. 3.14a and Figs. 3.14c-d. For sufficiently large C_0, D effectively varies twice between 0 and C_0 as t changes by $2\pi/\omega_1$, staying only briefly in the DZ. Interestingly, this explains the transition observed around $C_0 > 6$ in Figs 3.14a and 3.14c, where the effect of C_0 becomes smaller. From Fig. 3.14c, we found an approximate quadratic dependence of ω_1 on C_0 as $\omega_1 \approx -0.0075{C_0}^2 + 0.4576C_0 + 1.0365$ for $C_0 > 8$.

§ 3.4 Nonlinear Results for $D_0 = 4$

We consider the case where the unperturbed control parameter is close to the bifurcation point to chaos ($D = D_0 = 3.84$) by choosing $D_0 = 4$ and investigate how the oscillatory perturbation affects the nonlinear response for different values of C_0 and ω_1. As we follow a similar analysis to that performed in the previous section, we provide a rather brief discussion.

3.4.1 RESULTS FOR FIXED $C_0 = 2$ AND $C_0 = 20$

For fixed $D_0 = 4$, we present results for $C_0 = 2$ and $C_0 = 20$ by varying ω_1.

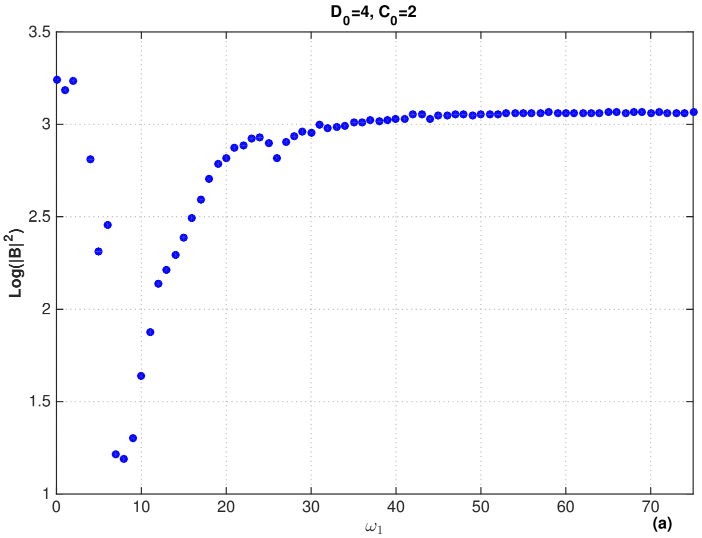

Figure 3.15: The amplitude of B as a function of ω_1 for $C_0 = 2$

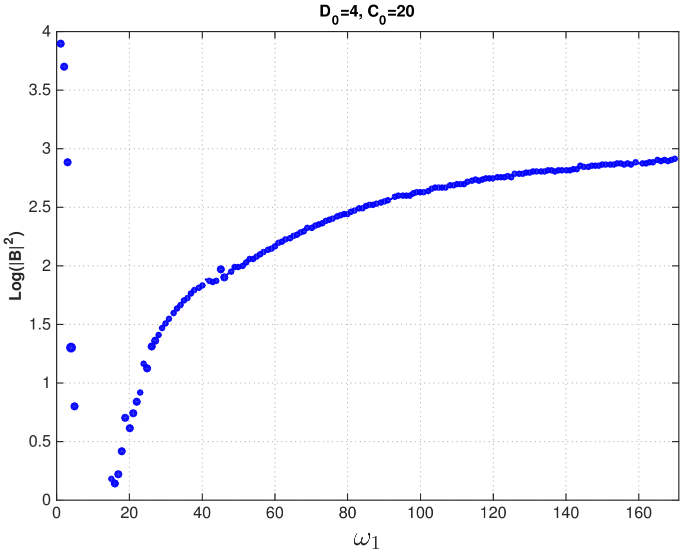

Figure 3.16: The amplitude of B as a function of ω_1 for $C_0 = 20$.

Figs. 3.15 and 3.16 show the amplitude $|B|^2$ against ω_1 for $C_0 = 2$ and $C_0 = 20$, respectively while Figs. 3.17 and 3.18 plot the corresponding angular frequency spectrum. From these figures, the minimum response is found around $\omega_1 = 7.8$ in both cases of $C_0 = 2$ and $C_0 = 20$. This result contrasts to the case $C_0 = 2$

when the minimum response occurs at $\omega_1 \approx 3.8$ (which was much closer to the natural frequency $\omega_0 = 3$). Essentially this implies that, the system's response to oscillatory control parameter becomes more complex for larger D_0 (due to the chaotic state) as well as for larger C_0. Furthermore, the nonlinear response to varying ω_1 in both cases also differs from the linear response discussed in Section 3.2 [see Fig. 3.1b and Fig. 3.1d].

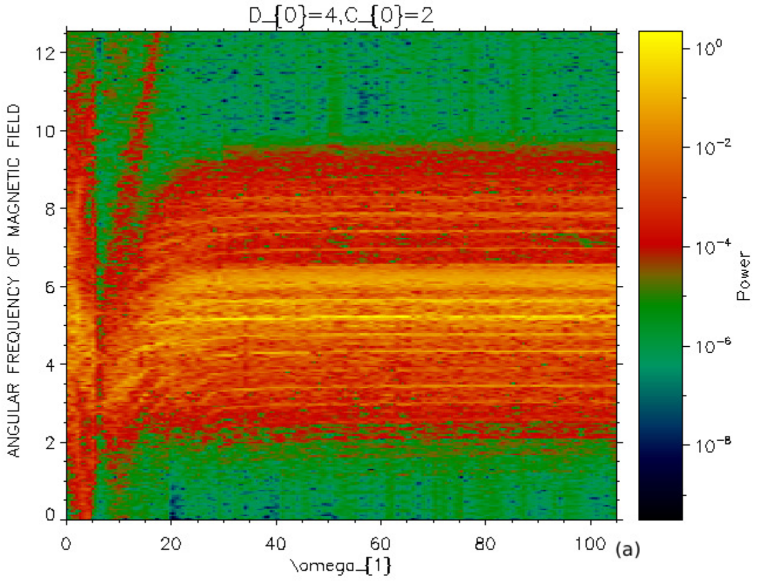

Figure 3.17: Frequency spectrum of B against ω_1 for $C_0 = 2$

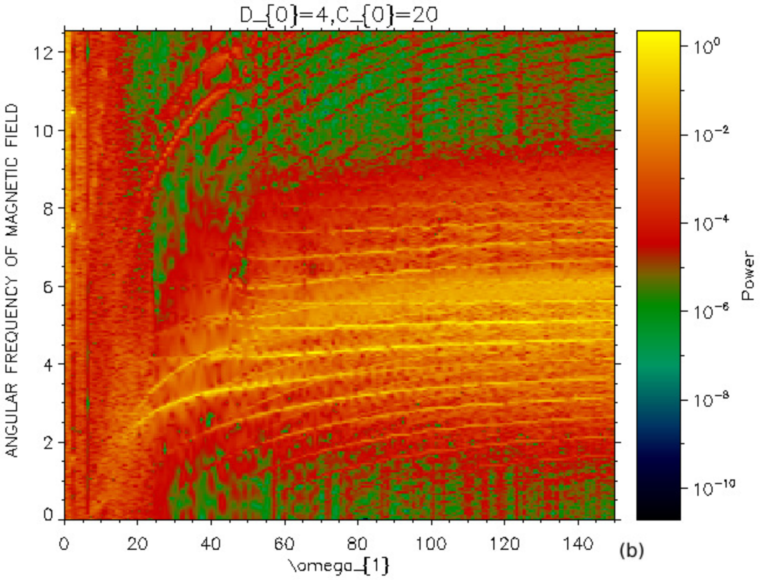

Figure 3.18: Frequency spectrum of B against ω_1 for $C_0 = 20$.

3.4.2 Summary of results for $D_0 = 4$

To understand the system's overall behaviour for $D_0 = 4$ we present the 3D plots of the mean value of $|B|^2$ and the dominant output frequency in Figs. 3.19 and 3.20, respectively, by performing similar steps required for Figs. 3.12 and 3.13.

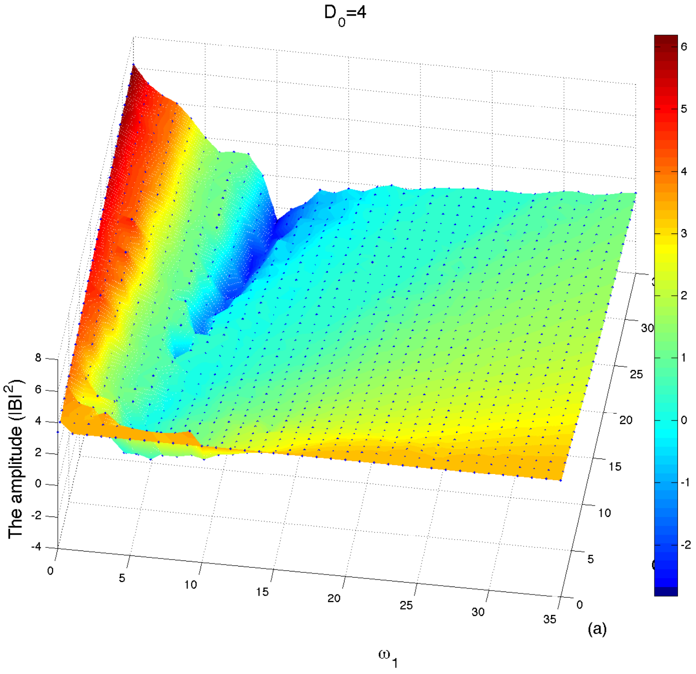

Figure 3.19: $|B|^2$; the colour is assigned to the intensity according to the scale shown in the colour bar on the right.

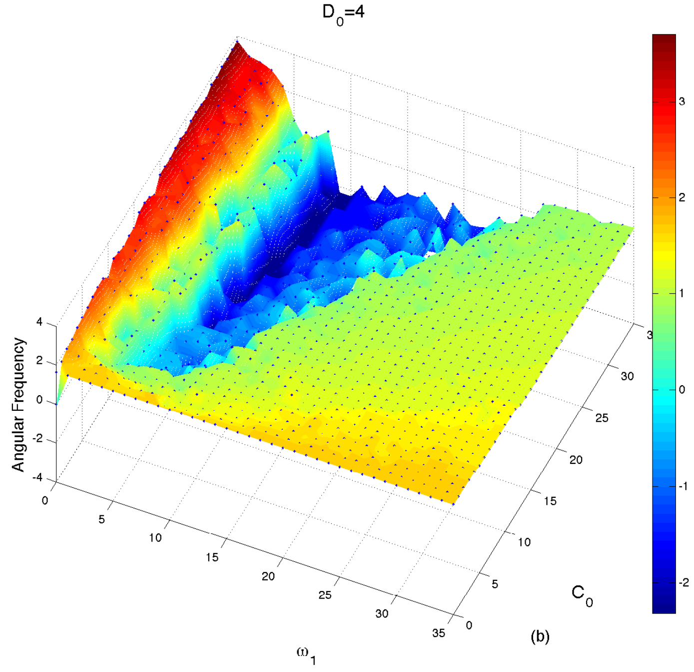

Figure 3.20: Dominant output frequency of B against ω_1 and C_0.

Specifically, Fig. 3.19 and Fig. 3.20 illustrate $|B|^2$ and the dominant output frequency respectively, as a function of C_0 and ω_1.

It is interesting to see the valleys in the minimum values of $|B|^2$ as well as in the dominant frequency of B in Figs. 3.19 and 3.20, respectively, similar to those observed in Figs. 3.12 and 3.13. These valleys again result from the minimum complexity (or maximum order) of our system for a certain combination of C_0 and ω_1; these are indicative of a non-monotonic response of the system upon the application of the perturbation. The coordinates of the valleys in Figs. 3.19 and 3.20 are shown in Fig. 3.21a and Fig. 3.21c [similar to Figs. 3.14a, 3.14c]. Fig. 3.21b shows the value of the minimum amplitude of $|B|^2$ at the valleys shown in Figs. 3.21a. It is clear that $|B|^2$ tends to decrease with C_0 until it becomes almost constant for $C_0 \geq 10$. Similarly, Fig. 3.21d plots the value of the minimum output frequency of B against C_0 at the valleys shown in Fig. 3.21b. Fig. 3.21d reveals that for $C_0 \leq 5$, ω_1 decreases with the increase of C_0 while for $C_0 \geq 5$, ω_1 increases in direct proportion to C_0. We note that Fig. 3.21a and Fig. 3.21c exhibit rather similar behaviour between C_0 and ω_1 although the latter shows multiple values of ω_1 for certain values of C_0. Finally, as in the case of $D_0 = 2$, the change in the relationship between ω_1 and C_0 from being inversely proportional suggests that there are two different nonlinear regimes depending on the value of C_0.

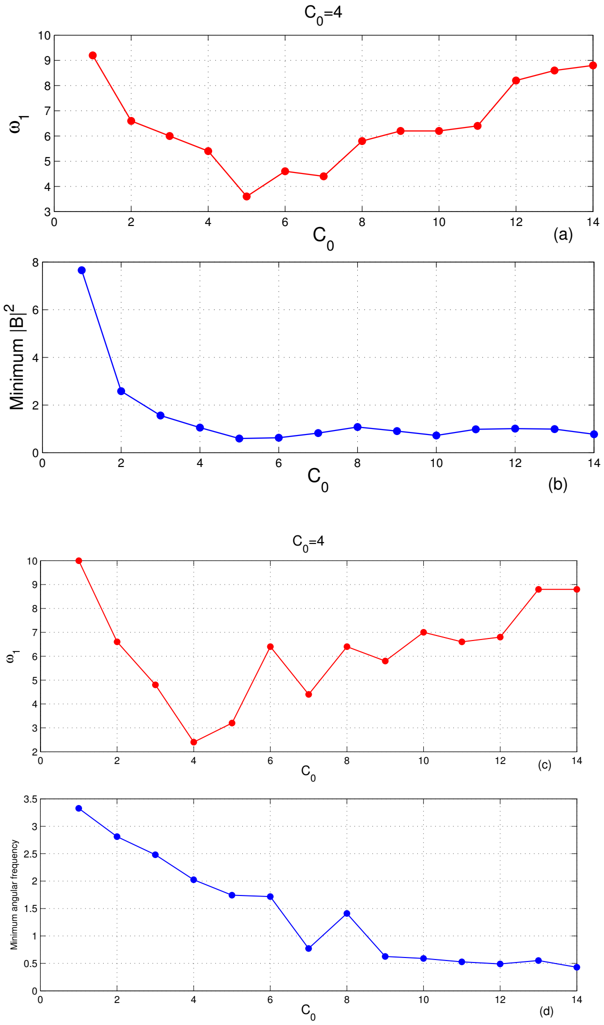

Figure 3.21: (a) Coordinates of the valley in Fig. 3.19; (b) The value of $|B|^2$ against C_0 at the valley in Fig. 3.19); (c) Coordinates of the valley in Fig. 3.20; (d) The value of the output frequency against C_0 at the valley in Fig. 3.20.

§ 3.5 Discussion and Conclusions

We have examined the combined effect of the constant and oscillatory control parameter on the complex-valued Lorenz system by setting $D = D_0 + C_0 \cos(\omega_1 t)$. Our principal findings are summarised as follows:

(i) The linear and nonlinear responses are different for finite frequency ω_1 but are similar for sufficiently large ω_1;

(ii) the maximum linear growth rate occurs due to the parametric instability at $\omega_1 = 4\omega_0$ as long as C_0 is not significantly larger than D_0;

(iii) the minimum nonlinear response occurs at $C_0 \approx D_0 + 1$ when the system stays in the DZ for the longest time;

(iv) the minimum nonlinear response occurs for ω_1 rather close to the natural frequency for small C_0 and D_0;

(v) the effect of the oscillatory control parameter disappears both linearly and nonlinearly for sufficiently large ω_1, with a linear relation between ω_1 and C_0, similar to the case of a purely oscillatory control parameter Mohamed and Kim (2014).

Finally, in order to strengthen our conclusions mentioned above, we also investigated the cases of other values of $D_0 = 3, 3.5, 5, 6, 7$ in addition to $D_0 = 2, 4$ and summarise the relations between C_0 and ω_1 in Figs. 3.22 and 3.23. Specifically, Fig. 3.22 shows $\omega_1/15$ against C_0 where the effect of the oscillatory C_0 disappears. From these results we identify the following relationship between C_0 and ω_1: for $D_0 = 2$, $\omega_1 = 7.3929 C_0 - 0.57$; for $D_0 = 3$, $\omega_1 = 9.2679 C_0 - 8.2857$; for $D_0 = 3.5$, $\omega_1 = 14.393 C_0 - 12$.

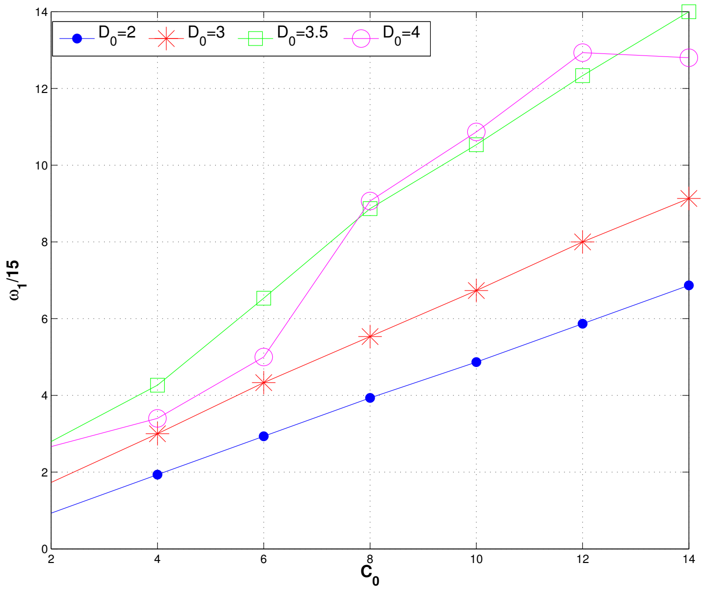

Figure 3.22: $\omega_1/15$ against C_0 where the effect of the oscillatory C_0 disappears for different values of D_0.

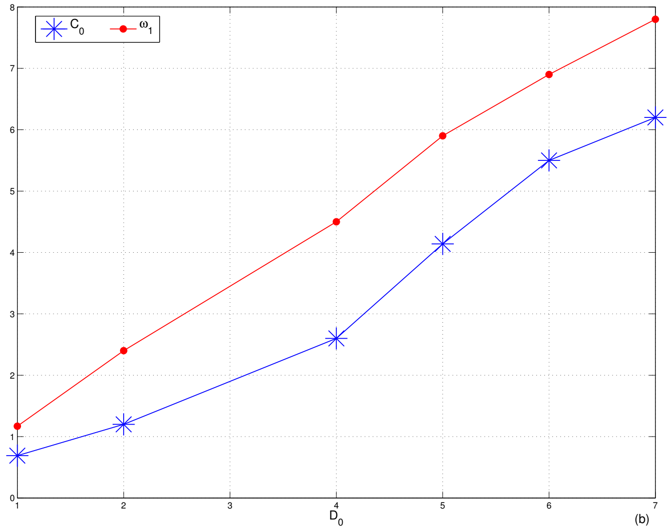

Figure 3.23: The values of C_0 (in red circles) and ω_1 (in blue stars) against D_0 where $|B|^2$ becomes minimum.

Fig. 3.23 shows the values of C_0 (in red circles) and ω_1 (in blue stars) on the y-axis against D_0 where $|B|^2$ becomes minimum. It is interesting to see that in all cases, the minimum response is obtained roughly when $C_0 = D+1$ as reported previously. This result suggests an interesting possibility of controlling dynamical systems (e.g. chaos) by the addition of an oscillatory control parameter. The extension of our work to other systems and the implications will be elaborated in future publications.

Chapter 4

Internal and External Forcing Effects

Abstract

In this chapter, we study the effect of applying internal $(C_0 \cos(\omega_1 t))$ and external $(F_0 \cos(\omega t))$ oscillatory control parameters on the complex Lorenz system. We began with the case when the dynamo number and the additive force are constants. We determined that the main impact of the external force's amplitude F_0 is that it drives the system component B from finite-amplitude solutions into damping behaviour. In opposition, the additive force drives A into periodic oscillation solutions with an amplitude that approximates the driving force F_0. Also, we test the effects of changing the driving frequencies ω_1 and ω for fixed $C_0 = 1$ for some values of F_0. In this case, the system exhibits resonance when $\omega_1 = \omega$.

§ 4.1 Introduction

In Chapter 2, we studied the response of the Lorenz system (1.18) using the parameter $D = C_0 \cos(\omega_1 t)$. In this chapter, we extend this study by adding the term $F_0 \cos(\omega_1 t)$ into the first equation of the system. This scheme of controlling the Lorenz'83 system is implemented by driving the system with internal and external time-dependent forces at the same time.

Examining the dynamical reaction to an external periodic signal is an approach that has been found in some early studies, when undamped oscillators are being observed Dykman and Krivoglaz (1984), Lu and Lu (2003). Our goal is to apply some of the best ideas in this system while maintaining as simple a form as possible.

In this chapter, the Lorenz system is used to simulate the dynamic interactions between the magnetic field's components and differential speed of rotation in the sunspots as shown in Chapter 2. The extended system consisting of the 6th-order differential equations can be rewritten as following:

$$\begin{aligned} \dot{A}(t) &= 2DB(t) - A(t) + F, \\ \dot{B}(t) &= iA(t) - 0.5iA^*\Psi(t) - B(t), \\ \dot{\Psi}(t) &= -iA(t)B(t) - \nu\Psi(t), \end{aligned} \tag{4.1}$$

where the control parameter of the system is defined as $D = C_0 \cos(\omega_1 t)$, and F represents the external forcing which is chosen as $F = F_0 \cos(\omega t)$, and ω_1 and ω are the driving frequencies. These parameters are used to control the behaviour of the Lorenz system (4.1).

The dynamics of the Lorenz system (4.1) are very rich; with the changes we made on the system it is capable of producing different kinds of behaviour, including chaos for different values of driving parameters.

Also the numerical results suggest that negative $-F_0$ and positive $+F_0$ have the same effect on the system for a long time simulation. Thus, it is sufficient to study the system only for positive F_0.

The system is symmetric under the transformation $(A,\ B,\ \Psi,\ D,\ F) \to (A^*,\ -B^*,\ \Psi^*,\ -D,\ -F)$.

The main questions in this chapter are: (i) whether there is a relationship between C_0 and F_0 in the absence of the driving frequencies ω and ω_1, like the linear relationship between C_0 and ω_1 which we found for $D = C_0 \cos(\omega_1 t)$ when $F_0 = 0$ in Chapter 2/ Mohamed and Kim (2014); (ii) whether the system's amplitude becomes maximum or minimum for certain values of C_0 when F_0 is fixed.

To answer these questions, we need to solve the system (4.1) numerically with fixing some parameters while varying the others.

§ 4.2 Numerical Results

We examine the change in the mechanism of the system (4.1) regarding changing different parameters; first, for varying C_0 and F_0 with fixing $\omega_1 = \omega = 0$.

§ 4.3 Results for Varying C_0 and F_0 for $\omega_1 = \omega = 0$

In this section, we consider the parameters as $D = C_0$ and $F = F_0$ where C_0 and F_0 are constants.

In order to understand the system's reaction in respect to the constant D and F, we perform the following four tasks:

(I) For the chosen values of C_0 and F_0, we solve the set of equations (4.1) numerically.

(II) We compute the mean value of B by taking time-average, after eliminating the initial transient.

(III) We use Fourier Series of B from step (I) (i.e. FFT of time-series of B) to compute frequency spectra and determine the dominant (output) frequency of the variable B which represents the frequency when the spectrum takes its maximum value.

(IV) We repeat the steps (I)–(III) by varying the values of C_0 and F_0 in the period $(0, 30)$ and plotted the results for the amplitude/frequency as a function of C_0 and F_0.

Finally, we obtained a 3-dimensional plot that gives the amplitude $|B|^2$/ frequency (in colour) as a function of F_0 and C_0 as shown in Fig. 4.1 / Fig. 4.2, where the colour change from blue to red indicates the amplitude/frequency from lower to higher, respectively.

4.3.1 Case I: (Amplitude of B)

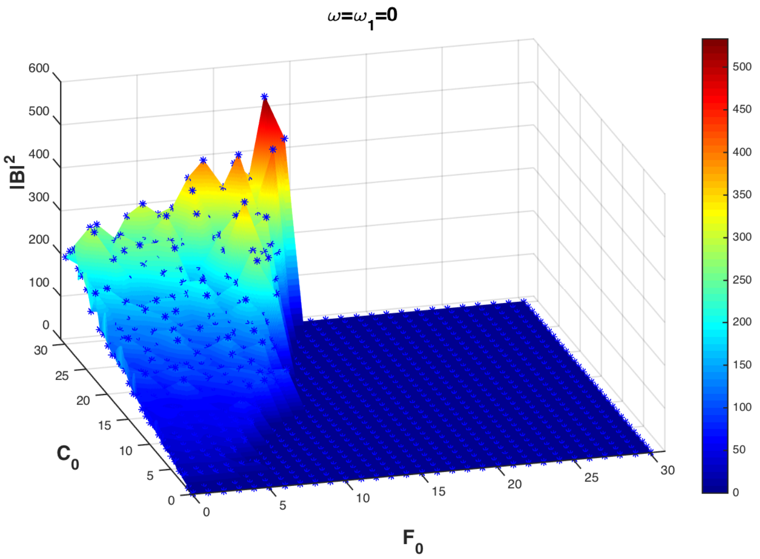

Figure 4.1: 3D plot of the amplitude B as a function of C_0 and F_0

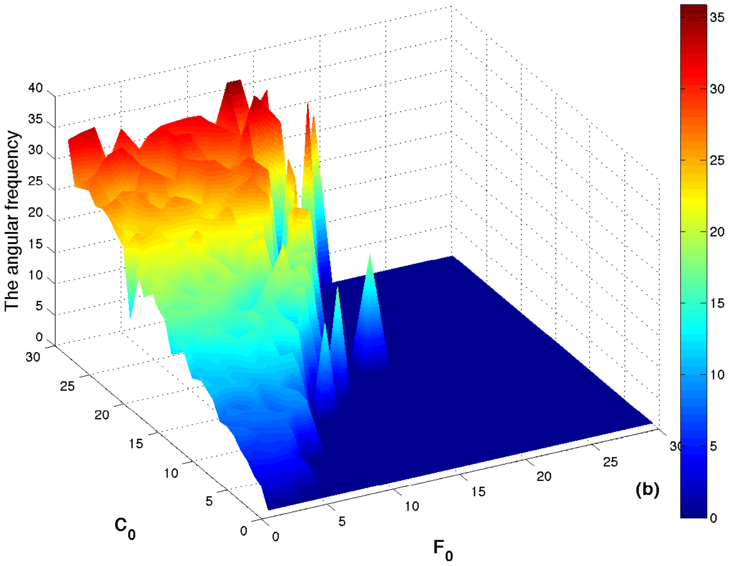

Figure 4.2: 3D plot of the dominant angular frequency of B as a function of C_0 and F_0.

Fig. 4.1 shows the amplitude squad of B ($|B|^2$) as a function of F_0 and C_0 within the range of $(0, 30)$. The corresponding dominant angular frequency is plotted in Fig. 4.2. For small values of F_0 the system starts with finite-amplitude solutions when $C_0 > 1$. The system's amplitude increases slightly with increasing F_0, for any fixed value of C_0. As F_0 increases further a sudden drop in $|B|^2$ is observed after approaching maximum amplitudes. This can be seen clearly in Figs. 4.1 and 4.2.

As a consequence, the higher value of C_0 the higher value of amplitude and dominant frequency of the solution, and visa versa. In contrast, the higher F_0 the lower the amplitude/dominant frequency solutions the system generates. Thus, the higher F_0 and lower C_0 are less efficient in generating finite-amplitude solutions.

In Figs. 4.1 and 4.2, two different regions can be observed. The first region (R_1) represents the area when the system exhibits finite-amplitude solutions. Different regular motions appear within this region. The other region (R_2) that appears as a dark blue area is linked with the system's damping solutions.

In contrast, in the region (R_2)(the dark blue area) A and B follow different structures; while B exhibits damping behaviour, A produces periodic solutions. In other words, in (R_1), A and B are coupled and have similar solutions. However, in (R_2), A takes a different from from B. A reasonable question that arises from the above study is what is the relationship between C_0 and F_0 when the system exhibits damping solutions? We thus presented a 2D diagram which shows the relationship between C_0 and F_0 when this change occurs.

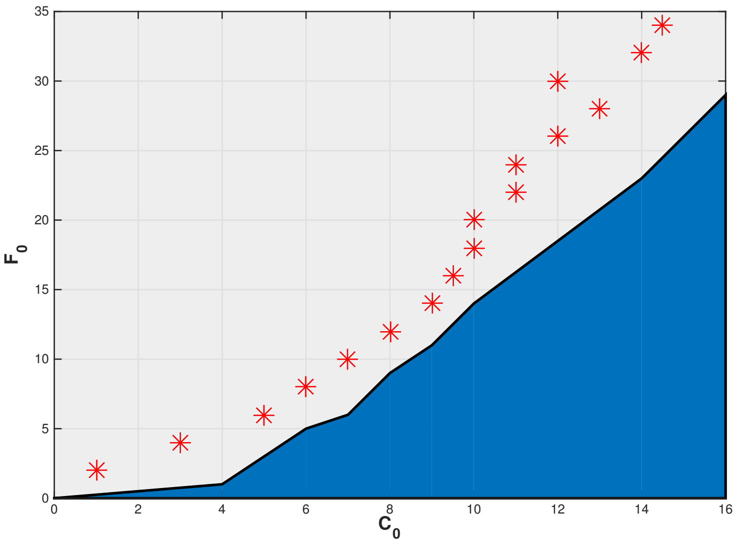

Figure 4.3: The coordinate of F_0 and C_0 when the maximum amplitudes occur is shown in red stars. The damping region is shown in blue.

Fig. 4.3 shows C_0 and F_0 coordinates of the highest peaks of the system's amplitude, represented by red stars. The blue area in Fig. 4.3 represents the relationship between F_0 and C_0 in the region of damping solution in (R_1), where a positive linear relationship between F_0 and C_0 is observed for $F_0 > 4$. This is similar to the findings in Chapter 2 / Mohamed and Kim (2014).

It is interesting to note that the results shown in Fig. 4.3 prove numerically that the Lorenz system (4.1) exhibits damping behaviour when $F_0 > 0.44C_0 + 3.8$. The relationship between C_0 and F_0 is linear. In addition, the boundary line between the regions (R_1) and $(R_2)$is given by $F_2 = 0.44C_0 + 3.8$.

As can be seen in Figs. 4.1 and 4.2, for fixed F_0 when the parameter C_0 grows, more chaotic structures appear, and (R_1) grows in size. However as F_0 is increased further, finite-amplitude solution changes to damping behaviour. It reminds us of the damping solution that occurred in Chapter 2. By comparing this result with our finding in Chapter 2, it can be seen that F_0 has quite similar effect as ω_1, with a different mechanism for $F_0 > 0$. Comparing this finding with the results obtained in case of $F_0 = 0$ using a time-dependent parameter $D = C_0 \cos(\omega_1 t)$ shown in Mohamed and Kim (2014), Fig. 4.1 and Fig. 4.2 provide us with a similar plot of $|B|^2$ and angular frequency as functions of C_0 and F_0.

However, one of the notable difference between these outcomes and the result presented in Chapter 2/Mohamed and Kim (2014) is that; the linear relationship, in this case, is $F_0 = 0.44C_0 + 3.8$, while the relationship between ω_1 and C_0 was given as $\omega_1 = 1.4465C_0 - 0.4212$, with higher tendencies than what is shown in Mohamed and Kim (2014). This linear relation has been seen in the case of using $D = C_0 \cos(\omega_1 t)$ as a control parameter. The effects of F_0 on the system are similar to those of ω_1 in Mohamed and Kim (2014). A positive linear relationship between F_0 and C_0 is observed for $F_0 > 4$.

4.3.2 CASE II: (AMPLITUDE OF A)

In the majority of previous studies e.g. Weiss et al. (1984), Sood and Kim (2014), it was sufficient to show the relevant results of either A or B. However, since different structures of A and B can be observed, we need to show $|A|^2$ as a function of F_0 and C_0 in addition to the results shown for the variable B in the subsection 4.3.1.

Fig. 4.4 shows the amplitude of A squared as a function of F_0 and C_0, for the same parameters that appear in Fig. 4.1.

Comparing the output amplitude that is shown in this case (Fig. 4.4) with the result that appears in Fig. 4.1 implies that A and B follow similar structures in the region of (R_1). However, as F_0 increases the damping behaviour present in

Fig. 4.1 becomes a band of periodical motion, where solutions with limit cycles occur.

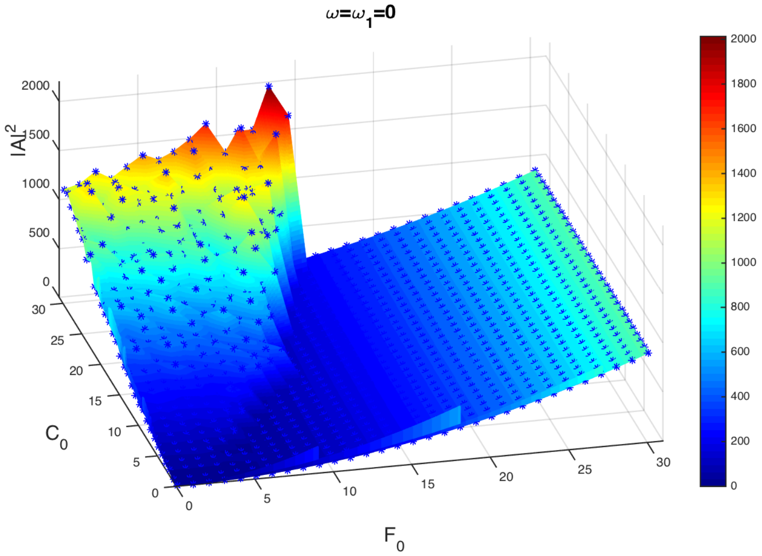

Figure 4.4: (a) 3D plot of A amplitude for fixed $D_0 = 2$.

The comparison between Fig. 4.1 and Fig. 4.4 indeed verifies that the waves of B are exponentially weak for higher values of F_0. This finding indicates that B transfers from cohesion to a state of disintegration; the exponential scaling expressed here would imply collapses of the term B, while A recovers as a result of a direct relationship with the driving force F_0. Therefore, the external force F_0 has the potential role to change the mechanism for the generation A. In contrast F_0 can not change the dynamics of B.

The dynamics of term A depends explicitly on the driving force F_0. The blue region in Fig. 4.3(b) also represents the coordinates of C_0 and F_0 where the splitting in the behaviour of A and B is made.

To provide a clear picture of what is happening in each region when C_0 is fixed with varying F_0, we need to study the following two cases;

Case 1: Results for fixed $C_0 = 3$ and varying F_0

The values of the internal force C_0 and the external forcing F_0 are chosen carefully to show how the system's solutions exhibit different behaviour.

In order to understand how A and B change their dynamical structures for varying F_0, we need to look closely to highlight the differences between the behaviour of the amplitudes of A and B.

Analysing the dynamical response of the system for each value of C_0 and F_0 is extremely difficult. Consequently, we will fix C_0 and vary F_0 in this case.

As an example, we consider $C_0 = 3$ to show how the system changes its behaviour regarding varying F_0 as plotted in Fig. 4.5. The red circles correspond to $Log|A|^2$, while the blue circles corresponding to $Log|B|^2$. It is apparent that the solutions A and B exhibit finite-amplitude solutions for small F_0, and around $F_0 = 5.22$ a sudden drop in $Log|B|^2$ is obvious seen. For $F_0 < 5.22$ the solutions trajectories of $Re(A)$ and $Re(B)$ oscillates with limit cycles. However, for $F_0 > 5.22$ the solution trajectory of $Re(A)$ spirals and then approaches the value of F_0. In contrast, during this period the trajectory of $Re(B)$ exhibits damping behaviour.

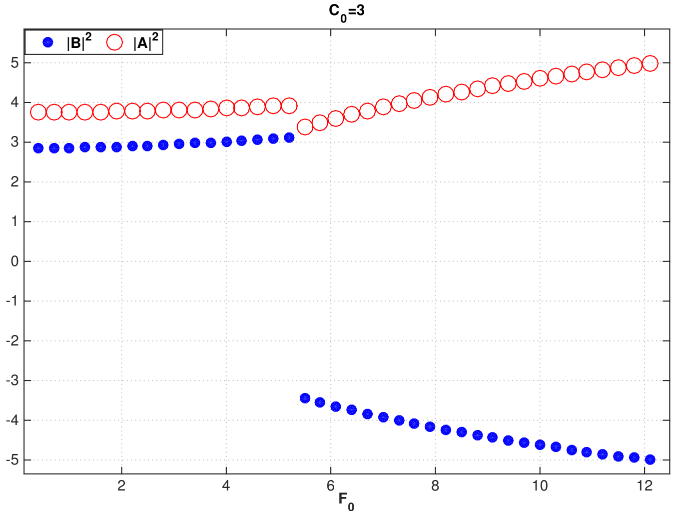

Figure 4.5: $Log|B|^2$ in blue and $Log|A|^2$ in red as function of F_0 for fixed $C_0 = 3$.

This demonstrates that if F_0 lies in the interval $[0, 5.22)$ the corresponding solutions of A and B are of finite-amplitude. However, for higher F_0 $(F_0 > 5.22)$, damping and periodic solutions do exist for B and A respectively. To perceive how the system behaves in each region we will consider two different positions of F_0, one in the interval $[0, 5.22)$ and the other for $F_0 > 5.22$ as following;

- First, in the region (R_1); for chosen $F_0 = 1$ (where F_0 can be any value that satisfies $F_0 < 5.22$), we plot the system's solution in a phase-space in Fig. 4.6. The time series of both components A and B oscillated in periodic behaviour, with a similar trend, and different amplitudes, as shown in Fig. 4.7.

- Second, in the region (R_2); we consider a higher F_0 at $F_0 = 7$ (F_0 can be any value which satisfies $F_0 < 5.22$) to make the effect of the additive force more apparent. The solutions' trajectories as a function of time are plotted in Fig. 4.8. It is obvious that $Re(A)$ and $Re(B)$ start to separate after few iterations, and their paths remain that of different behaviour over time.

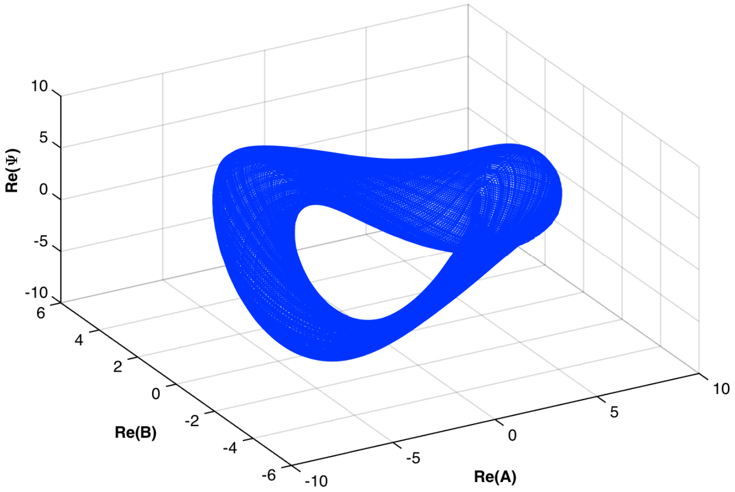

Figure 4.6: Phase space portrait of the system's components $Re(A)$, $Re(B)$ and $Re(\Psi)$ in X, Y and Z axises, respectively, for $C_0 = 3$ and $F_0 = 1$

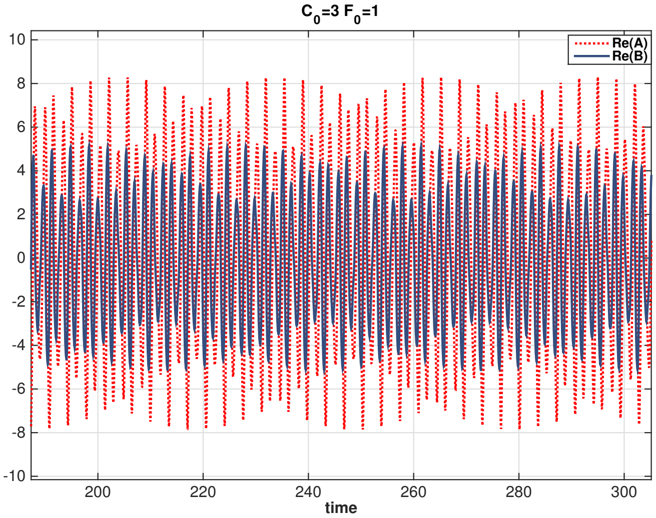

Figure 4.7: Time-domain of $Re(A)$ in red dashed line and $Re(B)$ in blue continuous line, for $C_0 = 3$ and $F_0 = 1$, when the system is exhibiting finite-amplitude solutions, for $C_0 = 3$ and $F_0 = 1$.

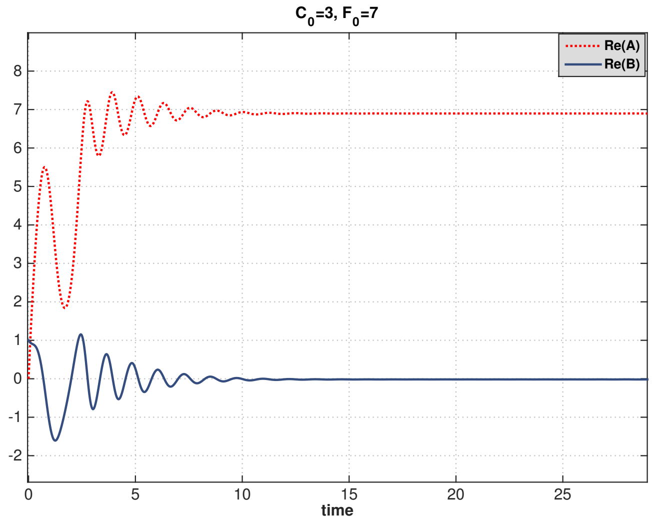

Figure 4.8: Time-domain of $Re(A)$ in red dashed line and $Re(B)$ for $C_0 = 3$ and $F_0 = 7$, when the system exhibiting finite amplitude solution.

Fig. 4.8 shows the solutions' trajectories of A in a red dashed line and B in a continuous blue line with increasing time. The trajectories of A and B have completely different behaviour. More precisely, the time series of A stick on a constant with very close value to F_0. However, the solution of B shows a damping structure.

We repeated these steps for several values of C_0, and then determine that as we increase C_0 for varying F_0 the system spends longer time to approach the damping status. For all of the values of C_0 examined, we obtained that all solutions of A and B go to the same attractors F_0 and zero, respectively. As the external forcing F_0 increases, the magnitude and period of these oscillations shrink, as well as the time the solution orbit A reaches its fixed point.

In general, the system's structure for varying C_0 and F_0 has two features; for any value of $F_0 < 0.44C_0 + 3.8$ (R_1) the system exhibits finite-amplitude solutions, and A and B own the same structures; for $F_0 > 0.44C_0 + 3.8$ (R_2) the component A has completely different behaviour from B.

The dynamics of the system's components after passing the boundary $F_0 = 0.44C_0 + 3.8$ typically exhibit one of the two types of behaviour, periodic or death oscillations. While A exhibits periodic oscillations, B exhibits damping solutions. A strong interaction between A and F_0 occurred because the system is forced through the first equation that represents the change in A with time.

Case 2: Varying C_0 for fixed $F_0 = 1$

In case 1 we fixed $C_0 = 3$ and varied F_0 to see the system response. We found that smaller F_0 is more efficient in generating finite-amplitude solutions. As a consequence F_0 needs to be a small value to ensure the production of finite-amplitude solutions. Therefore, we will set as $F_0 = 1$ and vary C_0.

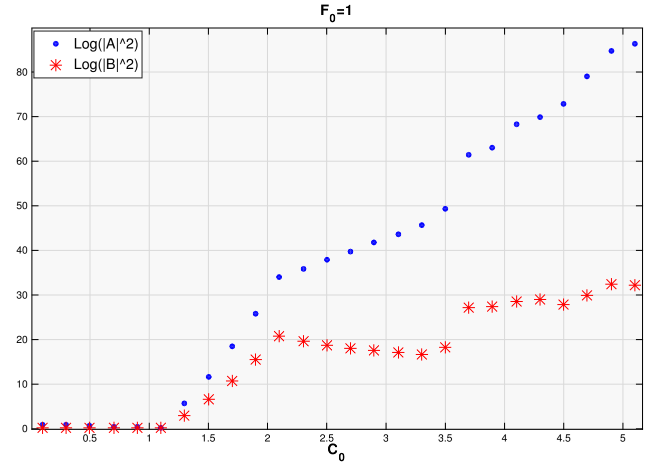

Figure 4.9: $Log|A|^2$ and $Log|B|^2$ against C_0 for fixed $F_0 = 1$.

Fig. 4.9 illustrates the strength of $Log|A|^2/Log|B|^2$ as a function of C_0 for fixed

$F_0 = 1$ and varying C_0. After the first bifurcation occurs around $C_0 = 1.1$ both $Log|A|^2$ and $Log|B|^2$ increase slowly with increasing C_0 for $C_0 > 1.1$. However, for $2.1 < C_0 < 3.4$, $|B|^2$ decreases slightly with increasing C_0. The decline in $|B|^2$ in this period is induced by the quenching of Ψ, which is a result of the Lorentz force of magnetic fields. The overview of Fig. 4.9 shows an increase in the amplitude squared of both A and B with increasing C_0. A small decrease in $|B|^2$ can be seen for $C_0 \in [2, 3.4)$. To illustrate the basic mechanism for the system for different C_0 at $F_0 = 1$, we plot the system phase space in four different positions of C_0 as shown in Fig. 4.10.

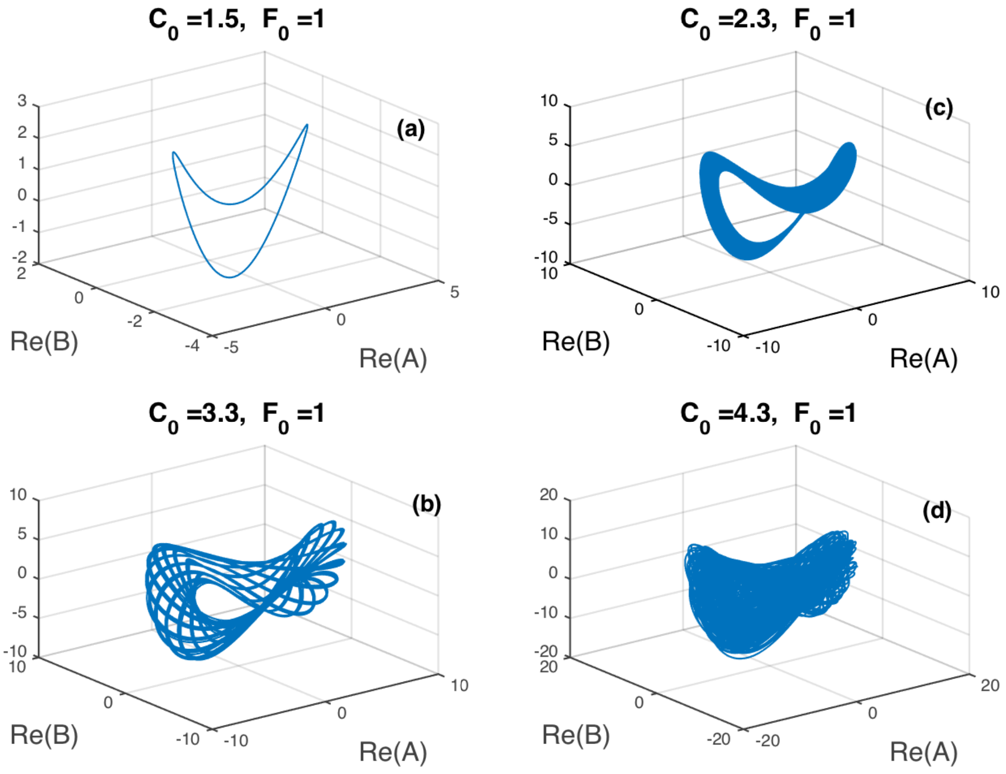

Figure 4.10: Phase trajectories for four different values of C_0 at $F_0 = 1$. (a) $C_0 = 1.5$, the case of limited oscillating solution; (b) and (c) the system's orbits when periodic oscillation solutions observed, for $C_0 = 2.3$ and $C_0 = 3.3$, respectively; and (d) an example of chaotic oscillating.

To this end, we now study the system response for non-zero equal driving frequencies ω_1 and ω.

§ 4.4 The Linear Growth Rate for Varying C_0 and $\omega = \omega_1$ for $F_0 = 1$

The linearisation allows us to get some information about our nonlinear dynamical model, as in the linear system any changes in a parameter do not affect the qualitative nature of the behaviour.

The principal idea is to find out how the solutions of the linearised version of the Lorenz system behave for varying ω_1 and ω. Thus we will be able to compare our results with the nonlinear case.

In particular, here we will show how the system's growth rate is affected by changing the driving frequencies.

Since our numerical analysis indicates that the system goes through damping region for higher F_0, we choose $F_0 = 1$ in order to see the system's response to a small external force (for large F_0, the system has zero amplitudes, i.e. the solution approaches zero).

Fig. 4.5 shows the system's growth rates as a function of C_0 for four fixed driving frequencies ($\omega_1 = \omega = 0, 1, 2,$ and 5) at $F_0 = 1$, obtained numerically using the linearised model equations. The corresponding growth rate of each ω_1 increases in magnitude as C_0 increased. The growth rate curves have lower magnitudes for higher ω_1. It is also worth noting that there is no distinct difference between the growth rates of $\omega_1 = 1$ and $\omega_1 = 2$.

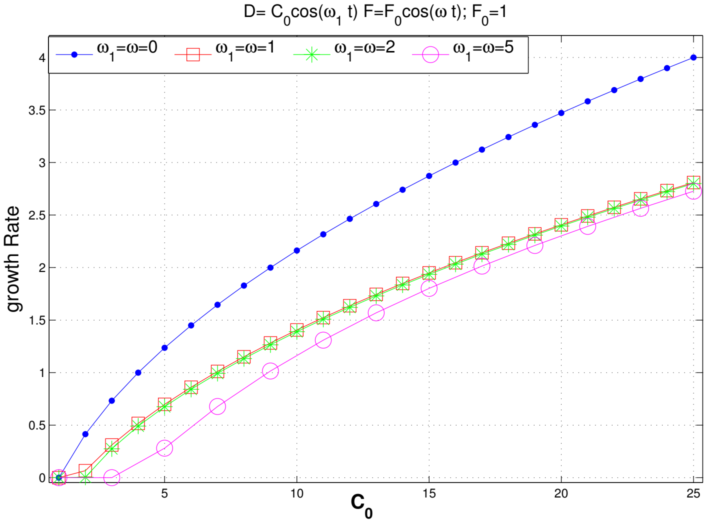

Figure 4.11: The linear system's growth rate for varying C_0 and fix $F_0 = 1$ and $\omega = \omega_1 = 0, 1, 2$ and 5

§ 4.5 Nonlinear Results for Varying C_0 and $\omega_1 = \omega$ for $F_0 = 1$

The previous section has shown how the linearised Lorenz system operates for the case of fixed $F_0 = 1$ and varying C_0.

To extend these results, we will illustrate some of the changes that occur in the system at $F_0 = 1$ in the non-linear version. Throughout this section, the possibility of more damping solutions than the previous section as a result of the nonlinearity is expected.

The idea is to see how the system is affected by changing more than one parameter at the same time. A typical correlation takes the form of Fig. **??** (a) and Fig. **??**(b).

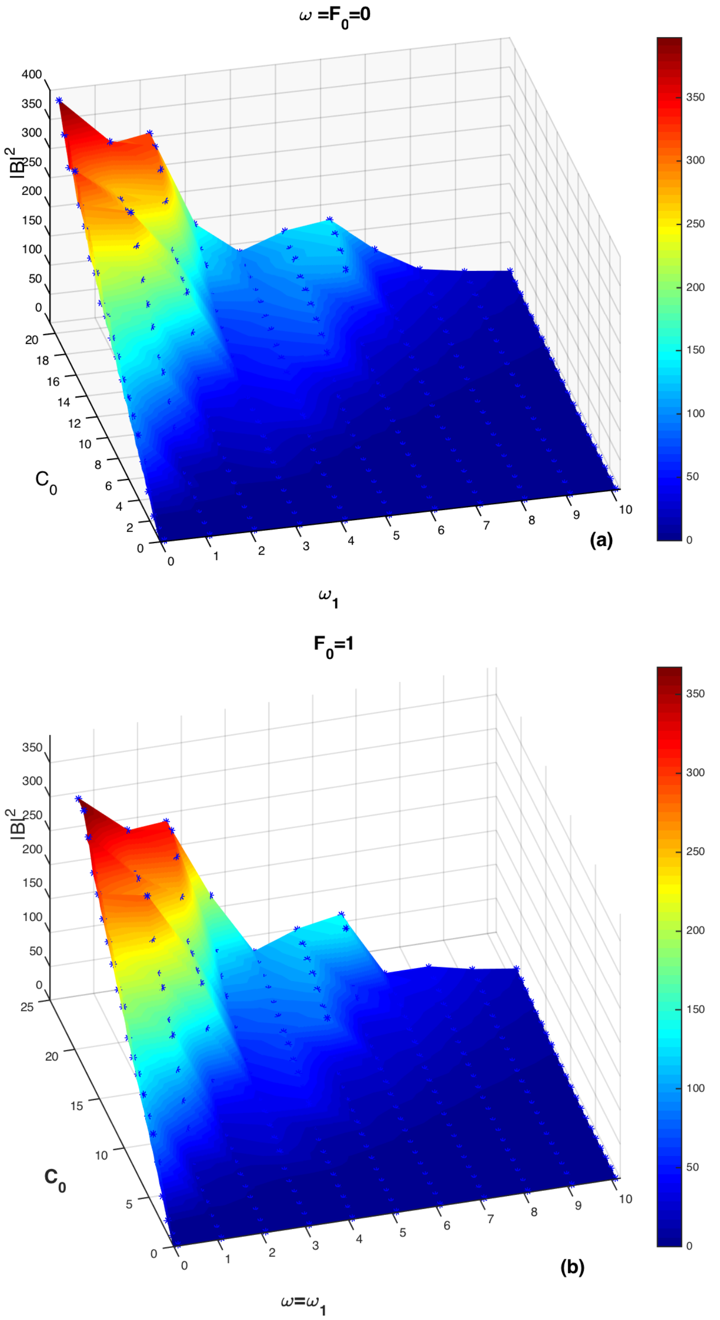

Figure 4.12: (a) $|B|^2$ as a function of C_0 and ω_1 for $F_0 = 1$;(b) $|B|^2$ as a function of C_0 and ω_1 for $F_0 = 0$.

Fig. 4.12 a and 4.12 b show 3D plots of the amplitude squared of B as a function of C_0 and ω_1/ω when the parameter $F_0 = 0$ and $F_0 = 1$, respectively.

Adding a small F_0 makes no significant difference to the overall trend in the system's amplitude and mechanism. The comparison between these two figures illustrates general similarity trends, as can be seen. The only obvious difference is the system produced higher amplitudes is produced at $F_0 = 0$, as illustrated in 4.12 (a).

It can be seen for a higher C_0, the additive force provides an appropriate condition for the system's amplitude to grow. We see that the maximum amplitude for fixed C_0 occurs when $\omega_1 = \omega = 0$. These results inform us that driving the system with the same internal ω_1 and external ω as driving frequencies can not make distinguished changes in the system's mechanism. Therefore, we in the following section will study the system through finding the system's amplitude as a function of ω_1 and ω.

§ 4.6 Results for varying ω_1 and ω, and fixed value of $C_0 = 1$

In this section, we will examine the system's reaction to varying both driving frequency to obtain some idea of how the solutions of the given equation behave for fixed $C_0 = 1$ (C_0 can be any other value). Fig. 4.13 shows 3D plots for the amplitude of B $|B|^2$ as a function of ω and ω_1 for four different values of F_0. Apparently, damping structure is a general feature of the system, excluding a small period of ω, and ω_1 where small amplitude can be seen.

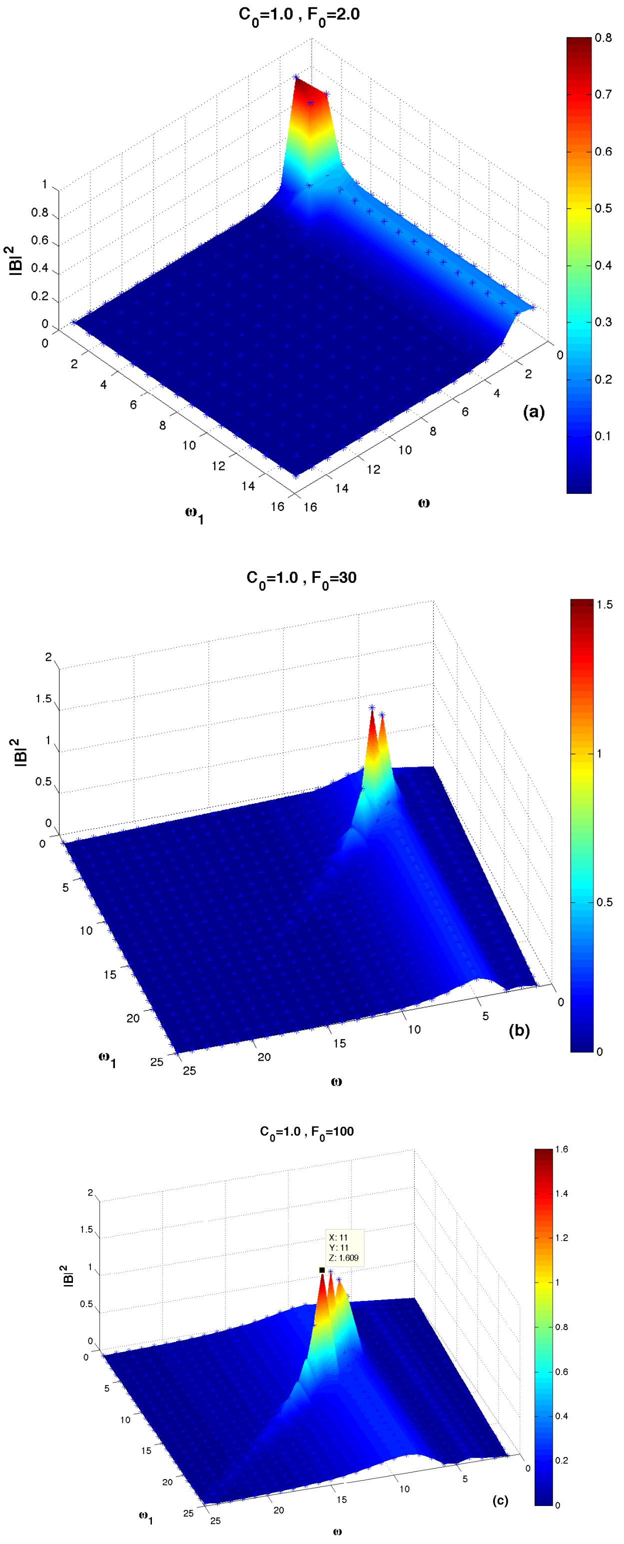

Figure 4.13: For $C_0 = 1$, 3D for $|B|^2$ as a function of ω and ω_1 for $F_0 = 2,\ 30$ and 100 in (a), (b) and (c) respectively.

We first have to pick some values for the parameter F_0. Since the analysis of the Lorenz system indicates that the stability characteristics does not depend on the external force F_0, it does not much matter what we choose for F_0. Note that the position of the mountain (highest peaks) depends on the values of F_0. It is useful to look at the phase-space of the system's solution at the highest a peak and the output frequency. We aim to find if there are any relationship between the driving and the output frequencies. It appears that in this situation the system goes through damping state for all values of ω and ω_1, with the exception of some values where a clear finite-amplitude solution can be noted.

The series in the figures 4.13a-c are clear confirmations of this behaviour, where very sharp and high peaks can be seen.

This process exhibited by the system's dynamo operates for almost all the values of ω_1 and ω, apart from the line that represents $\omega_1 = \omega$.

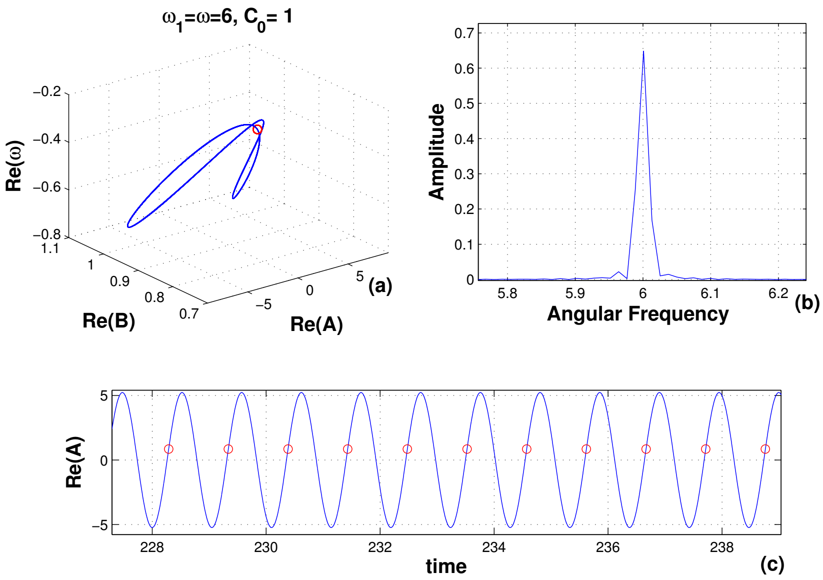

Figure 4.14: Results of the numerical solution for the system (4.1) when (C_0, F_0, ω_1, ω)=(1, 30, 6, 6). The red circles represent the Poincaré section. (a) The system phase-space; (b) Angular frequency; (c) the time series.

Fig. 4.14 a shows the phase-space of the solution for $\omega_1 = \omega = 6$.

Furthermore, the maximum amplitude appears when the driving frequencies are equal to the system output frequency. This phenomenon is identified as stochastic resonance. To show this, we will plot the system's solution and the frequency spectrum at the highest peaks, as shown in 4.15.

In this case, if the driving frequency is approaching the natural frequency, the energy is transported in the system with very small resistance. This makes the amplitude of the producing oscillations very exaggerated and much higher than of the driving force's amplitude.

Interestingly, the height of these peaks has a linear relationship with F_0, as shown in Fig 4.15.

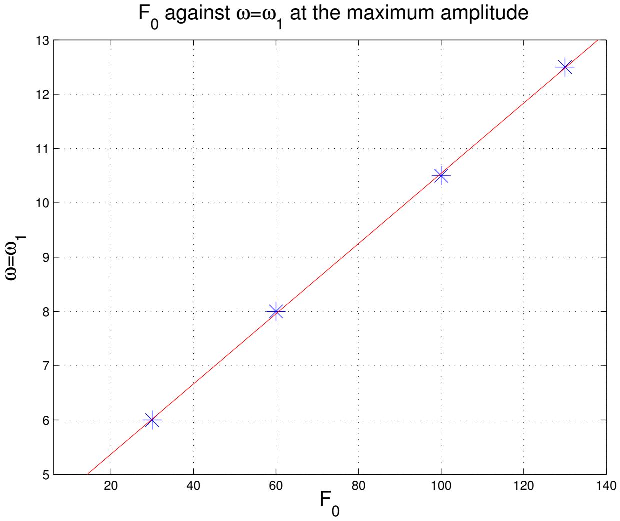

Figure 4.15: The maximum peaks of $|B|^2$ as a function of F_0

So far in our simulation we showed that F_0 has a strong linear relationship with the maximum peaks of $|B|^2$ exhibited in Fig. 4.13. For $F_0 = 2$, a different feature of the system's amplitude can be observed with one peak different from the case $F_0 = 30$. In fact, there are two features. Firstly, for $F_0 \leq C_0$ one sharp mountain can be noticed as illustrated in Fig. 4.13a, which is a very similar to what we obtained in the case of $C_0 = 1$ in the previous case. Secondly, for $F_0 \geq C_0$ multi-peak mountains occur around along $\omega = \omega_1$, as can be observed in 4.13b. These mountains become longer in duration with increasing F_0.

§ 4.7 Discussion and Conclusion

In summary, the present chapter presents the Lorenz system's response to two forcing. This is the extension of in Chapter 2 by driving the system with including the external forcing $F = F_0 \cos(\omega t)$ into the first equation in the Lorenz system under investigation. We used this technique to understand the system reaction to an external periodic force when the internal control parameter is not zero.

- We found two-types of solutions, one driven by the dynamo number when A and B coupled and the other driven by the additive force when A and B are decoupled, and we examine the cross-over between these two types of solutions.

- First, we started with the case when the dynamo number and the additive force are constants, i.e. with the driving frequencies $\omega_1 = \omega = 0$. We found that the main effect of the external force's amplitude F_0 is that it drives the system component B from finite-amplitude solutions into damping behaviour. In contrast, the external additive force drives the component A into periodic oscillation orbits, and the amplitude of A approaches the driving force F_0.

- Second, we examined the effects of varying the driving frequencies ω_1 and ω for fixed $C_0 = 1$ for some values of F_0. In this case, the system goes through resonance when driving frequencies ω_1 and ω are equal. The effects of changing one of the parameters of the system are demonstrated by 3D plots to show the general behaviour. Also, time series and phase space have been plotted to illustrate the detailed behaviour of the system for selected values of the parameters.

We found that Stochastic resonance (SR) occurs in the system for fixed $C_0 \gg F_0$ when the driving frequencies ω_1 and ω are equal.

- Also, in the case of non-zero driving frequencies for small additive force $F_0 = 1$, the system remains almost the same behaviour as for $F_0 = 0$, apart from a higher amplitude being observed. In comparison to the previous study shown in Chapter 2 using one time-dependent parameter $D = C_0 \cos(\omega_1 t)$, this chapter shows a much richer feature of the solution.

The approach used in this chapter can be applied to control other dynamical systems such as Rössler.

Chapter 5

Concluding Remarks

As summaries have been provided at the end of each chapter, the aim of this chapter is to provide a concise conclusion to this dissertation. The motivation for this thesis was to study the mechanism of the Lorenz system numerically.
We applied three different approaches in order to control the Lorenz system, which is used to model the process of generating the magnetic field in sunspots. We investigated the Lorenz system's response for different parameters and performed descriptions of the system's solutions that generated from computer simulations.

In Chapter 2, $D = C_0 \cos(\omega_1 t)$ was used as a control parameter to study the system's responses. One of the main results we obtained was shown in Fig. 2.15, that revealed the occurrence of a linear relationship between C_0 and ω_1 at the bifurcation points $\omega_1 = 1.4465C_0 - 0.4212$. The principal theoretical implication of this study is that smallerω_1 and higher C_0 is more valuable for the system to generate finite-amplitude solutions.

Chapter 3 was intended to determine the impact of using a non-zero mean value time-dependent parameter as $D = D_0 + C_0 \cos(\omega_1 t)$. The results of this analysis show that both the linearised system has different results from the nonlinear system for finite frequency ω_1 but are similar for sufficiently large ω_1;
(i) the maximum linear growth rate occurs due to the parametric instability at $\omega_1 = 4\omega_0$ as long as C_0 is not significantly larger than D_0;
(ii) the minimum nonlinear response occurs at $C_0 \approx D_0 + 1$ when the system remains in the DZ for the longest time;
(iii) the minimum nonlinear response for ω_1 occurs fairly close to the natural frequency for small C_0 and D_0;
(iv) the impact of the oscillatory control parameter disappears both linearly and nonlinearly for enough large ω_1, with a linear relation between ω_1 and C_0, similar to the case of a purely oscillatory control parameter Mohamed and Kim (2014).
In Chapter 4, internal ($C_0 \cos(\omega_1 t)$) and external ($F_0 \cos(\omega_1 t)$) parameters were used to control the system. It is an expansion of the subject studied in Chapter 2.
We found that:

- There was a linear relationship C_0 and F_0 when the system exhibits damping behaviour.
- Smaller F_0 and higher C_0 is more efficient in generating finite-amplitude solutions.
- A stochastic resonance appears as a result of the interaction between the external driving force and the system when driving frequencies ω_1 and ω are equal to the system's output frequency.

This dissertation has introduced new contributions in the area of controlling parameters in non-linear dynamical systems.

Chapter 6

Future Work

In this thesis we have studied the Lorenz system for the ordinary derivative. This research has raised many questions in need of further investigation. There are several approaches in which this work could be extended in the future.

- Extend the Lorenz system to be:

$$\begin{aligned}\dot{A}(t) &= 2DB(t) - A(t),\\ \dot{B}(t) &= i(1 + Ucos(\theta t))A(t) - 0.5iA^*\Psi(t) - B(t),\\ \dot{\Psi}(t) &= -iA(t)B(t) - \nu\Psi(t).\end{aligned} \tag{6.1}$$

- Extend the Lorenz system using viscosity of the flow to a time dependent parameter $\nu = \nu_0 cos(\zeta t)$

$$\begin{aligned}\dot{A}(t) &= 2DB(t) - A(t),\\ \dot{B}(t) &= iA(t) - 0.5iA^*\Psi(t) - B(t),\\ \dot{\Psi}(t) &= -iA(t)B(t) - \nu_0 cos(\zeta t)\Psi(t).\end{aligned} \tag{6.2}$$

- **Despite spending almost a year in engaging with the fractional derivative project we have yet been unable to obtain high accuracy results for the higher parameter D.**

  This involved around three months of researching about the project's background. The rest of the year was spent on developing a numerical code and simulations.

Until recently, there has been little interest in fractional calculus, despite it being more than 300 years old. Few mathematicians contributed to this subject over the years.

However, over the past 30 years there has been a significant increase in amount of research which involves fractional derivatives in solving differential equations. The fractional derivative applications to physics have begun recently Hilfer (2000), Sun and Sprott (2009). One of the main objects of the fractional-order systems is that a memory is included in the system Yang and Zeng (2010).

Several definitions of fractional derivatives are known; the Riemann-Liouville formation is probably the best Grigorenko and Grigorenko (2003). The definition of the fractional derivative of the Riemann-Liouville derivative Oldham and Spanier (1974) Baleanu et al. (2010) is given as follows:

$$\frac{\partial^{\alpha} f(t)}{dt} = \frac{1}{\Gamma(n-\alpha)} \frac{d^n}{dt^n} \int\limits_{a}^{t} \frac{f(\tau)}{(t-\tau)^{\alpha-n+1}} d\tau$$

where Γ is gamma function and n is an integer number chosen as $n-1 < \alpha < n$. Another definition was presented by Caputo with 0 lower integral limit, which is the adjustment of the Riemann-Liouville derivative. The

Caputo of order α is defined as

$$\frac{\partial^\alpha f(t)}{dt} = \frac{1}{\Gamma(n-\alpha)} \int\limits_0^t \frac{f(\tau)}{(t-\tau)^{\alpha-n+1}} d\tau$$

Now let us consider the fractional generalisation of the Lorenz system as:

$$\begin{aligned} \frac{d^\alpha}{dt}A(t) &= 2DB(t) - A(t), \\ \frac{d^\beta}{dt}B(t) &= iA(t) - 0.5iA^*\Psi(t) - B(t) \\ \frac{d^\gamma}{dt}\Psi(t) &= -iA(t)B(t) - \nu\Psi(t). \end{aligned} \tag{6.3}$$

Here, we suppose $0 < \alpha, \beta, \gamma \leq 1$ The system (6.3) for $\alpha = \beta = \gamma = 1$ represents the Lorenz system Weiss et al. (1984).

Bibliography

A. Anderson, M. N. Chaplain, E. Newman, R. Steele, and A. Thompson. Mathematical modelling of tumour invasion and metastasis. *Journal of Theoritical Medicine*, 2:129–151, 2000.

V. S. Anishchenko, A. B. Neiman, and M. A. Safanova. Stochastic resonance in chaotic system. *Journal of Statistical Physics*, 70:183–196, 1993.

V. A. Apety. *Chaotic dynamical systems*. Submitted in partial fulfillment of a postgraduate diploma at AIMS. Stellenbosch University, South Africa, 2011.

H. W. Babcock. The topology of the suns magnetic field and the 22-year cycle. *Astrophysical Journal*, 133:572–587, 1961.

D. Baleanu, K. Diethelm, E. Scalas, and J. J. Trujillo. *Fractiona calculus*. World Scientific, Southern Illinois University of Edwardsville, USA, 2010.

A. Becker and L. Kremer. Linear stability analysis for bifurcations in spatially extended systems with fluctuating control parameter. *Physica D*, 90:408–430, 1996.

R. Benzit, A. Sutera, and A. Vulpiani. The mechanism of stochastic resonance. *J. Phys. A: Math. Gen*, 14:453–457, 1981.

A. Bhattacharyaya and J. K. Bhattacharjee. Pattern formation in reaction diffusion systems: a galerkin model. *Eur. Phys. J. B*, 21:561–566, 2001.

S. Boccaletti, C. Grebogi, Y. C. Lai, H. Mancini, and D. Maza. The control of chaos: Theory and applications. *Physics Reports*, 329:103–197, 2000.

G. Bond, B. Kromer, J. Beer, R. Muscheler, M. N. Evans, W. Showers, R. Hoffmann, S. Lotti-Bond, I. Hajdas, and G. Bonani. Persistent solar influence on north atlantic climate during the holocene. *Science*, 69(3):563–668, 2001.

L. A. Bunimovich. Short-and long-term forecast for chaotic and random systems (50 years after lorenz's paper). *Nonlinearity*, 27:51–60, 2014.

E. Chaisson and S. McMillan. *Astronomy Today*. Addison-Wesley, 2011.

F. Chapeau-Blondeau and X. Godivier. Theory of stochastic resonance in signal transmission by static nonlinear systems. *Physical Review E*, 55:1478–1495, 1997.

P. Charbonneau, J. Christensen-Dalsgaard, R. Henning, R. M. Larsen, J. Schou, M. J. Thompson, and S. Tomczyk. Helioseismic constraints on the structure of the solar tachocline. *Astrophysical Journal*, 527:445–460, 1999.

M. Chen and Z. Han. Controlling and synchronizing chaotic genesio system via nonlinear feedback control. *Chaos, Solitions and fractals*, 17:709–716, 2003.

A. Crisanti, M. Falcioni, G. Paladin, and A. Bulpiani. Characterization of a periodically driven chaotic dynamical system. *J. Phys. A: Math. Gen.*, 30: 371–383, 1997.

K. M. Cuomo, A. V. Oppenheim, and S. H. Strogatz. Synchronization of lorenz-b ased chaotic circuits with applications to communications. *IEEE*, 40:626–633, 1993.

K. W. Dam and H. S. Lin. *cryptography's role in securing the information society.* National Academy Press, Washington, D.C., 1996.

S. Douglas, M. Mohamed, and E. Kim. Confinement improvement by fluctuating input power. *Physics of Plasmas*, 20:114504–4p, 2013.

M. I. Dykman and M. A. Krivoglaz. Classical theory of nonlinear oscillator interacting with a medium. *Soviet Physics Reviews, Harwood Academic, New York,*, 48:495512, 1984.

H. Dym and H. P. Mckean. *Fourier Series and Integrals.* Academic Press. 1972.

J. A. Eddy, F. R. Stephenson, and K. K. C. Yau. On pre-telescopic sunspot records. *Quarterly Journal of the Royal Astronomical Society*, 30:65–73, 1989.

A. Gailitis, O. Lielausis, E. Platacis, G. Gerbeth, and F. Stefani. Laboratory experiments on hydromagnetic dynamos. *Reviews of modern Physics*, 74, 2002.

H. Gang, T. Ditzinger, C. Z. Ning, and H. Haken. Stochastic resonance without external periodic force. *Physical Review Letters*, 71:807–810, 1993.

P. Gaspard. Rossler systems. *Encyclopedia of Nonlinear Science*, 231:808 – 811, 2005.

R. Graham. Hoft bifurcation with fluctuating control parameter. *Phys. Rev. A*, 25:3234–3258, 1982.

I. Grigorenko and E. Grigorenko. Chaotic dynamical of the fractional lorenz system. *Physical review letters*, 91(3):034101, 2003.

F. Guo-Lin and H. Wen-Ping. amplitude death in steadily forced chaotic systems. *Chinese Physics*, 16:2825–2830, 2007.

J. Haigh. The effects of solar variability on the earth's climate. *hilos T. Roy. Soc. A*, 361:95–111, 2003.

J. D. Haigh. Modelling the impact of solar variability on climfate. *J. Atmos. Terr. Phys.*, 61:63–72, 1999.

G. E. Hale. On the probable existence of a magnetic field in sun-spots. *Astrophys. J.*, 28:315–343, 1908.

G. E. Hale, F. Ellerman, S. B. Nicholson, and A. H. Joy. The magnetic polarity of sunspots. *Astrophysical Journa*, 49:153–186, 1919.

D. H. Hathaway. Photospheric features nasa@ONLINE, 2014. URL `http://solarscience.msfc.nasa.gov/feature1.shtml`.

D. H. Hathaway, R. M. Wilson, and E. J. Reichmann. The shape of the sunspot cycle. *Solar Physics*, 151:177–190, 2009.

D.H. Hathaway, R.M. Wilson, and E. J. Reichmann. The shape of the sunspot cycle. *Solar Physics*, 151:177–190, 1994.

R. Hilfer. "an introduction to fractional calculus." ch. 1 in applications of fractional calculus in physics. *Singapore: World Scientific*, pages 1–85, 2000.

D. V. Hoyt and K. H. Schatten. Group sunspot numbers: a new solar activity reconstruction. *Solar physics*, 69(179):189–219, 1998.

M. Hu, Z. Xu, R. Zhang, and A. Hu. Parameters identification and adaptive full state hybrid projective synchronization of chaotic (hyper-chaotic) systems. *Physics Letters A*, 361:231–237, 2007.

C. A. Jones, N. O. Weiss, and F. Cattaneo. Nonlinear dynamos: A complex generalization of the lorenz equations. *Physica D: Nonlinear Phenomena*, 14: 161–176, 1985.

D. S. Jones, M. J. Plank, and B. D. Sleeman. *Deferential Equations and Mathematical Biology.* 2nd Ed. CRC Press Taylor and Francis Group, 2009.

C. Letellier, L. A. Aguirre, J. Maquet, and R. Gilmore. Evidence for low dimensional chaos in sunspot cycles. *Astronom. Astrophys.*, 449:379–387, 2006.

J. H. Li, Y. X. Hana, and S. G. Chen. System with spatially periodic potential field and subject to multiplicative noise. *Physica D*, 195:67–76, 2004.

E. N. Lorenz. Deterministic non-periodic flow. *J. Atmospheric Sci.*, 20:130–141, 1963.

J. Lu and J. Lu. Controlling uncertain lu system using linear feedback. *Chaos, Solitons and Fractals*, 17:127133, 2003.

J. LÜ, T. Zhou, G. Chen, and S. Zhang. Local bifurcatios of the chen system. *International Journal of Bifurcation and Chaos*, 12:2257 – 2270, 2002.

J. Major. How big are sunspots?@ONLINE, 2012. URL `http://www.universetoday.com/95232/how-big-are-sunspots/`.

M. Moghtadaei and M. R. H. Golpayegani. Complex dynamic behaviors of the complex lorenz system. *Scientia Iranica*, 19:733–738, 2012.

M. Mohamed and E. Kim. Oscillatory control parameters in nonlinear chaotic systems. *Phys. Scr.*, 89:1–8, 2014.

M. Mohamed and E. Kim. Parametric instability and nonlinear feedback. *Under submition*, 2015.

A. Neiman, P. I. Saparin, and L. Stone. Coherence resonance at noisy precursors of bifurcations in nonlinear dynamical systems. *Physical Review E*, 56:270–273, 1997.

A. Newton and E. Kim. Effect of stochasticity in mean field dynamo models. *Phys. Plasmas*, 19:1–10, 2012.

I. Nicolson. *The Sun.* The Royal Astronomical Society, London, 1982.

R. W. Noyes. *The Sun, our star.* Havard University Press. Cambridge University, 1982.

K. B. Oldham and J. Spanier. *The Fractional Calculus.* Academic Press, San Diego, 1974.

M. E. Orme and M. A. J. Chaplain. A mathematical model of vascular tumour growth and invasion. *Math. Comp. Modelling*, 23:43–60, 1996.

D. A. Ostlie and B. W. Carroll. *An Introduction to Modern Stellar Astrophysics.* 1996.

E. Ott. *Chaos in dynamical systems.* 1st Ed, Cambridge University Press, UK, 1993.

E. N. Parker. The generation of magnetic fields in astrophysical bodies: Xmagnetic buoyancy and the solar dynamo. *Astrophys. J.*, 198:205–214, 1975.

E. N. Parker. *Cosmical magnetic fields.* Oxford University, 1979.

U. Parlitz and W. Lauterborn. Period-doubling cascades and devil s staircases of the driven van der pol oscillator. *Physical Review A*, 36:1428–1434, 1987.

A. S. Pikovsky and J. Kurths. Coherence resonance in a noise-driven excitable system. *Physical Review Letters*, 78:776–778, 1997.

J. Priede, R. Avalos-Zuniga, and F. Plunian. Homopolar oscillating-disc dynamo driven by parametric resonance. *Phys. Lett. A*, 374:584–587, 2010.

M. R. E. Proctor. Pattern formation in reaction diffusion systems: a galerkin model. *Monthly Notices of the Royal Astronomical Society: Letters*, 382:39–42, 2007.

S. Rajasekar and M. Lakshmanan. Period- doubling bifurcations, chaos, phase-locking and devil's staircase in a bonhoffer-van der pol oscillator. *Physica D*, 32:146–152, 1988.

P. Reimann. Brownian motors:noisy transport far from equilibrium. *Physics Reports*, 361:257265, 2004.

J. A. Revelli, M. A. Rodriguez, and H. S. Wio. Resonant phenomena in extended chaotic systems subject to external noise the lorenz96 model case. *Physica A*, 387:3103–3110, 2008.

R. M. Russell. Windows two universe@ONLINE, 2010. URL `http://www.windows2universe.org/sun/atmosphere/sunspots.html`.

D. T. Shindell, G. A. Schmidt, D. Mann, M. E. Rind, and A. Waple. Solar forcing of regional climate change during the maunder minimum. *SCIENCE*, 294:2149–2152, 2001.

D. S. A. Simakov and J. Perez-Mercader. Noise induced oscillations and coherence resonance in a generic model of the nonisothermal chemical oscillator. *Scientific Reports*, 3:1–10, 2013.

S. Sinha. Noise-free stochastic resonance in simple chaotic systems. *Physica A*, 270:204–214, 1999.

D. Sokoloff. The maunder minimum and the solar dynamo. *Solar Physics*, 224: 145–152, 2004.

S. K. Solanki, B. Inhester, and M. Schussler. The solar magnetic field. *Reports on progress in physics*, 69(3):563–668, 2006.

A. Sood and E. Kim. Dynamic model of dynamo (magnetic activity) and rotation. *Astronomy and Astrophysics*, 555:A22–11pp, 2013.

A. Sood and E. Kim. Detailed mathematical and numerical analysis of a dynamo model. *Astronomy and Astrophysics*, 563:A100–12pp, 2014.

M. Spiegelman. *An introduction to dynamical systems and chaos.* 1997.

M. Stix. *The Sun.* Physics and Astronomy, New York, 2000.

K. Sun and J. C. Sprott. Bifurcations of fractional-order diffusionless lorenz system. *Electronic Journal of Theoretical Physics*, 6(22):123–134, 2009.

M. Suzuki. The rotation of sunspots during activity cycle 22. *Solar Physics*, 178: 259–265, 1998.

F. Takens and H. Broer. *Dynamical Systems and Chaos.* Johann Bernoulli institute of Maths. and computer science. Groningen University, The Netherlands, 2009.

J. H. Thomas and N. O. Weiss. Fine structure in sunspots. *Annu. Rev. Astron. Astrophys*, 42:517–548, 2004.

J. E. Vernazza, E. H. Avrett, and R. Loeser. Structure of the solar chromosphere. ii - the underlying photosphere and temperature-minimum region. *Astrophysical Journal Supplement Series*, 224:1–60, 1976.

X. Wang and W. Chen. Bifurcation analysis and control of the rossler system. *IEEE*, 978:1484–1488, 2011.

X. Wang and M. A. Wang. Hyperchaos generated from lorenz system. *Physica A*, 387:3751–3758, 2008.

F. T. Watson. *Investigating sunspot and photospheric magnetic field properties using automated solar feature detection.* University of Glasgow., 2012.

N. O. Weiss. Periodicity and aperiodicity in solar magnetic activity. *Phil. Trans. R. Soc. Lond. A*, 330:617–625, 1990.

N. O. Weiss and M. J. Thompson. The solar dynamo. *Space Sci. Rev.*, 144:53–66, 2009.

N. O. Weiss, F. Cattaneo, and C. A. Jones. Periodic and aperiodic dynamo waves. *Geophys. Astrophp. Fluid Dynamics*, 30:305–341, 1984.

J. C. Willems. Dissipative dynamical systems part i: General theory. *Archive for Rational Mechanics and Analysis*, 45:321–351, 1972.

J. G. Wu, G. Q. Xia, X. Tang, X. D. Lin, L. Deng, T. Fan, and Z. M. Wu. Time delay signature concealment of optical feedback induced chaos in an external cavity semiconductor laser. *Opt. Express,*, 18:66616666, 2010.

D. J. Wuebbles, C. Wei, and K. O. Patten. Effects on stratospheric maunder minimum ozone and temperature during the. *GEOPHYSICAL RESEARCH LETTERS*, 25(4):523–526, 1998.

Z. Yan. Hopf bifurcation in the lorenz-type chaotic system. *Chaos Solutions and Fractals*, 31:1135–1142, 2005.

Q. Yang and C. Zeng. Chaos in fractional conjugate lorenz system and its scaling attractors. *Commun Nonlinear Sci Numer Simulat*, 15:40414051, 2010.

M. T. Yassen. Chaos synchronization between two different chaotic system using active control. *Chaos solution and Fractals*, 23:131–140, 2005.

K. K. C. Yau and F. R. Stephenson. A revised catalogue of far eastern observations of sunspots (165 bc to ad 1918). *Quarterly Journal of the Royal Astronomical Society*, 29:175–197, 1988.

C.H. Ziener, M. Rückl, T. Kampf, W. R. Bauer, and H. P. Schlemmer. Mathieu functions for purely imaginary parameters. *J. Compt. Applied Math.*, 236: 4513–4524, 2012.

Appendix A:

Given that a similar linear relation between C_0 and ω_1 was found in the case where an oscillatory control parameter was additive in Douglas et al. (2013) , we examine the generation of F driven by $D = C_0 \cos \omega_1 t$ to obtain an analytical estimate of the effect of C_0 and ω_1 on F as follows:

$$\frac{dF}{dt} \approx C_0 \cos \omega_1 t. \tag{6.4}$$

The time integration of Eq. (6.4) from $t = 0$ to t gives

$$F(t) \approx \frac{C_0}{\omega_1} \sin \omega_1 t. \tag{6.5}$$

Then, the time average of $[F(t)]^2$ over $t = [0, T]$ in the limit of $T \to \infty$ gives

$$\langle F(t)^2 \rangle \approx \frac{1}{T} \int_0^T dt [F(t)]^2 = \frac{C_0^2}{T\omega_1^2} \int_0^T dt [\sin \omega_1 t]^2 = \frac{C_0^2}{2\omega_1^2}, \tag{6.6}$$

Thus, Eq. (6.6) shows that on average, the root mean square (RMS) value of $F_{RMS} \approx C_0/\omega_1$, implying a linear relation between C_0 and ω_1.